The Design and Prototyping of Interface Technologies for Integrated Renewable Energy Systems

A thesis submitted to the School of Engineering at the University of East Anglia in partial fulfilment of the requirements for the degree of Doctor of Philosophy

Michael O'Brien

April 2023

Acknowledgements

I would like to acknowledge;

The support of my sponsor, mentor and friend Dr Noel McWilliam, for having more faith in me than I have myself.

My Academic supervisor Dr Sonia Melendi-Espina, for always having my corner, teaching me the timely utilisation of puppy-dog eyes and the occasional threats of violence - nunca te olvidaré.

The technical support I received from Dave Blomfield, Nick Griffin, Lil Dave, Gareth Flowerdieu and Peter Hemmins, thank you for the numerous 'loans' of equipment, the time taken walking me to the door and, for some, occasionally unlocking it so I could get back in the lab.

To Ruth and Jonty for helping me start this journey.

And to the most beautiful girl in Norwich, Ava Grace Weston, for keeping me sane, almost...

Dedications

I dedicate this thesis to

Dr Richard 'Al' Shiells

shine on you crazy diamond x

Contents

List of Figures i

List of Tables vii

1 Introduction 1

1.1 The State of Play 1

1.2 Population Growth & Climate Change 3

1.3 Interdependency Linked Commodities: the water energy food nexus 5

1.3.1 Water 5

1.3.2 Energy 6

1.3.3 Food 7

1.4 Positive Feedback Gain: turning the Water-Energy-Food nexus on its head 9

2 Generating Energy & Reducing Emissions 17

2.1 Technological Solutions 18

2.1.1 Carbon Capture, Utilisation & Storage 18

2.1.2 Modular Nuclear Technologies 18
2.1.3 Fusion 19
2.1.4 Demand Side Management & Energy Efficiency 20
2.1.5 Renewable Energy 20
2.1.5.1 Hydro 21
2.1.5.2 Solar 22
2.1.5.3 Wind 22
2.1.6 Considerations of the Electricity Generation Component . . 23
2.2 Energy Storage 24
2.2.1 Electrical-Energy Storage 24
2.2.2 Mechanical Energy Storage 25
2.2.3 Thermal Energy Storage 25
2.2.4 Electro-Chemical Energy Storage 26
2.2.5 Chemical Energy Storage 26
2.2.5.1 Bio-Fuel 27
2.2.5.2 Bio-Mass 27
2.3 Considerations of Energy Storage 27
2.4 Desalination 28
2.4.1 Desalination Technologies 29
2.4.1.1 Multi-Effect Distillation 29
2.4.1.2 Multi-Stage Flash Distillation 29

2.4.1.3 Other Desalination 30

2.5 Integrated Renewable Energy Systems 30

2.6 Integrated Renewable Energy Systems Incorporating Desalination . 32

2.7 Previous Work: The Dowerin Integrated Renewable Energy System 32

2.7.1 Dowerin and The Silent Flood 33

2.7.2 A Photo Journey: from Exeter to Australia 34

2.7.3 A PhD Born from a Field Trial 38

3 Project Aims & Objectives **40**

3.1 Research Goals 42

4 The System: simulating a photovoltaic-reverse osmosis unit in the lab **46**

4.1 The Lab Set-Up: a full breakdown 48

4.2 Reverse Osmosis 49

4.2.1 Membranes 50

4.2.2 Temperature Effect 51

4.2.3 The Clark Pump 51

4.2.4 The Specific Energy of Consumption of Desalination 59

4.2.5 Salinity, Total Dissolved Solids, Parts Per Million & Electrical Conductivity 60

4.3 System Components & Technical Specifications 61

4.3.1 The Rectifier 61

4.3.2 The Solar Pump Controller 61
4.3.3 The Pump 63
4.3.4 Reverse Osmosis Pressure Vessel 65
4.3.5 Reverse Osmosis Membrane 65
4.3.6 Indeterminate Bulk Container 65
4.4 Instrumentation 66
4.4.1 Pressure Gauge 67
4.4.2 Pressure Transducers 68
4.4.3 Flow Meters 68
4.4.4 Pressure Relief Valve 68
4.4.5 Gate Valve 68
4.5 Results & Discussion 69
4.5.1 Flow, Pressure & Power Benchmarking 69
4.5.2 Optimal Operating Window 73
4.5.3 Summary of Results 74

5 Modelling System Dynamics: the reverse osmosis component 75

5.1 Introduction 75
5.2 Equilibrium Modelling of Reverse Osmosis Systems 76
5.3 Dynamic Modelling & the Circuit Analogy 77
5.4 Parametric vs Non-parametric Models 77

5.5 Candidate Models 79

5.5.1 Black-Box Modelling 80

5.5.2 Structured Parametric: resistors in parallel 81

5.5.3 Structured Parametric: the hybrid model 82

5.6 Methodology: initial input signals 82

5.7 Results 86

5.7.1 Resistance Function: non-parametric 86

5.8 Discussion 88

6 The Energy Recovery Prototype REDACTED 91

7 Modelling System Dynamics: the circuit equivalence model 92

7.1 Introduction 92

7.2 Electronic Phenomena & Their Analogous Counterparts 94

7.3 Deriving the Circuit Equivalence Model 95

7.3.1 Insights & Assumptions 96

7.3.2 Uncoupled Discharge Dynamics 98

7.3.3 Coupling & Constraints 100

7.3.4 Energy Losses are Negligible 101

7.3.5 Coupled Charge Dynamics 101

7.3.6 Fluids are Ideal 102

7.3.7 Partial Filling of the Inner Chamber 102

7.4 Model Parameteriastion 105

7.4.1 Rectifier Bridge Resistances 106

7.4.2 General Methdology 108

7.4.3 Results 109

7.5 Spring Configuration 111

7.5.1 Methodology 114

7.6 Pistonless Configuration 118

7.7 Discussion 118

8 Conclusion Summary **122**

8.1 Reverse Osmosis Model Summary 122

8.2 The Energy Recovery Prototype Summary: REDACTED 123

8.3 The Circuit Equivalence Model Summary 123

Bibliography **125**

Appendices **136**

A Appendix A: system modelling techniques **136**

A.1 Bode Plots 136

A.2 Laplace Transform vs the Fast Fourier Transform 137

B Appendix B: code progression **141**

B.1 Arduino 141

B.1.1 5 kHz data logger 141

B.1.2 8 pin checker 168

B.2 MatLab 169

B.2.1 dataCheckScript 170

B.2.1.1 fullDataCheck fullSystem 170

B.2.1.2 runMainTestScript theBigKahuna fullSystem . . . 172

B.2.1.3 loadData fullSystem 182

B.2.1.4 flowTurbines 183

B.2.1.5 scales 189

B.2.1.6 pressureTransducers 190

B.2.1.7 sickTransducers 190

B.2.1.8 psuOutputs 191

B.2.1.9 HEsensors 191

B.2.1.10 getIRFFTs 192

List of Figures

1.2.1 Global population forecast to reach 8.5 billion in the next seven years even amidst a continued decline in the rate of births. 3

1.3.1 Regions of the world suffering from water stress by percentage by 2040 6

1.3.2 Regions of the world without access to electricity 7

1.3.3 Anthropogenic climate change has slowed global agricultural growth, by region in percentage reduction 8

1.3.4 Corn vs ethanol production in the USA 8

1.4.1 A visualisation of the positive feedback cycle. 12

1.4.2 Flow diagram depicting the inputs and outputs of an IRES. 13

2.1.1 Share of low carbon generation globally as of 2020 21

2.7.1 Michael O'Brien receiving training on the BioGen at Exeter University's Cornwall Campus, Tremough. 34

2.7.2 Preparing the system for international shipping. Note three RO pressure vessels, the full Spectra Watermaker kit including the Clark, a low pressure CAT pump, power converter and high-pressure pump controller. 34

2.7.3 Good bye, England. Hello, Australia. 35

2.7.4 The Dowering farmstead with adequate water containment capacity. The Dowerin landscape. 35

2.7.5 The first task was to build suitable shelter for the IRES. 36

2.7.6 Commissioning the IRES in its new home. 36

2.7.7 Salt drainage trench excavation in action. 37

4.1.1 Initial configuration of lab based set up 49

4.2.1 Components of a reverse osmosis spiral wound membrane 50

4.2.2 The Clark pump 52

4.2.3 Clark pump operation 52

4.2.4 Sections of the Clark 53

4.2.5 A visual reference to the 'inner and outer' chambers 54

4.2.6 Flows in to and out of the inner and outer chambers 54

4.2.7 'rectifier bridge', birds eye view of bottom section of Clark 55

4.3.1 Estimated pump performance (in red) of model 4FLS4.2/120-D72/1300 taken from manufacturer's website. NOTE The red line is an extrapolation based on the other models. 64

4.4.1 The lab based set up with instrumentation. 66

4.4.2 The lab set-up for benchmarking the reverse osmosis. 67

4.5.1 Flow versus pressure curves for all voltage setting data sets i.e. 35 V, 50 V, 55 V, 60 V, 65 V, 70 V, 72 V and 75 V. 69

4.5.2 Pump performance comparison between the manufacturer's data sheet, the dashed line, and the two closest empirical data sets, 72 V and 75 V. 71

4.5.3 Power vs pressure curves for the 5 V increment data sets ie 50 V - 75 V. 72

4.5.4 Power versus flow curves for the 5 V increment data sets i.e. 50 V - 75V. 72

4.5.5 Optimal operating power versus pressure window; 300 W - 1300 W and 0.3 MPa - 0.8 MPa between 50 V and 70 V. 73

5.5.1 (a) resistors in parallel model (b) black box model. Qf, Qp, Qr are feed flow, permeate flow and reject flow respectively. Pf and Pr are feed pressure and reject pressure. Rg and R1 are resistances to water flow through the membrane and across the membrane respectively. 79

5.7.1 Black box model fits 87

5.7.2 Non-parametric estimation for resistance R_1 88

5.7.3 Non-parametric estimation for resistance R_g 89

5.7.4 Parametric estimation for resistance R_g 89

7.3.1 The lab based PVRO system with Clark redrawn as an electronic circuit 97

7.4.1 'rectifier bridge'circuit model withsensor placement 107

7.4.2 'rectifier bridge' dynamic regression coefficients 109

7.4.3 'rectifier bridge' power dissipation in Watts 110

7.5.1 'Spring Configuration' Clark assembly 112

7.5.2 'Spring Configuration' circuit model 115

7.5.3 A hacked pair of scales interfaced with an Arduino to measure extremely low leakage flow. 116

List of Tables

4.1 Table identifying and naming the input:output variables and the chosen SI units that are used in this document going forward . . . 47

4.2 Rated values of solar pump controller 62

4.3 Rated values of of the submersible pump 63

5.1 The standard data suite used to evaluate the system under different parameters, comprised of 12 separate data sets 86

1

Introduction

This chapter introduces the problem in its general form. The consequences of a rising population, climate change, diminishing resources and the inequitable distribution of basic commodities are discussed. The end of the chapter highlights the often negative interdependent relationships between water, energy and food and prepare the reader for the mission statement; the potential for inverting these interdependencies and leveraging the dynamics for a positive gain.

1.1 The State of Play

Rising global population, the spread of Westernised dietary habits, the pursuit of year-on-year economic growth, increasing urbanisation and runaway climate change are placing unprecedented stress on water, energy and food systems the like of which has never been witnessed in human history before.

In the past 100 years global population has increased by 4.4 times. Water withdrawal from renewable freshwater resources for agricultural, municipal and industrial needs has increased 1.7 times faster than population growth within the same period, 7.3 times greater than it was in the last century [1].

Population and consumption trends are set to continue well into the century, with world population projected to increase 25% [2], water demand 55% [3] and global energy demand 30-60% [4] all by 2050 [5]. Agricultural production will

need to increase 70% over the same period to meet food, feedstock and fibre requirements of an estimated 9.7 billion people. To reiterate this needs to be accomplished within a time-scale of less than 30 years.

Meeting these consumption trend demands set against a backdrop of diminishing environmental resources, degraded ecosystems, volatile global markets and climate instabilities, whilst ensuring environmental integrity and social equity is a significant and essential challenge. Water shortages are already a leading cause of morbidity and mortality resulting in 9.1% of the global disease burden and 6.3% of all deaths [6]. Over 1 billion people currently lack access to clean water, a figure expected to rise to 3.9 billion by 2050 [7] [8].

Constrained resources, energy insecurity and global inequality cannot be discussed without mentioning the more recent event of the war in Ukraine 2021. The hostilities exacerbated an already unstable global supply chain, the vulnerabilities of which were initially exposed during COVID19, and pushed energy prices up worldwide. Both of these issues impacted the price of food commodities on the global market. Europe was particularly impacted due to a general lack of energy self-sufficiency and an over reliance on fossil fuels.

Is this the new normal? Is this acceptable? Is there an alternative?

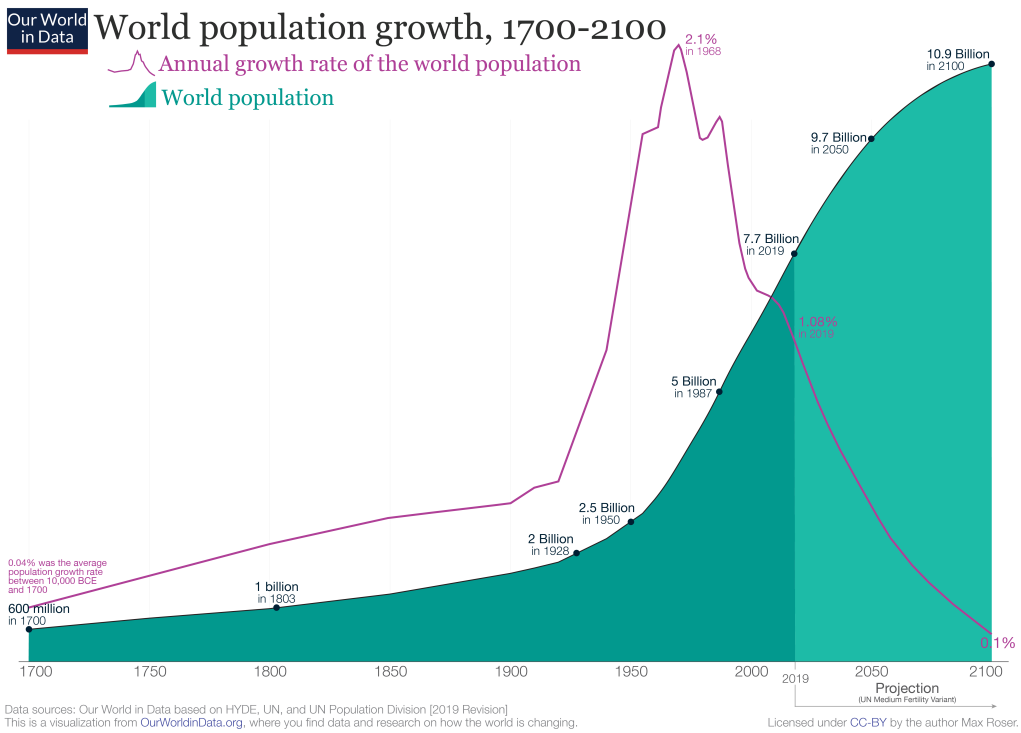

Figure 1.2.1: Global population forecast to reach 8.5 billion in the next seven years even amidst a continued decline in the rate of births.

1.2 Population Growth & Climate Change

The 15th November 2022 is the day the world population reached 8 billion see figure 1.2.1.

Global fertility rates have been in decline since their peak in 1963. This is due to an abrupt drop in total fertility across all regions occurring simultaneously, a phenomenon known as the demographic transition [10]. In spite of this decline there is still an estimated 82 million additional people per year that will have to be provided for [39].

The industrial revolution ushered in a population explosion over the last two centuries and the ubiquitous use of oil have had an inconceivable impact on the natural environment. Anthropogenic forcing of carbon dioxide due to the combustion of fossil fuels, natural habitats being decimated for their resource and plastic pollution permeating global ecosystem have all contribute to devastating this planet and continue to do so.

Esteemed naturalist and environmental advocate, Sir David Attenborough, succinctly articulates the consequences of climate change below:

> *"And if the natural world can no longer support the most basic of our needs, then most of the rest of civilisation will quickly break down. Please make no mistake, climate change is the biggest threat to security that modern humans have ever faced."*
>
> David Attenborough [40]

Carbon dioxide along with other green house gasses (GHGs) are directly linked to global warming. Scientific consensus is that if global temperatures increase beyond 1.5% of 2010s average temperature then the world would have gone past the 'tipping point'. Extreme weather events, erratic meteorological systems, sea level rise, rising sea temperature, wild fires, draught, heat-waves all accelerate eco system failure, mass species extinction events and leave humanity fighting over the dwindling resources of an ever increasingly hostile planet.

Those who are reading this paragraph have lived through the steepest part of the curve in Figure 1.2.1 and it is this generations responsibility to sustainably provide the resources, space and energy to secure the future for the next generation's. Methodologies, processes and technologies of equitably supporting a large world population need to be initiated now, while simultaneously reducing carbon emissions. This by far is the single biggest issue humankind needs to address urgently.

1.3 Interdependency Linked Commodities: the water energy food nexus

In a resource limited world, interdependency between primary production systems become a significant concern as the production of one often necessitates consumption of another.

Competing interests between these inextricably linked critical domains summarises the "Water-Energy-Food, WEF, Nexus" and poses fundamental questions regarding sustainable and equitable production and distribution of our most basic commodities.

In 2015 the United Nations laid out its ambitious Sustainability Development Goals, UNSDG. Covering 17 of the worlds most pressing issues, and a target of 2030 to achieve them by. Water, food and energy were on the list.

By the end of 2050 the UN also committed it's members to a 'net zero' carbon target by 2050. This means a reduction in emissions of 45% compared to 2010 levels. None of these targets are currently being met [76].

This section will show how the already stressed commodities; food, energy and water, are competitively intertwined, and how the ramifications of the relationships between these three basic but essential commodities culminates with one often having to be sacrificed for another.

1.3.1 Water

Goal 6 of the UNSDG is to "ensure availability and sustainable management of **water** and sanitation for all."

Figure 1.3.1 shows countries effected by water stress, as a ratio of water withdrawal to renewable surface and groundwater supplies, by 2040 [45].

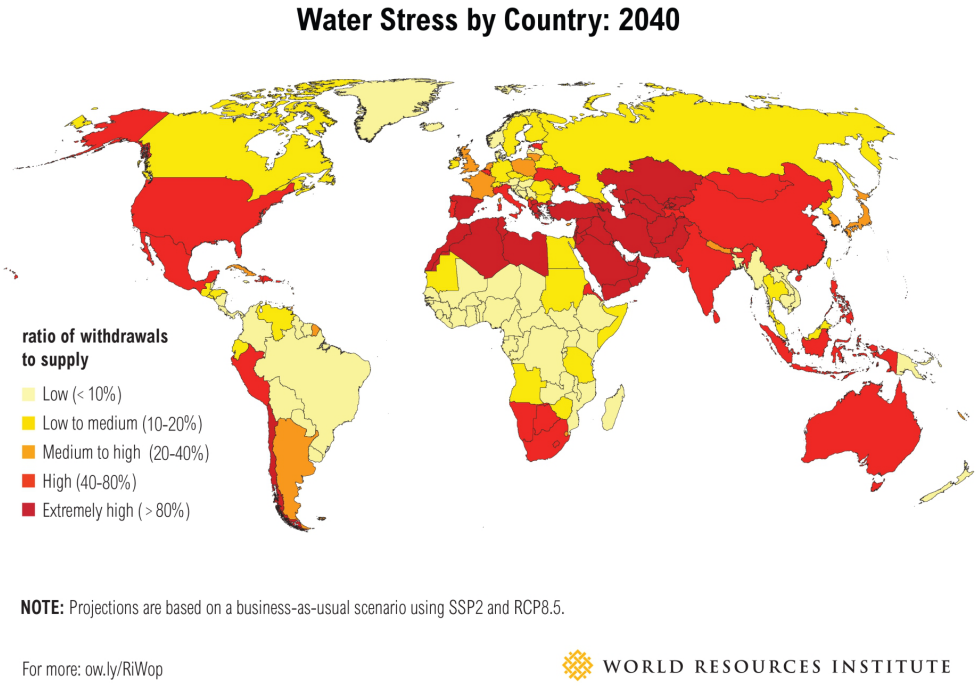

Figure 1.3.1: Regions of the world suffering from water stress by percentage by 2040

Globally, agriculture accounts for 70% of water withdrawal [1] and 15% is attributed to energy production [8]. In Europe and the USA the water used in power plant cooling accounts for 43% and 50% of total freshwater withdrawal respectively. 90% of worldwide power generation is deemed to be water intensive [8].

How will energy generation be able to match the increased demand over the next 25 years, without impacting water stress, while maintaining carbon emission reduction commitments?

1.3.2 Energy

Goal 7 of the UNSDG is to "ensure access to affordable, sustainable and modern **energy** for all."

Energy production is one of the main drivers of climate change, contributing to

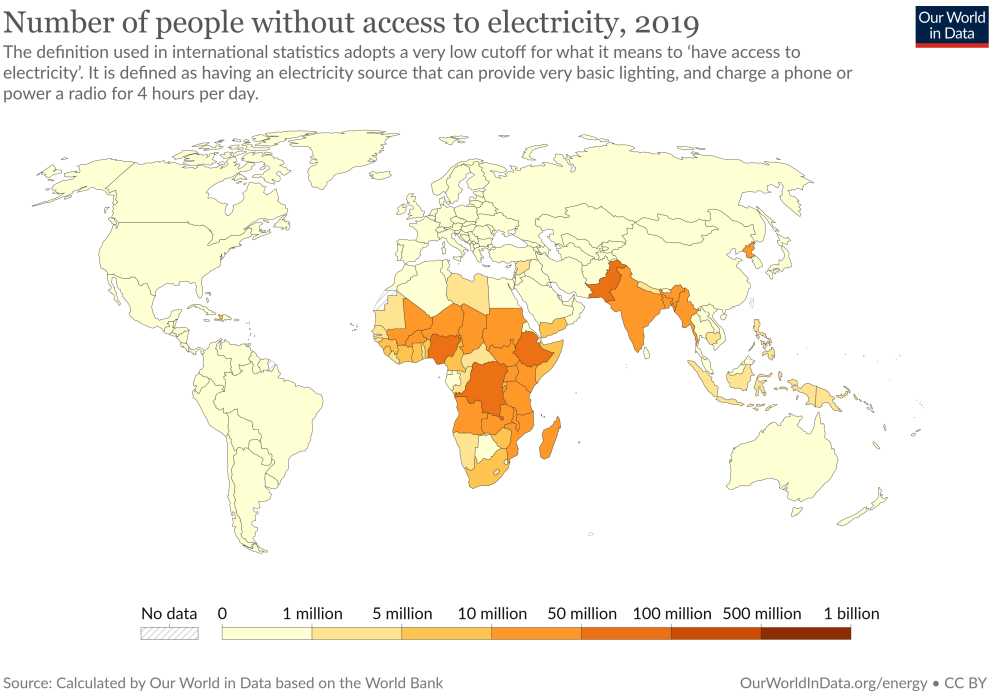

Figure 1.3.2: Regions of the world without access to electricity

80% of green house gasses. Nearly 10% of the world's population do not have access to electricity and 32.5% cook their food with harmful fuels [41]. The food industry is responsible for 30% of total energy consumption [2].

There are 940 million people without access to electricity see figure 1.3.2. 3 billion people suffer from high health costs from indoor pollution due to not having access to clean cooking fuels.

High energy prices directly effect the cost of food production. As has already been witnessed by recent geo-political hostilities [48]. In a bid for energy security due to the recent geo-political turmoil delivering renewable energy generative capacity has been accelerated, moving the UN closer to the Paris agreement target [50].

1.3.3 Food

Goal 2 of the UNSDG is to "End hunger, achieve **food** security and improved nutrition and promote sustainable agriculture."

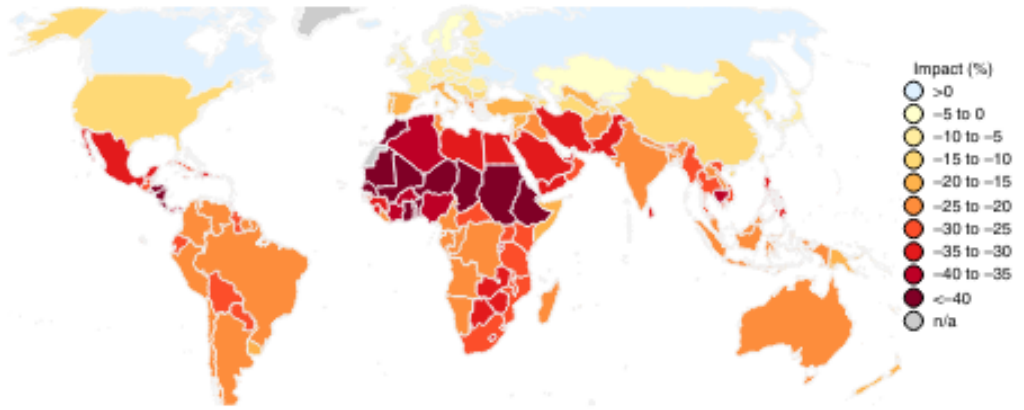

Figure 1.3.3: Anthropogenic climate change has slowed global agricultural growth, by region in percentage reduction

Climate change has adversely affected agriculture by slowing agriculture growth by greater than 40%, see Figure 1.3.3. 828 million people suffered from hunger in 2021. After falling for decades global hunger rose from 2019-2021 affecting nearly 10% of the global population. 45% of child deaths are due to hunger and related causes [49].

With a growing population and the promise of lowered carbon emissions biofuels already play a major part in global decarbonisation ambitions. In 2022 the UK suggested to renege on climate commitments of biocrop production in favour of food crops due to the international food shortage compounded by the war in Ukraine [44]. This was a contentious issue for the USA, a major producer of bioethanol from corn. Figure 1.3.4 perfectly illustrates the competition between food versus fuel crops.

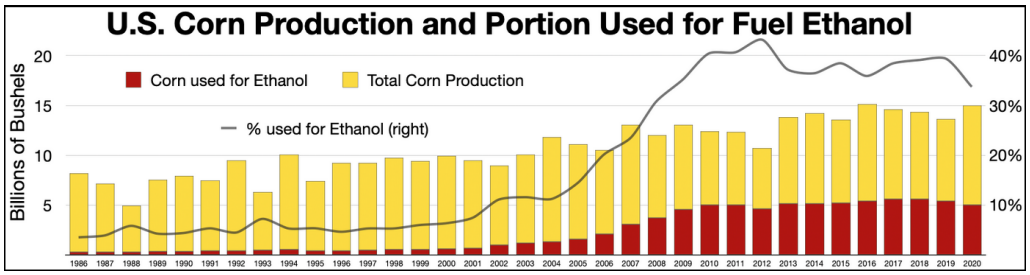

Figure 1.3.4: Corn vs ethanol production in the USA

1.4 Positive Feedback Gain: turning the Water-Energy-Food nexus on its head

A possible contribution to the solution of the sustainability issues posed by the WEF nexus could be a system that provides reliable, accessible and affordable energy and water at a low environmental impact to those people who are suffering from energy, water and food shortages. Sustainability issues require a sustainable solution and as such would utilise renewable energy. The solution would have to overcome the drawbacks inherent with renewable energy generation i.e. intermittency, storage, decentralised generation and inaccessible locations. Such a solution would further benefit from being a self-sustaining, adaptable, modular system. In addition delivering multiple utilities, for various applications, while accommodating different scales of demand and adjusting operational dynamics to fit variable environmental influences. While also supporting energy storage capabilities. Such a system will furthermore be referred to as an integrated renewable energy system, IRES.

Consider a process within a system that uses excess energy from solar power generation to desalinate water. Specific energy is defined as the amount of the energy in kWh required to desalinate one cubic meter of saline water. The theoretical minimum energy required for desalination, E_D, is given by van't Hoff's formula [84], yielding a specific energy of approximately 0.77 kWh/m^3. Current industry standard technologies yield a specific energy of seawater, SE_{SW}, in the ranges of 2.6-8.5 kWh/m^3 [83].

Suppose now that the desalinated water is used as irrigation for the production of a crop, C. The yield of the crop, Y_C, kg/m^3 will depend on multiple factors, including choice of crop and variety, farm management practices (e.g. sowing-density, weed control, use and type of fertiliser), soil-types, evapotranspiration (which is itself a function of the prior factors; irradiance, temperature, wind speed and humidity) as well as rainfall and irrigation amounts and patterns. Denote

the depth of water to which the crop is irrigated in meters as I.

Therefore, a cubic meter of water would irrigate an area

$$A = \frac{1}{I} \tag{1.4.1}$$

giving rise to crop per m^2 of irrigation water,

$$C = A(I)Y_C(I) = \frac{Y_C(I)}{1} kg/m^3 \tag{1.4.2}$$

which may be thought of as a "specific yield" in analogy to specific energy.

The energy content, E_C, of the crop is simply

$$E_C = C\rho_C \tag{1.4.3}$$

where ρ_C is the energy density of the crop in kWh/kg.

The crop itself can, in whole or part, be converted to biofuel, B.

$$E_B = \eta_C E_C \tag{1.4.4}$$

Where η_C embeds the crop fraction used with losses within the harvesting and processing method.

Biofuel can be stored and used to generate power, E_P, as needed.

$$E_P = \eta_B E_B \tag{1.4.5}$$

Where η_B represents losses of the conversion process.

The inputs and outputs of each step of the process embed energy content, corresponding to a stepwise energy transformation and an overall energy yield.

ζ is defined as the total conversion energy ratio of the system, which is itself the product of individual conversion energy ratios that represent each processing

stage of the system. Thus all zetas represent the energy input versus output of conversion processes.

$$\zeta = \frac{EnergyOutput}{EnergyInput} = \zeta_D \zeta_C \zeta_B \zeta_P \tag{1.4.6}$$

Where ζ_D, ζ_C, ζ_B and ζ_P are the ratios of energy input/outputs for each conversion sub-process within the system; corresponding to desalination, crop, biofuel and power generation respectively.

Here

$$\zeta_D = \frac{E_D}{SE_{SW}} \tag{1.4.7}$$

ζ_D represents the ratio of energy intrinsically embedded within the purified water relative to seawater against that used to generate the water. Thus ζ_D is also the energetic efficiency of the desalination process, E_D, relative to the theoretical minimum for seawater, SE_{SW}.

$$\zeta_C = \frac{E_C}{E_D} \tag{1.4.8}$$

ζ_C is the ratio of energy embedded within the crop, E_C, to that embedded within the water used to produce the crop, E_C.

Both

$$\zeta_B = \frac{E_B}{E_C} = \eta_C \tag{1.4.9}$$

and

$$\zeta_P = \frac{E_P}{E_B} = \eta_B \tag{1.4.10}$$

are similar process efficiencies pertaining to the conversion of the crop to biofuel and the biofuel to power respectively.

The above equations have shown that

$$\zeta_D \zeta_C \zeta_B \zeta_P = \frac{E_D}{SE_{SW}} \frac{E_C}{E_D} \frac{E_B}{E_C} \frac{E_P}{E_B} \tag{1.4.11}$$

Combining 1.4.6 with 1.4.11 gives rise to

$$\zeta = \frac{EnergyOutput}{EnergyInput} = \zeta_D \zeta_C \zeta_B \zeta_P = \frac{E_D}{SE_{SW}} \frac{E_C}{E_D} \frac{E_B}{E_C} \frac{E_P}{E_B} \tag{1.4.12}$$

which ultimately reduces to

$$\zeta = \frac{E_P}{SE_{SW}} \tag{1.4.13}$$

As long as more energy is produced by the biofuel component, in the form of electricity generation, than the energy required to irrigate the crop for the biofuel in the first place, then a positive feedback gain is achieved. See Figure 1.4.1 for a visual representation of the feedback gain described in 1.4.

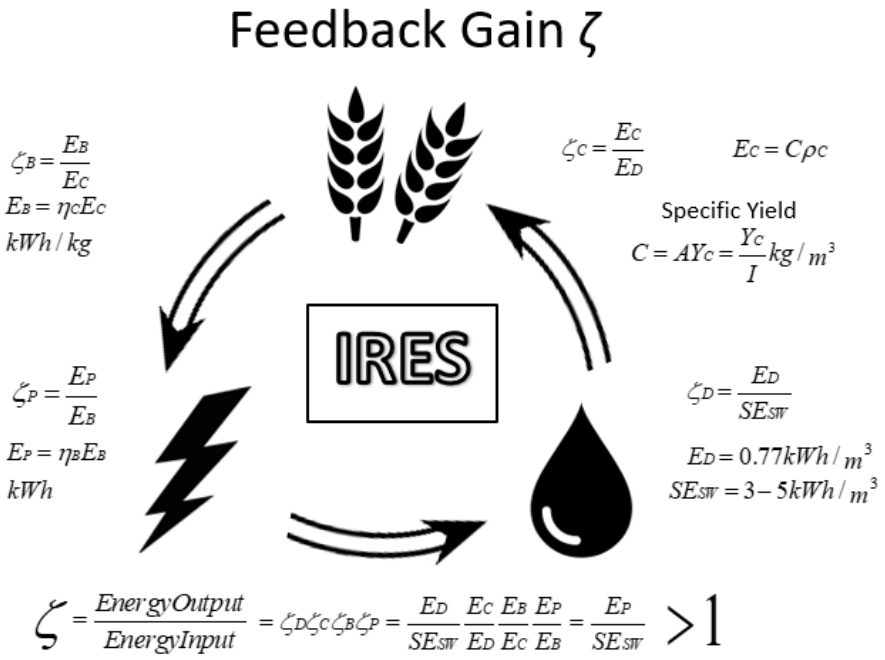

Figure 1.4.1: A visualisation of the positive feedback cycle.

As a minimum, requirement component technologies should be sought such that ζ is higher than efficiencies of alternate storage technologies. Both water and biofuel are more convenient forms of storage than high temperature thermal, hydrogen or batteries. The above system presents an additional possibility for

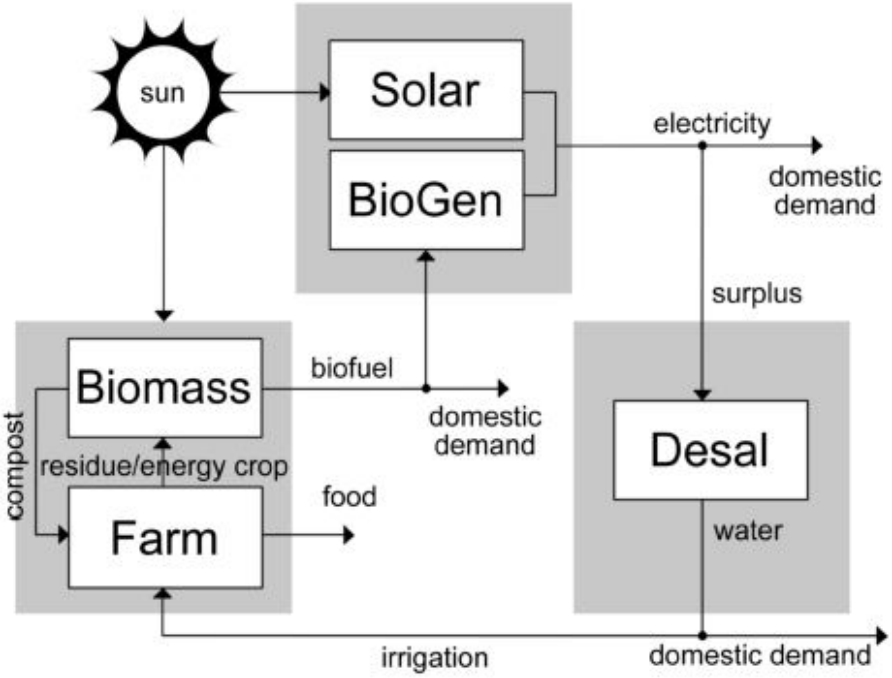

Figure 1.4.2: Flow diagram depicting the inputs and outputs of an IRES.

positive feedback wherein power produced by the process may be used to further increase water production, creating a closed-loop cycling of energy and materials.

It is crucial to note that ζ_C may take values greater than unity, since the crop attenuates solar energy extraneous to the system, thereby increasing the entropy of the system. Should this gain exceed the losses then the system may ramp-up to full capacity production, auto-generating system inputs and producing surplus output.

Such a system incorporating photovoltaic and biofuel based energy generation with water desalination delivers the resources required to alleviate the issues associated with the WEF nexus. The dual renewable energy generation of PV and biofuel provides a sustainable electric load, capable of a 24/7-demand profile, eliminating intermittency. The desalination aspect supplies both potable water for human consumption and irrigation as well as energy storage; in the form of stored potable water, but also in the form of the stored chemical energy of the irrigated bio-crops; this aspect overcomes storage issues and alleviates the strain associated with water withdrawal, see Figure 1.4.2 for a visualisation of an IRES

as described.

Note that Figure 1.4.2 depicts the electricity production after one full cycle. The electricity contributed via the bio-gen originates from the solar input not only invested in the desalination and biofuel processing phases via the input of photovoltaic panels (PV), but also from the solar energy attenuation within the crop growth. As such, the electricity output depicted in Figure 1.4.2 is the sum of the the solar component from the PV and the bio-gen component, which in turn is a product of efficiencies representing each phase of conversion i.e. desalination, crop growth, bio-fuel processing and power generation.

Utilising all or part of the water produced, for the irrigation of bio-crops, embeds a positive feedback cycle within the system, ensuring an energy secure future. The integrated process of the system creates a closed-loop cycling of products resulting in an overall positive gain per cycle.

Although, RO plants that treat brackish water have lesser capacity than their sea-water counterparts they account for nearly half of RO plants worldwide [95]. The proposed system is ideally suited on land that could be used for agricultural crops, yet is otherwise constrained due to lack of freshwater and sub-par soil substrates. Such areas are commonly found in dry, arid regions of the world. Regions that have naturally saline aquifers or groundwater that has become saline due to ingress of seawater or anthropogenic causes [96], suffer with unacceptable levels of salinity unable to support crop propagation; the wheat belt of Western Australia for example. In such areas the system would not be desalinating highly saline sea-water but mid-saline brackish water instead. The repercussive effects of an active system will have beneficial impact on soil quality replenishment, and localised ground-water take-up.

There is commercial interest to develop a set of technologies that satisfy,

$$\eta_P \eta_D \eta_I \eta_C > 1 \tag{1.4.14}$$

where η_P, η_D, η_I and η_C represent the efficiencies of the power, desalination, irrigation and crop processes respectively.

If satisfied the system can achieve a positive feedback gain and cyclically ramp-up to maximum capacity production, 24/7, without fossil fuels or batteries. Thereby solving intermittency and storage issue furthermore being 100% sustainable and renewable. This is achieved by supplementing power generation with the bio-fuel component when solar irradiance is sub-optimal or during night time production schedules.

This is made possible since relieving environmental constraints to crop production; water stress, aquifer salinity, soil conditioning and organic content, the system is able to attenuate an additional source of solar energy input via biofuel production. The improvement of the soil and water quality of the local environment will, in and of itself, lead to an increase in crop yield.

Efficiencies of each of the components embed a feedback gain to the system, if feedback is greater than 1 then the system has actualised and autonomous production is achieved. Such a system will provide a multitude of research opportunities.

Specific interesting aspects of the system include; a novel feedback gain, closed loop cycling, waste streams as energy streams, 100% renewable, fundamental commodity provision, servicing of off grid communities, low waste, beneficial environmental impact, natural hedging removing intermittency, built in redundancy and tackling the water, energy and food nexus.

The present challenge is maximising the feedback gain ratio to intensify system efficacy. As previously expressed in 1.4.14; for autonomous production feedback gain has to be greater than 1. The industry sponsor, Mitravitae, requires a feedback gain greater than 2 or 3 to ensure economic viability.

This work will explore the potential to leverage WEF nexus interdependences to create novel synergies for efficient simultaneous production of food, water, energy

and biofuels from systems integrating solar, desalination and biofuel technologies. In particular this PhD focuses on modelling, design and prototyping of novel integration technologies between solar and desalination systems.

It is anticipated that the results borne from the intended research will develop methodologies and deliver technologies that will substantially increase efficiency, and reduce operation and maintenance, O&M, costs of solar-desalination and integrated renewable energy systems (IRES).

2

Generating Energy & Reducing Emissions

Generating energy and reducing emissions do not have to be mutually exclusive. As previously discussed an IRES would comprise of appropriate technologies that can deliver energy generation and desalination with storage capacity to mitigate intermittency. The system has to be modular and portable, able to be deployed in hard to reach/off-grid locations. The technologies involved would be robust and readily available, tried and tested, 'off-the-shelf' components. The order of complexity associated with system should be kept low as possible to facilitate user interaction and satisfaction. As the intended market audience are owners of small holdings, communities and people that do not have access to affordable energy or clean water, the technologies, components and auxiliary processes of the system should be low cost. Affordability should not be a barrier to energy autonomy and freedom from the myriad of health risks and development problems associated water scarcity.

The correct combination of technologies would satisfy this criteria while simultaneously relieving pressure on water constrained area and avoid contributing to emissions.

This chapter will broadly discuss carbon reduction, low-carbon energy generation and sources of renewable energy. Whereafter a current state of the art regarding renewable energy, storage and desalination technologies and techniques will be

presented. This will frame the proposed system in Section 1.4 within the context of the efficacy of available technologies.

2.1 Technological Solutions

2.1.1 Carbon Capture, Utilisation & Storage

Carbon capture, utilisation, and storage (CCUS) is a term to describe any process used to reduce carbon emissions by capturing the carbon dioxide (CO_2), either pre or post- combustion, at point of use or remotely, and storing the CO_2 underground. The utilisation of captured CO_2 is a suitable feedstock for industrial process or enhanced oil recovery [54].

A 2021 study assessing the water footprint of CCUS technologies stated that 'the widespread deployment of CCUS to meet the 1.5 °C climate target would almost double anthropogenic water footprint.' Concluding that 'the most water-efficient way to stabilise the Earth's climate is to rapidly carbonise our energy systems and improve energy efficiency.' [42]

One proposed CCUS project for a power plant uses a third of the electricity generated by the plant to sustain the process while simultaneously increase the plant's water usage by 55% [43]. This isn't an outlier, studies indicate that the energy required to remove the CO_2 post-combustion from coal power plant would consume 30-50% of the plant output and can increase water withdrawal demand by 200% [53].

2.1.2 Modular Nuclear Technologies

Over the past decade the nuclear industry has been developing novel technologies that fall into two categories; small modular reactors and advanced modular reactors, SMRs and AMRs respectively. These novel advanced

reactors, NARs, differ from the traditionally large commercial nuclear power plants LCNPP, by having a reduced power output due to their size. NARs are also fabricated off site, and then transported to, and constructed on, site, hence the modular term in their name. SMR's technological lineage can be directly linked to the LCNPP design. Whereas AMRs have fundamental design differences, incorporating advanced materials and control systems. NARs can be sited at decentralised locations for on site utilisation, making them ideal for energy intensive industrial processes and off-grid communities. The time-scale to grid deployment for AMRs is approximately twenty years, with accelerated deployments of SMRs expected in the next decade [55].

Nuclear technologies are being positioned as having a role in providing energy for a net-zero carbon emissions future. Yet nuclear is at the stage of being deployed in systems intended to be operated and maintained by the general public.

2.1.3 Fusion

Fusion, the holy grail of energy generation, is still, as always, several decades away from commercialisation. A claim had been made recently that a USA project had achieved reached the elusive milestone of net gain, more energy out than in. The fusion reaction lasted a fraction of a second, producing 3.15 MJ of energy from an input of 2.05 MJ [77].

The report failed to include the 300 MJ energy cost of the lasers used to initiate the process in the net gain calculation. When this omitted value is factored into the calculation the input energy is 100 times more than the output energy, which equivalent to a 99% loss - the literal opposite of a net energy gain [51].

"In some senses everything changes; in another, nothing changes," said Justin Wark, a professor of physics and the director of the Oxford Centre for High Energy Density Science. "It is highly unlikely that fusion will impact on a time-scale sufficiently short [enough] to impact our current climate change crisis, so

there must be no let up on our efforts in that regard [52].

2.1.4 Demand Side Management & Energy Efficiency

Reduction in energy usage guarantees reductions in carbon emission. This can be achieved by increasing energy efficiency, doing more with less, or reducing losses due to the transmission, conversion and storage of energy by better matching demand with generation, known as demand side management.

While at Exeter University, Dr Peter Connor introduced the concept of the most valuable unit of energy; the negawatt. A portmanteau of the words negative and watt. Used to describe the energy conserved while achieving the same work output due to increased efficiency, changing of user habits or adopting alternative processes/new technologies. Energy efficiency measures and smarter management techniques will be essential for delivering a cleaner future, and will be a key consideration influencing design choices in the proposed project going forward.

2.1.5 Renewable Energy

The potential energy that renewables could supply on a global scale presents a vast untapped resource. Harnessing a fraction of this under-utilised potential could be used to fuel food, water and energy production systems.

Until recently lack of policy support and limitations at the fundamental level have prevented renewables competing openly with fossil fuel driven energy demands and expectations [12]. Sustainable production is inherently reliant on renewable processes and technology, which come with their own reliability issues. Renewables are notoriously intermittent and inconveniently decentralised, providing further challenges regarding storage and transmission [13].

In 2021 renewable energy accounted for 25% of global electricity generation and

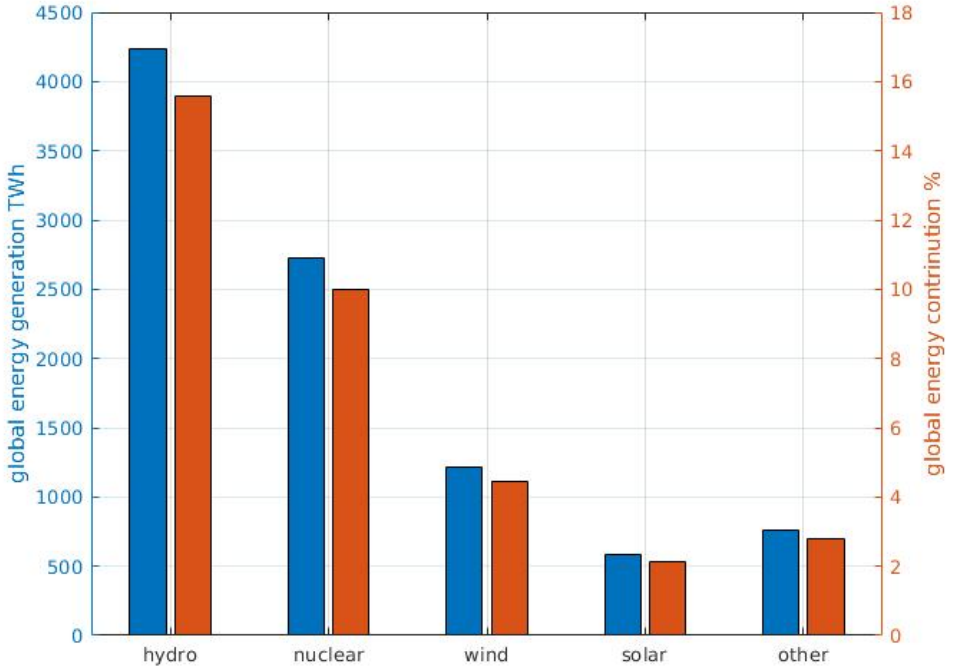

Figure 2.1.1: Share of low carbon generation globally as of 2020

40% for the UK [85]. Hydro and nuclear contribute 15% and 10% of global electricity production respectively, see Figure 2.1.1. Large-infrastructure energy generation schemes have been favoured by the status quo as they fit the traditional model of predictable centralised generation.

Contribution from the remaining renewables (wind, solar, bio-energy and geothermal) combined amount to less than 10% to global electricity generation.

2.1.5.1 Hydro

Hydro accounts for 4,300 TWh of electricity globally, the equivalent of one and a half times the electricity consumption of Europe. Hydro is the third largest source of electricity generation worldwide after coal and natural gas [86]. Yet, in the UK hydro accounts for just 1.2% of total electricity production, an approximate 5 TWh a year [87].

There are over 1,500 hydroplants in the UK. The majority are small to micro

plants with approximately 100 being over one megawatt installed capacity [88].

Hydro turbines have a high efficiency 70-90 %, a high capacity factor of up to 50% [89]. Micro-hydro plant have a high level of predictability, varying with annual rainfall patterns.

Hydro expansion is limited in the UK due to environmental concerns and as most favourable sites have already been developed. There is considerable untapped capacity with a single micro-hydro plant being able to provide reliable generation for several houses. Although, Environment Agency regulations, costly licensing agreements and the Microgeneration Certification Scheme MCS) still being 'under development' since 2013 are all barriers to implementation and further investment [90].

2.1.5.2 Solar

Solar alone is a vast resource: over 1.08×10^{14} kW fall on the Earth's surface every second [3], over the period of a year this is more than 27 times the energy contained in all known and estimated fossil fuel resources [9], if 0.1% of this energy was converted at 10% efficiency rate it would be greater than the total global generating capacity (3000 GW) by a factor of 4 [3].

The Sahara desert could supply the equivalent electricity demand of the world by having 1.2% of its land area taken up with photovoltaic panels, even at moderate conversion rates [11]. Yet, in 2021 solar accounted for just over 4% of electricity generation in the UK.

2.1.5.3 Wind

There is no simple non-arbitrary way to compute the global wind resource, depending on the model methodology for land it could be between 1 - 4 W/m^2 [56].

Ignoring the coefficients of performance and mechanical efficiencies wind power is determined by swept area, air density and wind speed. Wind speed is the dominant variable as it is the third power of velocity, thus wind speed has the biggest impact on generating capacity [57]. Wind speed increases with height due to wind shear, hence bigger is better in the wind industry. Viable wind locations are heavily site constrained [58].

The UK produced 69.83 TWh [91] of electricity in 2021, accounting for 22.6% of total electricity generation [92].

2.1.6 Considerations of the Electricity Generation Component

Although considered clean low-carbon energy sources, fusion and SMRs/AMRs are fundamentally incompatible for the system due to the level of complexity, associated risk and technical barriers to commercial availability.

Small scale hydro, although mostly an untapped resource globally, is not considered for the generation aspect of the system due to the hydrological constraints of the sites the system is designed for. Any location having access to running water is rendered non-applicable by virtue of the systems fundamental design goals. That being said the system could be adapted to concurrently generate electricity and clean liquid waste streams from industrial application that are isolated from utilities, e.g. mining operations.

The depth at which usable geothermal energy is found varies globally and thus 'Deep geothermal energy' is poorly defined. The Uk government has refers to the term as any heat resources from 500 m or more below ground surface. The heat resource required for a geothermal power plant 140 degrees approx is found at depths of 5000 m in the UK. Geothermal energy being extremely location specific thus rendering it non-mobile or modular is a poor fit for the system.

High solar irradiance goes hand in hand with areas that are affected by water stress. It is a natural step to use the source of energy that is most abundant in

areas suffering from water scarcity to alleviate issues associated with water scarcity. Therefore PV is ideally suited as the renewable energy generation component in the first instance, i.e. bootstrapping the system with off grid generation capabilities from the first day of deployment.

PV is a readily available, affordable, proven technology. PV panels by definition are modular and portable. Modern PV technology is robust, has good longevity and has low O&M requirements. Once installed PV will reliably generate over a range of solar irradiance inputs.

Photovoltaic energy is perfectly placed as the system's primary generation component and is now framed within the context of the current state of the art.

2.2 Energy Storage

There are various energy storage techniques and technologies at different stages of availability. Energy storage systems can be classified as electrical, electrochemical, chemical, mechanical and thermal [14]. For the purpose of this exercise the most salient ones will be briefly discussed.

2.2.1 Electrical-Energy Storage

Supercapacitors and superconducting magnetic energy storage, SMES, are examples of electrical energy storage systems. Both systems are at the research, development and demonstration stages of commercial availability i.e. pre-commercial; both have a low energy density and suffer from issues with dissipative losses of energy; up to 40% and 15% a day approximately [15].

2.2.2 Mechanical Energy Storage

Compressed air-energy storage, CAES, flywheel and pumped hydro-energy storage, PHES, are mechanical energy storage systems. CAES can be 80% efficient and has a fast reaction time [12] but has a round-trip efficiency of 48% [16]. Due to the large-scale operation of a pressurised cavern CAES is costly and has a lengthy commissioning process. Attainment of site-specific locations is also prohibitive [12].

Although flywheels are up to 90% efficient, idling losses, low energy density and high capital cost [12] are issues associated with this type of energy storage.

PHES systems are the most prevalent form of energy storage in the world, accounting for 99% of stored electricity capacity. Storage cycle efficiency can be 75% [16]. Generally seen as large storage, in the 10 MW – 1 GW range. Access to large water resource and land area is necessary and expensive infrastructure is required. PHES systems are seen as capitally intensive and environmentally intrusive [12].

2.2.3 Thermal Energy Storage

Hot water, molten salt and phase change material, PCM, are examples of thermal energy storage systems. The application of sensible heat from hot water energy low quality due to its low energy density. PCM has the additional disadvantage of suffering from variable discharging temperature [17]. The high thermal stability, high heat capacity, high density, and low vapour pressure are advantages of molten salt energy storage. Limitations may arise due to storage media costs, the risk of corrosion and the difficulty in hygroscopic salt handling [18].

2.2.4 Electro-Chemical Energy Storage

The efficacy of batteries as an electro-chemical energy storage system has been proven historically. The high energy density, modular portability and reliable storage capacity renders batteries extremely versatile and thus batteries are widely deployed worldwide. They fit readily to many applications - small-scale, off-grid or large commercial [19]. Batteries are sensitive to environmental extremes and are particularly unreliable in hot climates. Irregular and improper charging profiles can have a dramatic impact on life span, reducing storage capability and can be costly to replace. In general batteries have a storage cycle efficiency of 70-85% [18].

That being said an appropriately stored lead-acid battery with a good charge routine can be up to 60% – 95% efficient, have good cycle life and offer rapid electrochemical reaction kinetics. The use of heavy metals is a particular drawback rendering batteries toxic and an environmental hazard [12].

Nickel based batteries can be 60% - 90% efficient, have a low capital cost but are highly toxic [12]. Zinc and vanadium batteries are in the early stage of commercial availability; they are 75% - 85% efficient but have low energy densities [12].

Lithium based batteries are high cost, can be 90% - 100% efficient and have a high power energy density. The high cost of lithium oxide and salt recycling [12] is considered environmentally unfriendly.

2.2.5 Chemical Energy Storage

The conversion of power to gas of methane and hydrogen through electrolysis are forms of chemical energy storage techniques. Although methane is three to four times more energy dense than hydrogen the conversion is more complex and therefore costly. Methane has a round-trip efficiency is 25% - 35% approximately [19].

Hydrogen as an energy storage technique is expensive with low volumetric density 12.7 MJ/m3 and a low boiling point around 273 C at 1 atm pressure makes the liquefaction very energy intensive [12] Hydrogen has a daily self-discharge rate of 4% [15]. Hydrogen is 45% efficient [15] but has very poor round trip efficiency when generated via the electrolysis of water; 20% [16]. The high energy density of hydrogen is countered by the safety implications and cost. [15].

Other forms of chemical energy storage are biofuel and biomass.

2.2.5.1 Bio-Fuel

Biofuel in the form of gas has high energy density and is up to 50% efficient, has a long operational lifetime and a negligible self-discharge [14]. Although the pressurisation required for handling comes with a high cost in energy, current infrastructure can be leveraged to accommodate transport and storage where such access to as grid exists [15].

2.2.5.2 Bio-Mass

Although having a low energy density biomass benefits from having a high storage lifetime, a relative low cost, is easily produced and is ubiquitous. What is more biomass begets biofuel, as an energy storage option the raw product can be stored for a lengthy period of time and used in its crude form or converted to a more energy dense product when needed.

2.3 Considerations of Energy Storage

To tackle the intermittency issues already discussed, a complimentary form of energy storage should be considered when designing a system that generates electricity from renewable sources. This is evermore apparent in off-grid applications, where connection to a transmission network or grid is prohibitive,

some form of storage is essential and must be incorporated.

The different types of storage available are specific to the application, with separate advantages and disadvantages being associated with each. Hydrogen, batteries, flywheel, super-capacitors, biofuel and biomass are all types of energy storage that are appropriate for small-scale generation i.e. less than 100 kW.

Flywheel and super-capacitors are at the pre-commercial stage of development and as such are currently unavailable on the general market. Batteries are an environmental hazard and underperform in hot climates. Hydrogen is costly and is associated with a handling risk. Biofuel can be energy intensive to process and store.

Although biomass has a low energy density it is due too this low-volatility it can be easily stored for extended periods of time until needed. Bio-mass is a ubiquitous global resource and can be made from agricultural waste residue, e.g. the stalk of corn or wheat from commercial crops.

2.4 Desalination

In 2015 more than 3 million people and 150 countries were dependent on water produced by desalination [20]. Desalination is an energy intensive process [32] without the needs being met by renewable energy the estimated fossil fuel cost to produce 1,000 m^3 of potable water a day is 10,000 tonnes of fossil fuel a year [33]. Ensuring the power supply incorporates renewable energy can easily mitigate the negative effects of this intensive energy requirement. Therefore it is essential that the growing demand for water be met by renewable energy [32].

Latest figures show approximately 70% of renewable desalination plants are solar powered, with over 130 renewable desalination plants brought into commission in recent years [34]. Although the cost of producing water from renewable desalination is higher than traditional fossil fuelled techniques the

difference in cost is predicted to fall to 0 in the next 20 years, as the cost of energy produced from renewable sources converges with the cost of energy produced traditionally [20].

This period to parity can be expedited if, as is the case in many countries, subsidies for unsustainable fossil fuels are removed [32]. Increasing efficiencies in water productivity alongside continued research and development in desalination processes will guarantee renewable desalination will out-compete fossil fuelled desalination in the near future [20].

2.4.1 Desalination Technologies

Reverse osmosis, RO, accounts for 85% of current desalination production worldwide. Saline water is forced across a semi-permeable membrane. The water that permeates the membrane is fresh, leaving behind a saline concentrate on the other side [20].

2.4.1.1 Multi-Effect Distillation

In a multi-effect desalination, MED, system, the feedwater is passed through a series of evaporator chambers, heating the feed water in to steam, to condensing into product water. Each stage essentially reuses the energy from the previous stage, with successively lower temperatures and pressures.

MED accounted for approximately 17% of global desalination capacity in 2020, making it the second most common desalination technology after reverse osmosis. [20]

2.4.1.2 Multi-Stage Flash Distillation

Another type of thermal desalination, multi-stage flash desalination, MSFD, accounts for 7% of global desalination. The feed water is flashed over a series of

concurrent heat exchangers. the stages have different pressures corresponding to the boiling points of water at the stage temperatures. [20]

2.4.1.3 Other Desalination

There are other desalination techniques that will emerge as viable technologies in the coming years desalination is forecast to keep on growing by 7% as it has done foe the last 10 years, yet currently they account for 1% of global desalination. [20]

- direct contact spray evaporation
- electrodialysis
- freeze distillation
- solar stills

2.5 Integrated Renewable Energy Systems

There has been an increased interest in IRES in literature in the prior decade; including hydrogen renewable energy systems, HRES, bio-hydrogen integrated renewable energy system, BHIRES, multi-generation IRES, multi-supply IRES and IRES with desalination [20] - [29].

A case study for a proposed BHIRES with the additional functionality of processing biomass waste and converting waste water into a water commodity. The economic appraisal stated that an IRES producing hydrogen via biomass is more economical than an IRES producing hydrogen via electrolysis. The study found a major limitation to bio-hydrogen production was the potential cost of biomass.

The solution is to use low cost feedstock, inexpensive biomass and biowaste. The paper did acknowledge that the value of the system for producing hydrogen alone

was low and that the multiple functions of generating hydrogen and electricity, as well as processing biowaste and waste water should not be overlooked when considering such systems [21].

This is confirmed by numerous studies into IRES providing multiple beneficial processes. To focus solely on one aspect of the IRES neglects the true value of the commodities provided. Other beneficial aspects of the IRES should be properly taken into account, specifically the eco-friendly emphasis and low fuel cost of the technologies compared to alternatives, especially when conducting cost benefit analysis and evaluating the overall impact of the system [21] [22] [28] [29] [30].

The optimisation of multiple renewable energy sources can overcome the stochastic quality of one form of generation with another. Also, reduction to the overall cost of energy of the system can be achieved by maximising the generating capacity of the cheapest renewable source of energy [22]. 2016 studies of IRES for remote areas in India found that gasification from biomass was the major source of power generation for all four areas of the study [27] and that locally available renewables were the most cost effective sources of energy [24]. It has already been shown that stand alone IRES are a cost effective form of electrification for remote communities that are inaccessible by grid [26] [27].

In some configurations of IRES that utilise batteries as the choice of energy storage the conversion losses due to the charging/discharging cycles decrease overall efficiency and increase energy cost [31]. Optimisation can help achieve a continuous power supply without problematic failures [24], with control optimisation and careful selection of multiple energy sources a 24 hr base load demand can be catered for [29].

The correct choice of renewables must be kept in mind as increasing variability in the system worsens demand satisfaction and increases the need for extra capacity, which in turn increases capital cost. There is a trade off between the reliability and performance of a system and the cost associated with it [25], which is to be expected.

2.6 Integrated Renewable Energy Systems Incorporating Desalination

A 2015 paper in the journal Desalination reviews the current IRES technologies involved with desalination, highlighting various innovative, low energy desalination processes [32]. Multi-generation IRES can provide desalination throughout the day, with multiple outputs from the same system improving overall system efficiency [35]. IRES providing additional commodities are more sustainable and reduce primary energy sources at suitable levels for communities or small commercial applications [36].

To summarise an IRES that has more than one source of generation provides energy security by building in redundancy and increases system efficiency. The use of desalination as a way of embedding energy storage through the propagation of biomass stock alleviates the intermittency issues associated with renewable energy. Systems that have multiple product outputs increase overall utility and system sustainability. System efficiency is maximised when generation can be optimised to suit demand requirements. System value is maximised and overall cost of production is greatly reduced when using biowaste as the biofuel input. This could be in the form of agri-crop residue such as the stems of wheat or straw crops. Such systems are ideally suited for off grid communities and small holdings.

2.7 Previous Work: The Dowerin Integrated Renewable Energy System

In 2016 Michael O'Brien was part of a two stage project working along side Dr Noel McWilliam of Mitravitae to construct, test, ship to and commission an IRES in Australia for field trials. The first stage was to construct and test a multi-generation system based on photovoltaic and biogas from biomass with RO

desalination at Exeter University. Upon successful completion the second stage was initiated. The system was shipped to a small holding in Dowerin, Western Australia, where it was commissioned for field trials. The system provided three separate commodities; clean water, electricity and gas.

2.7.1 Dowerin and The Silent Flood

The subterranean topography of Australia is bowl-shaped, leading to salt precipitation from the surrounding ocean migrating inland. This salt accumulates in the aquifers and water tables, contaminating the land and creating significant challenges for crop growth in the wheat belt of Western Australia.

Historically, there has been sufficient average rainfall to naturally irrigate crops. However, due to the lack of humic content in the soil substrate and the absence of root-bearing vegetation to manage water levels, crops struggle to grow. This phenomenon is known as the "silent flood" [93].

To combat this issue, farmers have resorted to digging extensive trenches, draining higher ground farmland into lower-lying regions. As more land becomes unusable, smaller farms go bankrupt and are absorbed by larger farms that can endure losses for longer periods. These larger farms then have more land to use as salt dumping grounds. Unfortunately, as this problem continues to escalate, the current business model is proving unsustainable.

The town of Dowerin, located three hours northwest of Perth in wheat belt country, is particularly affected by the silent flood. It presents an ideal location for field trials of Mitravitae's Integrated Renewable Energy System (IRES), which aims to address these agricultural challenges

2.7.2 A Photo Journey: from Exeter to Australia

Figure 2.7.1: Michael O'Brien receiving training on the BioGen at Exeter University's Cornwall Campus, Tremough.

Figure 2.7.2: Preparing the system for international shipping. Note three RO pressure vessels, the full Spectra Watermaker kit including the Clark, a low pressure CAT pump, power converter and high-pressure pump controller.

Figure 2.7.3: Good bye, England. Hello, Australia.

Figure 2.7.4: The Dowering farmstead with adequate water containment capacity. The Dowerin landscape.

Figure 2.7.5: The first task was to build suitable shelter for the IRES.

Figure 2.7.6: Commissioning the IRES in its new home.

Figure 2.7.7: Salt drainage trench excavation in action.

2.7.3 A PhD Born from a Field Trial

As discovered from this field trial, electrical generation technologies reliant on biogas present challenges and obstacles that require surmounting if auto-production is to be actualised. Low efficiency, robust technology is a prerequisite due to the poor quality of biogas. In the case of biogas produced by gasification, high contaminant content in the form of carbon dioxide, $CO_2 \leq 40\%$, and hydrogen sulphide, $H_2S \leq 1\%$, both forming acidic solutions in the presence of H_2O, are not only detrimental to the system downstream but also reduce the energy density of the gas and prohibit the use of more sophisticated energy efficient technology. With the removal of contaminants and particulates from the gas stream, high efficiency power generation fuel cell technology could be incorporated to system design, vastly improving overall efficiency and helping maximise the feedback gain.

As already discussed the individual efficiencies of each stage of the process need to be maximised. A Clark pump was used as a pressure exchanger to recover energy from the RO reject stream. The mechanical piston to stroke ratio of the Clark is 1:10, and it is this volumetric ratio that dictates the recovery ratio when using the Clark device. To overcome this limited means of production a secondary high pressure pump was installed on the feed line. Any additional flow into the RO unit via the secondary pump had a volume to volume increase in permeate output. In this way the recovery ratio could be controlled. Unfortunately high pressure pumps a major source of energy consumption contributing upto 50% to the specific energy of consumption, SEC. Reducing the cost of energy of the high pressure pump or omitting its use all together by developing a novel energy recovery device became an apparent essential step in increasing overall efficiency of the system.

In addition to maximising the feedback gain and reducing the SEC of desalination there was a quality control problem. In the instance where there is a possibility of a no biomass component in the first cycle of generation and water production,

the power supplied to the RO is, by nature of the PV, intermittent. How the RO responds to this dynamic input leads to a variance in permeate TDS levels i.e. water quality. A deskbased research exercise into dynamic models of RO systems showed that global research on the matter was lacking. Therefore, devising a dynamic model for PVRO systems would be worthy of further investigation.

3

Project Aims & Objectives

The Design & Prototyping of Interface Technologies for Integrated Renewable Energy Systems

Millions of people suffer from lack of access to clean water and affordable energy. A standalone, self sustaining, photovoltaic- reverse osmosis, PVRO, + biogas generator system had been proposed to alleviate water stress and provide electricity. Achieving commercial success of the system relies on enhancing overall efficiency by reducing energy consumption and increasing production. The aim of this thesis was to assess the processes of the system, investigate ways to enhance value and deliver technologies that do so. A lab-based test rig emulating a PVRO system was designed and constructed to evaluate the system's inputs and outputs. An energy recovery device was prototyped, installed, tested and analysed. System identification experiments were conducted and a black box model was inferred to predict membrane performance under dynamic conditions. A novel modelling approach was developed and verified.

A battery-less desalination IRES based on PVRO + a biogas generator produces three commodities, water, electricity and gas. The biogas generator component alleviates the intermittency of the solar component. Poly-production not only increases the utility of the system but also embeds a storage capacity in the form of water production. Flexibility in production also allows the outputs to

be tuned to the demands of the user, embedding a demand side management element, which increases overall efficiency. The operation of the system can be used holistically, in conjunction with permaculture techniques that produce a localised increase in water quality and soil reparation. Thus, IRES have the potential to green the desert. The correct design and operation of an IRES embeds a positive feedback gain, delivering geometric growth of the outputs per crop cycle. To ensure positive gain, the efficiencies of the inter-stage conversions of energy, i.e. sunlight to electricity, electricity to water, water to biomass, biomass to biofuel, biofuel to biogas and biogas to electricity, must be optimised.

Field trials of said IRES have shown that the biogas generator is a main cause of O&M downtime. High pressure pumps account for approximately 70% of the total energy consumption of RO systems. Investigation into the potential of waste energy recovery to mitigate the issues of the biogas generator and energy intensive pumps is an essential factor of the positive feedback gain.

Steady state system models that describe RO are abundant in literature, dynamic models less so. As there well maybe occurrences of the desalination component being powered solely by solar, a dynamic model predicting the performance of the system under power supply variance conditions, including permeate product quality, would contribute to dynamic modelling of pumped hydro systems worldwide.

In light of these challenges and opportunities, this research aims to explore innovative solutions to enhance the efficiency and reliability of the integrated renewable energy systems (IRES). By focusing on the development and optimisation of energy recovery devices, dynamic modeling techniques, and system identification, this study seeks to address key technical hurdles. Specifically, the following research questions were formulated to guide the investigation and provide a structured approach to achieving the overarching goals of improving system performance and sustainability.

Can an energy recovery prototype be built to interface with the IRES in a way

that reduces the specific energy of consumption of desalination?

Can a model be inferred from input/output data to determine optimal operating conditions to maintain permeate water quality?

Can a novel modeling technique be developed to simplify the complex, non-linear, and time-invariant dynamic relationships within the system

3.1 Research Goals

In the face of widespread challenges surrounding access to clean water and sustainable energy sources, the development of innovative technologies holds immense promise. With millions of people worldwide experiencing water scarcity and energy insecurity, there is a pressing need for solutions that are both effective and environmentally sustainable. In response to this urgent call, this research endeavors to explore novel approaches in the field of integrated renewable energy systems (IRES) with a specific focus on photovoltaic-reverse osmosis (PVRO) technology augmented by biogas generation.

Central to this investigation is the design and construction of a laboratory-based test rig that faithfully emulates the intricacies of a PVRO system. This test rig is envisioned not only as a means of performance benchmarking but also as a platform for experimentation and innovation. By incorporating high-frequency data logging capabilities and ensuring adaptability within budget constraints, the test rig becomes a versatile tool for exploring various aspects of PVRO technology, including the integration of energy recovery devices (ERD).

Furthermore, this research seeks to evaluate the untapped potential of waste energy within the PVRO system. By assessing and harnessing this waste energy, new avenues for enhancing overall system efficiency and sustainability can be explored. This exploration culminates in the design, construction, and testing of an ERD prototype, leveraging waste energy to augment the operation of the

PVRO system.

In parallel with these practical endeavors, rigorous theoretical groundwork is laid through the development of a black box model of the PVRO system using system identification (SI) techniques and MATLAB. This model serves as a foundational framework for subsequent analyses and simulations, facilitating a deeper understanding of the system dynamics.

Central to the overarching goals of this research is the development and validation of a dynamic model that accurately captures the complex interplay of variables within the PVRO system. By assessing the robustness and accuracy of this dynamic model against observed real-world dynamics, valuable insights can be gained into the performance and potential optimization of PVRO technology within integrated renewable energy systems.

Through a combination of practical experimentation, theoretical modeling, and rigorous analysis, this research endeavors to contribute to the ongoing quest for sustainable solutions in water and energy resource management. By pushing the boundaries of innovation and exploring the synergies between renewable energy technologies, it is hoped that this work will pave the way towards a more sustainable and resilient future.

With this overarching vision in mind, the research goals outlined below serve as a roadmap for achieving the objectives laid out in the preceding narrative. Each goal represents a critical step towards advancing our understanding of PVRO technology within integrated renewable energy systems and unlocking its full potential for addressing pressing global challenges.

Goal 1 Design and build a lab-based test-rig emulating a PVRO system: This foundational goal entails the creation of a versatile experimental platform capable of faithfully replicating the intricacies of PVRO technology. Key considerations include high-frequency data logging capabilities, cost-effectiveness, and adaptability for future investigations, particularly

concerning the integration of energy recovery devices.

Goal 2 Performance benchmark the system under a range of operating conditions: By subjecting the test rig to a variety of operational scenarios, with the aim to systematically evaluate the performance and efficiency of the PVRO system across different environmental and load conditions.

Goal 3 Assess the waste energy potential: This goal involves a comprehensive assessment of the untapped energy resources within the PVRO system, with a particular focus on identifying and quantifying waste energy streams that can be harnessed to enhance overall system efficiency.

Goal 4 Design, build, and test an ERD prototype based on waste energy: Building upon the insights gained from the waste energy assessment, this goal entails the development and testing of a prototype energy recovery device tailored to exploit these identified energy sources.

Goal 5 Define black box model of PVRO system using SI techniques and MATLAB: This theoretical endeavor involves the development of a comprehensive black box model using system identification techniques and MATLAB. This model serves as a foundational framework for subsequent analysis and simulation efforts.

Goal 6 Evaluate the inputs and outputs for a dynamic model: To inform the development of a dynamic model, this goal focuses on gathering and analyzing data related to the inputs and outputs of the PVRO system under various operating conditions.

Goal 7 Develop and validate a dynamic model to assess its robustness and accuracy: Building upon the theoretical groundwork laid in goal 5 and the empirical data gathered in goal 6, this objective entails the development and validation of a dynamic model capable of accurately representing real-world dynamics.

Goal 8 Evaluate model results vs observed results: Finally, this goal involves a critical evaluation of the dynamic model's performance against observed real-world data, providing insights into its robustness and predictive capabilities.

Collectively, these research goals constitute a multifaceted approach towards advancing the understanding of PVRO technology within the broader context of integrated renewable energy systems. Addressing these goals systematically and rigorously will contribute towards the development of sustainable and resilient solutions for water and energy resource management.

4

The System: simulating a photovoltaic-reverse osmosis unit in the lab

---

This chapter describes the lab based test-rig that was built specifically to emulate a battery-less PVRO system. The test-rig was designed and developed for the purpose of experimentation, validation and, adaptation for the advancement of IRES. The goal of this project is to investigate, explore and develop interface technologies that impact the utilisation and performance of IRES and improve the understanding of dynamic processes within the system due to the stochastic nature of the power supply i.e. solar irradiance.

The following Section 4.1 explains the initial PVRO test-rig, the component used along with a schematic of the set-up. This is followed by the technical specifications of the equipment and, where pertinent, the motivation behind the purchase decisions

A summary of technical specifications in Section 4.3 detail the instrumentation used to monitor the system variables required to parametrise the system's inputs and outputs, see Table 4.1. These are;

- the power supply unit, PSU, voltage and current; V_{psu} and I_{psu} respectively.
- the flow rates, Q, of the feed pump, RO reject line and RO permeate

production; Q_{feed}, Q_{reject}, and $Q_{permeate}$ respectively.

- the pressure, P, of the input feed to the RO and the reject output; P_{feed} and P_{reject}. Note pressure at the exit of the permeate port is assumed to be 0.
- the salinity, S, in total dissolved solids in parts per million of the feed, reject and permeate flows; S_{feed}, S_{reject}, and $S_{permeate}$ respectively.
- The temperature, T, of the feed and permeate, T_{feed} and $T_{permeate}$

Table 4.1: Table identifying and naming the input:output variables and the chosen SI units that are used in this document going forward

Variable	**Name**	**Unit**	**Input/Output**
PSU voltage	V_{PSU}	V	I
PSU current	I_{PSU}	A	I
Feed flow	Q_{feed}	l/s	I
Reject flow	Q_{reject}	l/s	O
Permeate flow	$Q_{permeate}$	l/s	O
Feed pressure	P_{feed}	MPa	I
Reject pressure	P_{reject}	MPa	I/O
Feed TDS	S_{feed}	mg/L	I
Reject TDS	S_{reject}	mg/L	O
Permeate TDS	$S_{permeate}$	mg/L	O
Feed temperature	T_{feed}	°C	I
Permeate temperature	$T_{permeate}$	°C	O

The system was benchmarked over a range of power inputs to establish the base performance under normal operating conditions. The performance of the pump was compared to the manufacturer's data sheet. Salt rejection performance of the membrane was tested at two different levels of feed saline concentration. The results of which are discussed in Section 4.5 along with the efficacy of the instrumentation to capture the results and how this influences the design of experiments going forward.

4.1 The Lab Set-Up: a full breakdown

The lab set-up is a test rig based on the IRES Mitravitae implemented in the field, in Dowerin, Australia. The Dowerin IRES utilised the Clark pump and secondary high pressure pump method, which increases the RR by injecting a secondary high pressure feed in parallel to the RO input, previously discussed in Chapter 2. Power generation for the IRES is initially supplied by the solar component as a means to desalinate water for crop production until such time as the first yield of biofuel is ready to supplement electricity generation. This thesis does not consider aspects relating to the production of crops, processing of biofuels or the generation of power from the biofuel component, hence the gasifier as described in Chapter 2 will not form part of this test rig or focus for further study. As already noted, the work focuses on theoretical and technological improvements to the solar desalination subsystem. Specifically the focus is on PVRO solar desalination as these are the technologies that underpin the IRES deployed by Mitravitae.

A lab based system mimicking the processes involved in a basic PVRO system was commissioned at the Flume Lab 01.20, University of East Anglia. The flume lab has adequate floor drainage and appropriate double-door access for installing larger pieces of equipment.

The test-rig consisted of a submersible pump suspended in an indeterminate bulk container, IBC, a $1m^3$ tank. The pump was powered by a rectifier and controlled by a solar pump controller.The rectifier supplied mains rectified DC to the solar pump controller. The solar pump controller could be set to apply a current adjustment to maintain maximum power being supplied to the pump. The pump flow feeds an RO unit. The flow is separated across a semi-permeable membrane, exiting the RO unit in two separate flows; a high saline 'reject' flow and a low saline product flow, 'permeate'.

The initial configuration omitted the Clark pump, see Figure 4.1.1. This was for

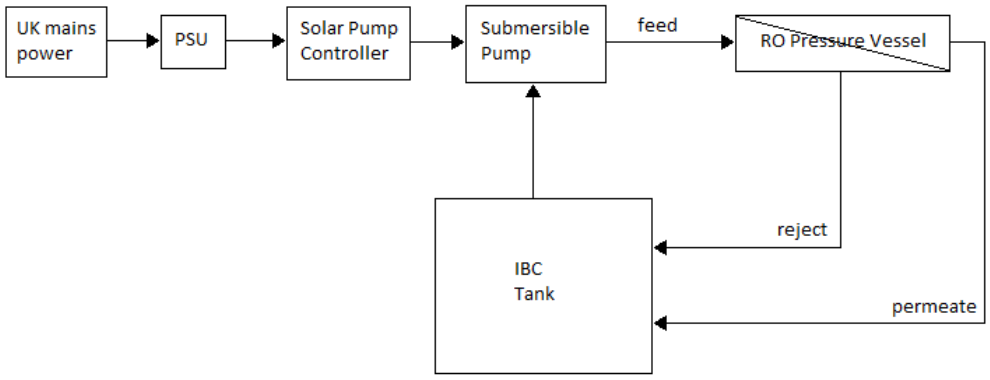

Figure 4.1.1: Initial configuration of lab based set up

several reasons:

- testing of the fundamental components prior to adding complexity to the system
- benchmarking the performance of the basic system without energy recovery
- calibration of the pressure and flow sensors
- design, implementation and iterative improvement of the data acquisition system
- understanding the limitations of the system
- familiarising controls and operation of the system

4.2 Reverse Osmosis

Desalination by reverse osmosis is a process where particulates, ions, and salts are removed from a liquid, by hydraulically forcing a feed fluid across a semi-permeable membrane. Water molecules diffuse across the membrane surface layer leaving a higher concentration fluid behind.

The process is energy intensive as high pressure is needed to maintain the hydraulic energy to overcome the osmotic pressure of desalination, which varies

depending on the temperature and concentration of the feed fluid.

4.2.1 Membranes

Thin film composite spiral wound membranes are the most common type of membrane. These membranes are industry standard and offer excellent rejection rates and robustness.

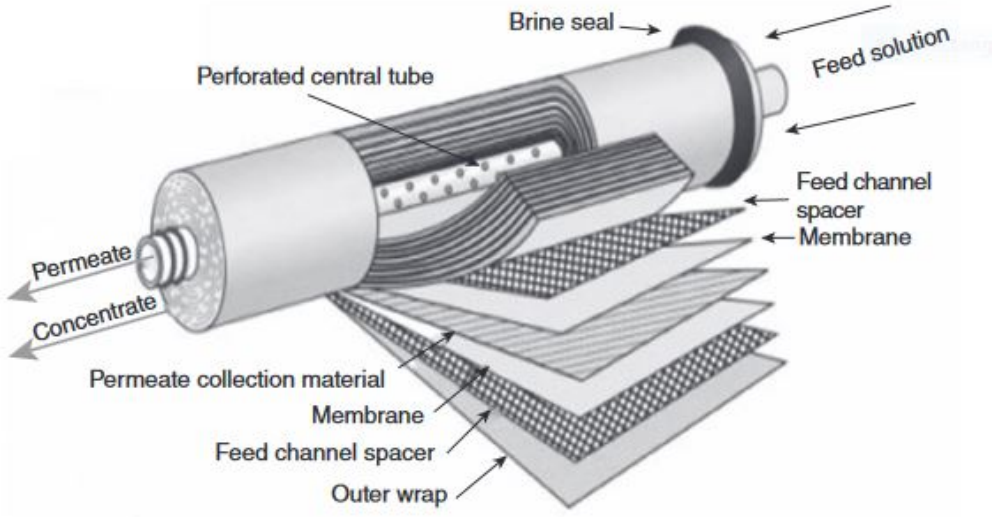

Figure 4.2.1: Components of a reverse osmosis spiral wound membrane

RO membranes are typically capable of removing 90 – 99% of contaminants such as total dissolved solids (TDSs) in the water supply. The membranes are usually manufactured as a flat sheet of thin composite membranes consisting of an active polyamide layer (high permeability but impermeable to dissolved salts and particulate matter)supported by a porous polysulphone layer wound round a central collection tube as shown in Figure 4.2.1. Osmosis occurs when two solutions with different concentrations are separated by a semipermeable membrane. In RO water purification systems, the osmotic pressure is overcome using hydraulic pressure, which is applied using a pump to the concentrated side. Water is then driven from the concentrated solution and collected downstream of the membrane.

4.2.2 Temperature Effect

Membrane performance is greatly effected by temperature. Thus, the temperature of the feed flow greatly effects permeate production. When temperature is increased for constant product flow the required pressure to drive the RO process is reduced at the expense of lower salt rejection across the membrane. For every degree Celsius increase in feed water temperature membrane capacity increases by 3%. [78]. At high temperatures, 55°C plus, membrane pore is altered increasing the permeate flux by up to 300% [79].

4.2.3 The Clark Pump

The Spectra Watermaker Clark pump, see Figure 4.2.2, from now on referred to solely as the Clark, is a pressure intensifier energy recovery device.

The Clark takes a low pressure feed and boosts it to provide the required pressure for reverse osmosis desalination to occur [63]. The Clark achieves this by recycling the energy in the pressurized RO reject. In the case of high saline concentration feed water, the embedded pressure energy exiting the RO unit can be up to 6.9 MPa [62]. The internal geometry of the Clark constrains the volumetric RO reject flow by 90%. This mechanism forces the feed flow to rise to a pressure greater than the osmotic pressure required for desalination. Embedding the ability of the Clark to automatically ramp up and down, adjusting to the concentration and temperature of the incoming feed flow, independently of user control. The Clark can operate with a low pressure feed of 0.4 pa, and can attain high pressures of up to 6.9 MPa. In this way the Clark is capable of capturing up to 97% of the 'waste' energy of the RO reject stream [61].

The Clark utilises two opposing reciprocal pistons that share a single rod. Although the concept of the double piston arrangement for RO applications was patented in 1979 [60], it was Clark Permar's valve-operating mechanism, licensed to Spectra Watermakers Inc in 1997 that made it a commercial success

Figure 4.2.2: The Clark pump

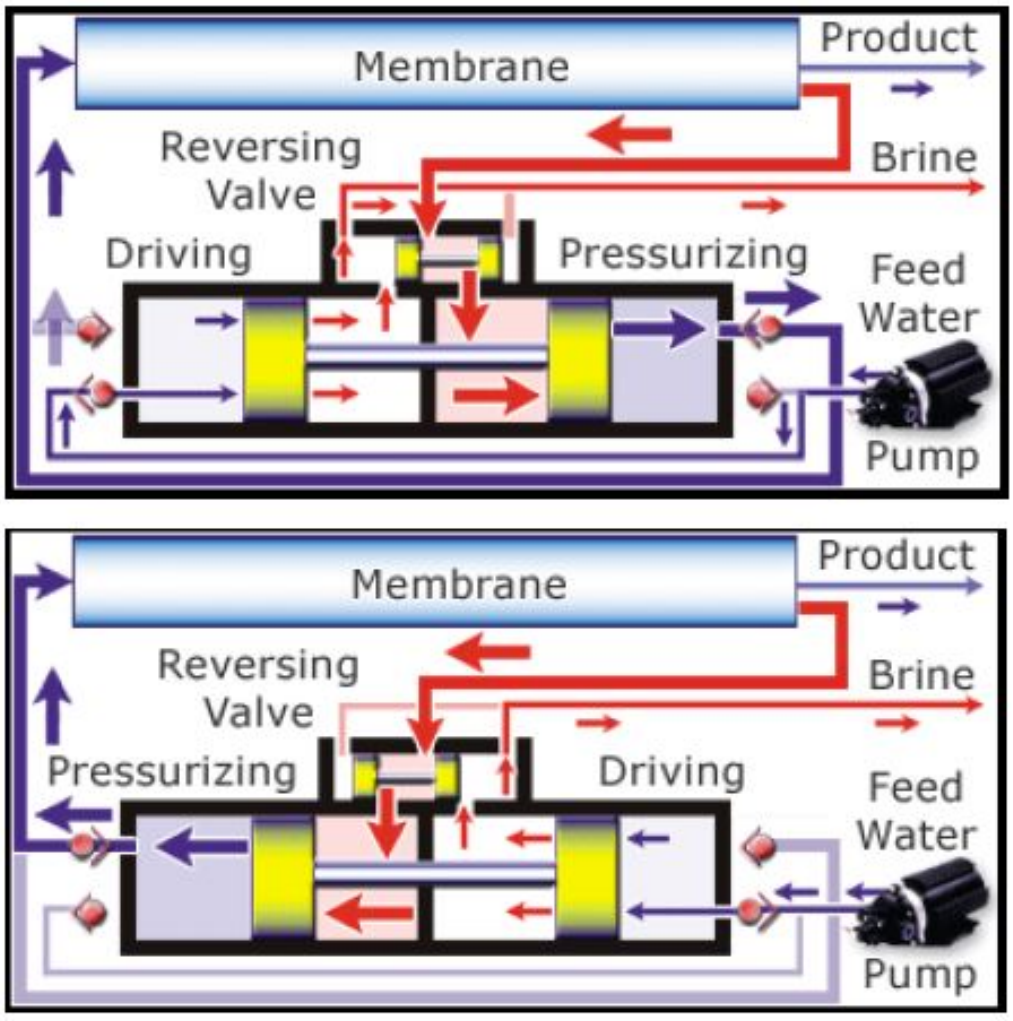

Figure 4.2.3: Clark pump operation

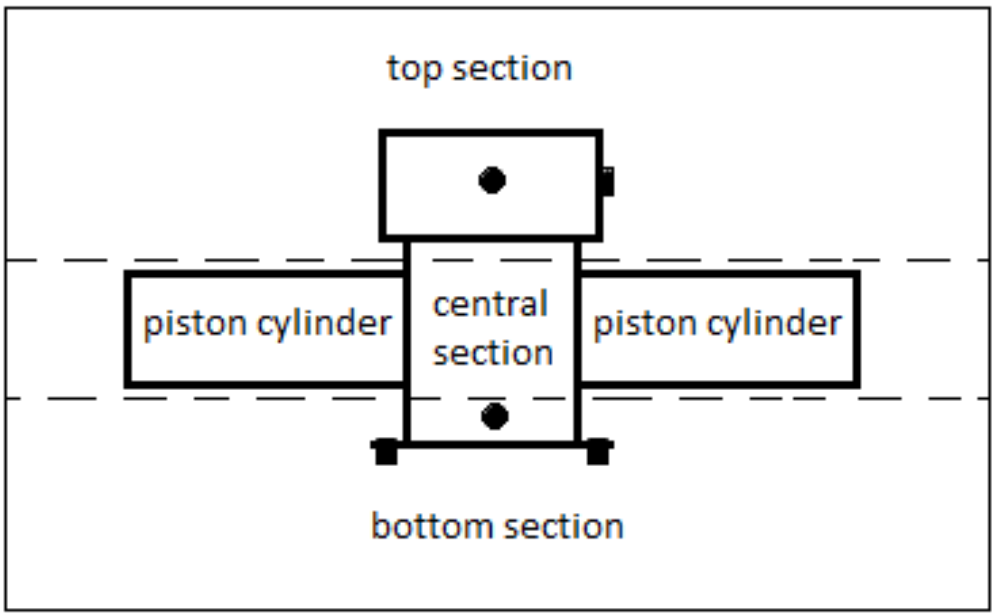

Figure 4.2.4: Sections of the Clark

[59]

How it works in detail: The Clark, although is a relatively simple mechanism, is hard to explain in text form. Possibly, a better understanding will be gained by viewing the diagrams in Figure 4.2.3. The Clark is a symmetrical device. Each side acts as the inverse action of the other. One side drives the pressurisation, exchanging energy from the RO reject to pump feed flow. The otherside exits the Clark, at high pressure, as the RO feed. Upon the return stroke of the piston, the side that was pressurised is now empty and starts to fill, becoming the driving force that pressurises the fluid on the other side. As one side fills the other side empties.

The top section of Clark is where the the valve operating mechanism is housed. The valve is a passive switching mechanism and switches the flow between the central section inner-piston-chambers see Figure 4.2.5. A internal spool assembly, embedded in the central block of the middle section, is actuated when the back face of a piston head returns to the centre block. Making physical contact with the end of the spool rod, pushing the spool assembly to oneside. Simultaneously closing off and opening up counter channels connecting the LHS

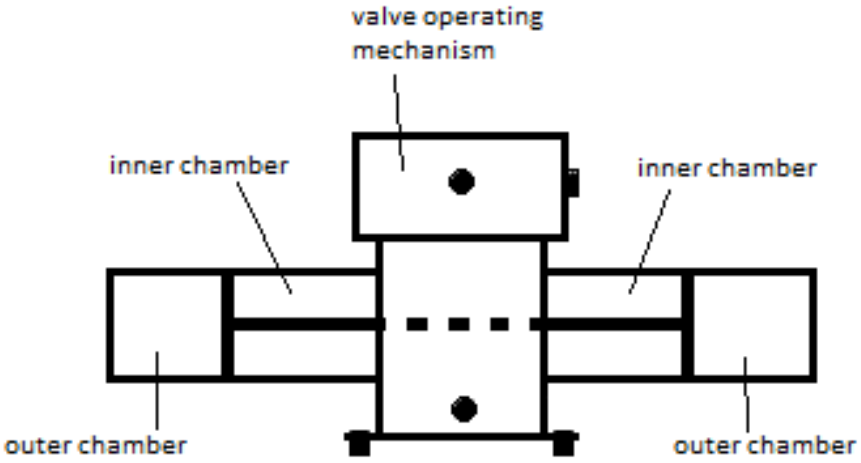

Figure 4.2.5: A visual reference to the 'inner and outer' chambers

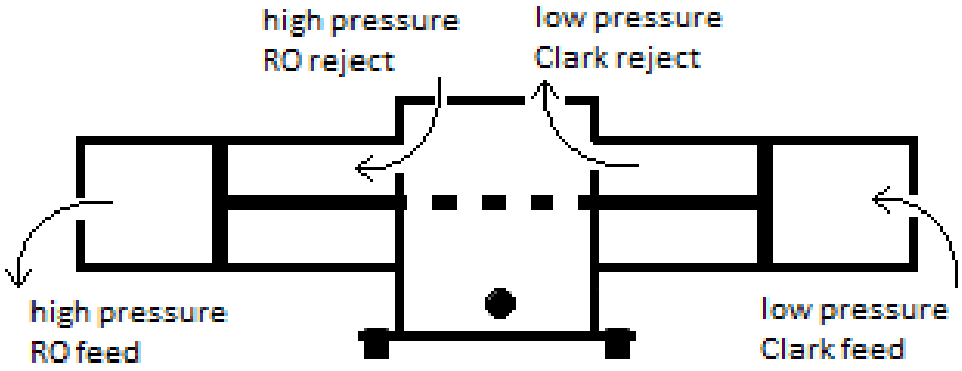

Figure 4.2.6: Flows in to and out of the inner and outer chambers

and RHS chambers of the central block to the top section of the Clark (the valve housing). A pressure differential occurs across the valve, and with the additive forces of the RO reject, forces the actuation of the operating mechanism, which in turn, switches the direction of flows into the inner chambers of the central section see Figure 4.2.5. The RO reject now fills the inner chamber, of a piston cylinder on oneside of the middle section, while the inner chamber of the piston cylinder on the other side, is being exhausted to atmosphere as Clark reject.

Flow enters the Clark from the feed pump at low pressure in the bottom section.

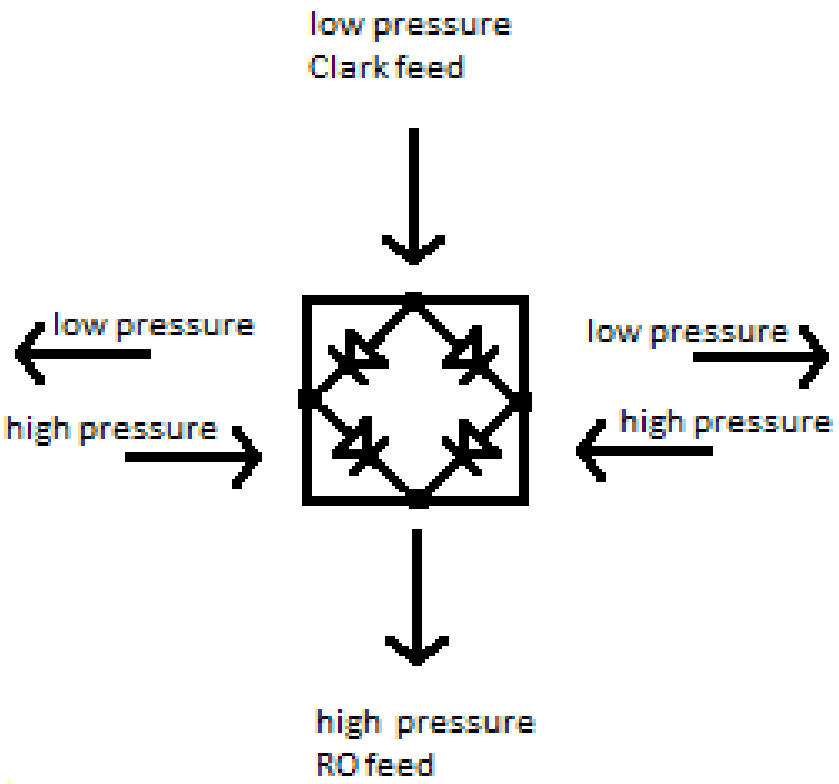

Figure 4.2.7: 'rectifier bridge', birds eye view of bottom section of Clark

Depending on the actuation cycle, it is drawn into one side of the piston cylinder's outer chamber while the fluid in the outer chamber of the piston cylinder on other side is being forced out at high pressure as RO feed.

While the pump feed is filling the outer chamber on one side the RO reject is filling the inner chamber on the other side. The forces from the feed flow and the reject flow are summative resulting in an exchange of energy being imparted to the RO feed exiting the Clark. At the end of a full piston stroke the switching spool rod is actuated, the flows are redirected, the roles of the chambers switch, i.e. the pressurising side becomes the pressured side, and the cycle begins again, see Figure 4.2.6.

The bottom section of the Clark, where the flow enters from the low pressure feed pump and the highpressure RO feed flow exits, maintains flow direction

with a split channel and two check-valves in series on both sides. The pressure differential either side of these four check-valves determines the direction of flow. The configuration is similar to a rectifier bridge in electronics that converts DC to AC, see Figure 4.2.7.

10% recovery ratio mechanism

Let the area piston head be $Ahead$. Let A_{rod} be the cross sectional area of the piston rod. Let l denote the length of displacement.

It follows that the value for l is the same for both chambers and the swept length of the cylinder is the same distance travelled by the piston rod, which is by definition l.

If we assume the internal diameter of the cylinder is equal to the diameter of the piston head, ergo, the cross sectional area of the cylinder is equal to A_{head}.

By design of the Clark we know $A_{head} = 10/9 * A_{rod}$.

When the piston is fully actuated one side of the piston cylinder has the internal volume of the outer chamber, V_{OC}, at maximum, and the internal volume of the inner chamber V_{IC} (of the piston cylinder on the other side of the centre block) is also at maximum.

$Volume = A*l$ therefore $V_{OC} = A_{head}*l$ and the $V_{IC} = (A_{head}*l) - 10/9*(A_{head}*l)$

As it can be seen from above, the 10% recovery ratio is fixed due to the cross sectional area of the piston rod. Spectra offer other models that incorporate the Clark with different RR based on the size of cross sectional area of the piston rod; 7%, 15% and a 20% but this is just 2x the 10% recovery option [64]. As the piston is enclosed within onside of the chamber that the piston head resides in. The other side of the chamber has the volume of the area of the piston head times the internal length L of the chamber when being filled and the piston actuates, the filling stroke. the side that is occupied by the piston with the same length L therefore occupies 10% of the chambers total volume on the return stroke,

thus forcing 10% of the total input flow into the Clark to be forced through the membrane as permeate.

100% of the flow leaves the Clark pressurised as RO feed. Due to the volumetric ratio between the inner and outer chamber of the Clark only 90% can return. 10% is forced across the membrane and exits the RO as permeate.

The pressure embedded in the returning flow enacts its force against the piston head of the inner chamber on one side of the piston cylinder. Simultaneously, the incoming flow from the feed pump is acting upon the piston head in the outer chamber of the piston cylinder on the other side in the same direction of force as the RO reject.

The forces combined pressurise the fluid exiting the outer chamber on the other side feeding the RO input. Due to the volumetric ratio of the Clark the fluid is forced to overcome the osmotic pressure of desalination no matter what that pressure is.

In this way the pressurised fluid is the sum of the pressure from the feed flow plus the additional pressure form the RO reject and as such will dynamically ramp up and down independently based upon the parameters of the feed fluid.

The coupling of the feed pressure with the RO reject pressure and the volumetric ratio between inner and outer chambers is what makes the Clark device capable of ramping up to 7 MPa, the desired level to overcome osmosis pressure of seawater, (70 bar, 1000 psi) with an initial input of only 0.7 MPa (7 bar, 100 psi) of pressure.

Ramping up: There are several potential modes of the ramping mechanism depending on initial starting conditions of the system.

As the membrane is confined in a fixed space, the internal volume of the pressure vessel, affects of membrane elasticity on storage are ignored with the assumption that full production is only achieved when all gasses (air) have been expunged from the pressure vessel.

When only considering the pressure vessel storage itself and assuming the fluid is Newtonian then there are two main possible ramping scenarios which will affect the time to full production of the system.

Assumptions 1) any volumetric storage capability of the membrane is ignored 2) the working fluid is incompressible

Scenario 1: Primed, both pressure vessel and Clark are fully primed

The mechanism for ramping up is instantaneous when the system is primed i.e. already is full of water. If 100% of the pressure vessel and all chambers of the Clark are completely filled with fluid upon start up then the pressure will increase to the point of overcoming the osmotic pressure required for desalination in in one stroke of the Clark piston.

Scenario 2: Non-primed, either or both the RO and Clark are not primed

Dry start up is ill advised for most membrane types as hydraulic shock to the membrane and cause mechanical damage to the fabric. A soft start is recommended to avoid damaging the membrane. A soft start is where the initial flow rate is low and increased to full over an extended period, minutes.

In this scenario the first cycle of the Clark piston stroke will push air into the RO unit as both piston cylinders are empty. On the second stroke the outer chamber that was being filled, now full, is being pumped to the RO but without the accompanying additive force of the returning fluid from the RO reject, as previously stated the RO is empty or more accurately the fluid is air at this point.

This cycle will continue until the Clark has displaced all the air from the system in the required amount of cycles to do so, $xcycles$. In addition, the fluid pressurised by the Clark leaving the outer chambers won't return to the inner chambers, completing one full round trip, until a minimum of 2 piston strokes has been completed. Therefore, in the case of starting the system dry the required pressure

to overcome osmosis of the working fluid will not be attained until two plus *xcycle* strokes of the Clark.

The pressure required to overcome the osmotic pressure of desalination dependant upon the fluid components as well as the condition of the RO membrane. Namely; the total dissolved solids, temperature, pH of the fluid and the biofouling and mechanical deformity of the membrane.

To summarise, the time taken to achieve full production depends on the initial starting conditions of the system, namely whether or not the components are primed. Whereas the level of energy required to reach full production is dependant on the constituents of the feed fluid and level of membrane degradation.

4.2.4 The Specific Energy of Consumption of Desalination

Desalination is considered an approach for mitigating water stress. Despite the abundance of saline water worldwide, additional energy consumption and increased costs present barriers to widespread deployment of desalination as a municipal water supply.

Specific energy consumption (SEC) is the standard metric in which the energy requirement of the desalination process is quantified. The SEC expresses the energy required to produce clean water in kWh per m^3, and is the biggest impact on the performance desalination, especially of overall process sustainability.

Overcoming osmotic pressure and forcing feed flow across the membrane is the largest contribution to SEC, usually varying between 60% and 80%. This is dependant on choice of technologies involved, system configuration, temperate, feed water salinity and composition. Ignoring the thermodynamic minimum of osmotic pressure additive SEC processes can be reduced to some extent, via improvement in technology, system design and optimal operation

4.2.5 Salinity, Total Dissolved Solids, Parts Per Million & Electrical Conductivity

There are different ways of discussing salinity due to the terminology of how to describe it and the methodology of how it is measured. Salinity was defined as the total amount of dissolved material in grams in one kilogram of seawater, which is a dimensionless unit of parts per thousand.

Total dissolved solids, TDS, is a measurement of the the amount in weight of substances dissolved in a volume of liquid and has a unit of mg/l, which can also be described as parts per million. Both terms are often used interchangeably but this ignores the specific gravity (density) of the liquid in question. The accepted density of water is approximately kg/l. With a ratio of 1:1 any conversion becomes unnecessary. But a liquid with a high concentration, e.g. sea water 35,000 ppm, has a density of 1.024 kg/l and a corresponding concentration of 35,840 ppm, in this case.

Meters and probes that measure salinity use the electrical conductivity method, which measure how well a material can conduct electricity. The amperometric technique. performed by passing a known voltage between two probes suspended in a medium, spaced a known distance apart and measuring the resistance. Resistance is the inverse of conductance.

Conductance (S) = 1/Resistance(ohm)

Conductance was originally measured in mhos, and later changed to Siemens (S). Conductivity is currently measured in Siemens/m. When measuring the conductivity of a liquid is often displayed as uS/cm.

As temperature effects the conductivity of a liquid most probes have an built in thermocouple that simultaneously measures the temperature. Allowing for adjustments to made post observation.

Throughout the following document salinity will be referred to as TDS in ppm

and conversion for the density of the liquid when it is pertinent can be assumed.

4.3 System Components & Technical Specifications

The technical specifications of the system components will now be discussed covering the technologies used in the lab-based test-rig. Each component will be introduced, describing its general purpose and context within the experiments of the PVRO system.

4.3.1 The Rectifier

In lieu of a PV panel a power supply unit, PSU, rectifying UK mains power (220-240V AC at 50 Hz) drove the solar pump controller. The initial PSU was a Chinese manufactured rectifier capable of transforming the alternating current, AC, input in to a range of direct current, DC, appropriate for the controller. The motivation for choosing this product, a low budget option with relatively rapid delivery, was for expediting the start of the experiments. This allowed more time for a thorough desk based investigation into PSUs capable of emulating real time solar irradiance to be concluded, while concurrently capturing data regarding the fundamental dynamics and performance characteristics of the system.

4.3.2 The Solar Pump Controller

The solar pump controller supplied with the pump has built in multi power point tracking, MPPT, capabilities that can be disabled manually. With MPPT enabled the controller adjusts the electrical load of the photovoltaic panel, or in this case a variable PSU, before converting it to 3-phase DC required for the operation of the pump. With MPPT disabled the controller passes through the power input with no load management being applied. In this first stage of equipment testing and calibration, the rectifier was not capable of being controlled

Table 4.2: Rated values of solar pump controller

Rated voltage	72 V DC
Rated current	12 A
Biggest open voltage (VOC)	100 V DC
Max power	1100 W
Starting voltage	36 V
Best working voltage (VMP)	60-76 V DC
Overload current	15 A
Over curent	17 A
Ambient temperature	20
Efficiency max.	98%

by an external input and could only ramp up or down its output depending on the demand of the load, which was effectively controlled by applying a back-pressure to the reject line.

The solar pump controller had a variable pot controlling the speed of rotation, a simple dial-knob that could be manually turned from minimum to maximum. Setting the controller to max disables the MPPT.

The solar pump controller was rated at 72 V and had a rated current of 12 A, see 4.2, which is an equivalent power output of 864 W. This was contrary to its rated power of 1100 W see Table 4.2. With a low starting voltage of 36 V and a 'best working' range between 60 -76 V combined with a max current (overload rating) of 15 A, gave a large power 'window' to test the pump in; 43 2- 1140 W. The top end of which is inline with the rated power.

4.3.3 The Pump

A submersible, permanent magnet synchronous motor (PMSM) driven (helical screw type), positive displacement pump was chosen for its dynamic response to input and load characteristics, continuous operation capabilities, high motor efficiency, ability to maintain pressure over a range of rpm and resilience to back-pressure.

The chosen model, the Feili Solar 4FLS4.2/120-D72/1300, has a power rating of 1300 W, see Table 4.3, well within the planned operational parameters, and although rated at 72 V can operate from $\geq$ 36 V. The rated maximum flow was 4.2 m^3/hr (1.17 l/s) with a maximum head of 12 meters (1.2 MPa)

Much like an IV performance curve of a PV panel, the pump's working pressure has a negative correlation with its flow rate, see Figure 4.3.1. As such when the pump is at its maximum with regard to flow rate the pressure is at a minimum and vice versa. Unfortunately, the pump curve performance data for the 4FLS4.2/120-D72/1300 was omitted from the graph.

Estimating from the extrapolated data; 70 m of head at 2 m^3/hr; 0.7 MPa at 0.56 l/s, appeared to be the optimal point on the curve that provides maximum flow and maximum pressure.

Table 4.3: Rated values of of the submersible pump

Model	4FLS4.2/120-D72/1300
Voltage (V)	72
Power (W)	1300
Max. flow (m^3/hr)	4.2
Max. head (m)	120
Outlet dia. (inch)	1

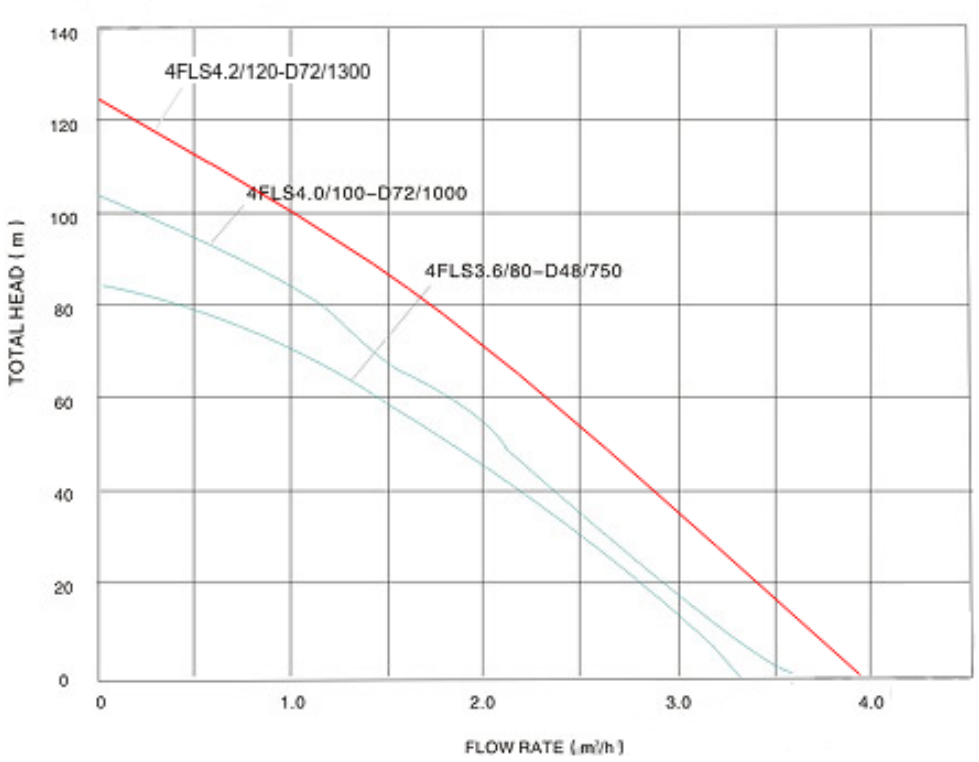

Figure 4.3.1: Estimated pump performance (in red) of model 4FLS4.2/120-D72/1300 taken from manufacturer's website. NOTE The red line is an extrapolation based on the other models.

4.3.4 Reverse Osmosis Pressure Vessel

The RO pressure vessel is a standard vessel for use with 4040 membranes, so called due to the dimensions in inches of the length and diameter of the membrane, 40" and 4" respectively. The body is constructed of glass fibre reinforced epoxy resin (GFRER) and has a working pressure of 1000 psi, equal to 6.895 MPa. Phoenix Pressure Vessels supplied the vessel and tested at 1.1 times the working pressure prior to dispatch. Epoxy resin has a bond strength of 3300 psi (22.75 MPa) and the maximum possible limit of the test rig was 6.9 MPa, with the planned experiments being well below this.

4.3.5 Reverse Osmosis Membrane

A low energy, spiral wound membrane was chosen for several reasons. The intended application, the Dowerin IRES, is for the treatment of brackish water, 1,000 - 5,000 TDS (although salinity of groundwater in and around the Perth region of Australia can reach up to 7,000 TDS). The extra low energy membrane, XLE-4040, performs well at low pressures. The XLE-4040 has a salt rejection rate of 99.0% with a feed concentration of 500 mg/l NaCl at 100 psi (0.86 MPa). These limits well within the operational range of the pump without additional energy recovery, which is optimal. The XLE-4040 can also be operated up to 41 bar (4.1 MPa), which allows for experimentation at higher salinities and with a Pressure exchanger enrgy recovery unit (Clark pump) incorporated to the system.

4.3.6 Indeterminate Bulk Container

A reinforced intermediate bulk container, IBC, approximately 1 m^3, with a capacity of 1,000 litres was used as the feed tank. All system output flows were routed back to the tank i.e. the brine reject and the permeate product water.

4.4 Instrumentation

Instrumentation to capture real-time flows and pressures was installed on the input and outputs of the system, see 4.4.1.

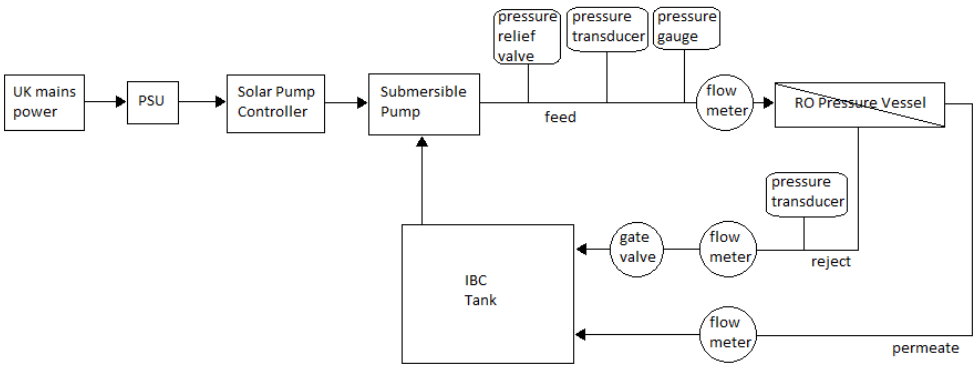

Figure 4.4.1: The lab based set up with instrumentation.

The feed, reject and permeate lines had inline flow meters installed.

The feed and reject lines had spur, pressure transducers, PTs, installed. The feed had an additional mechanical pressure gauge, PG, as a redundancy and fail-safe measure, allowing for continuous observation of feed pressure. As the permeate line was routed back to the tank, and free from obstruction no pressure instrumentation was installed, as it was assumed that the permeate would exit under atmospheric pressure i.e. 0 Pa gauge pressure. As with all RO operations the permeate is considered to be the end goal of the system and consequently all back-pressure on this line is to be avoided.

A pressure relief valve, PRV, was installed on the feed line in close proximity to the pump.

A gate valve was installed on the reject flow, allowing for the manual adjustment of the back-pressure that the system experienced. This is how different back pressure set points were achieved.

At this stage it was only possible to record power data manually by observing

the liquid crystal display on the front of the rectifier.

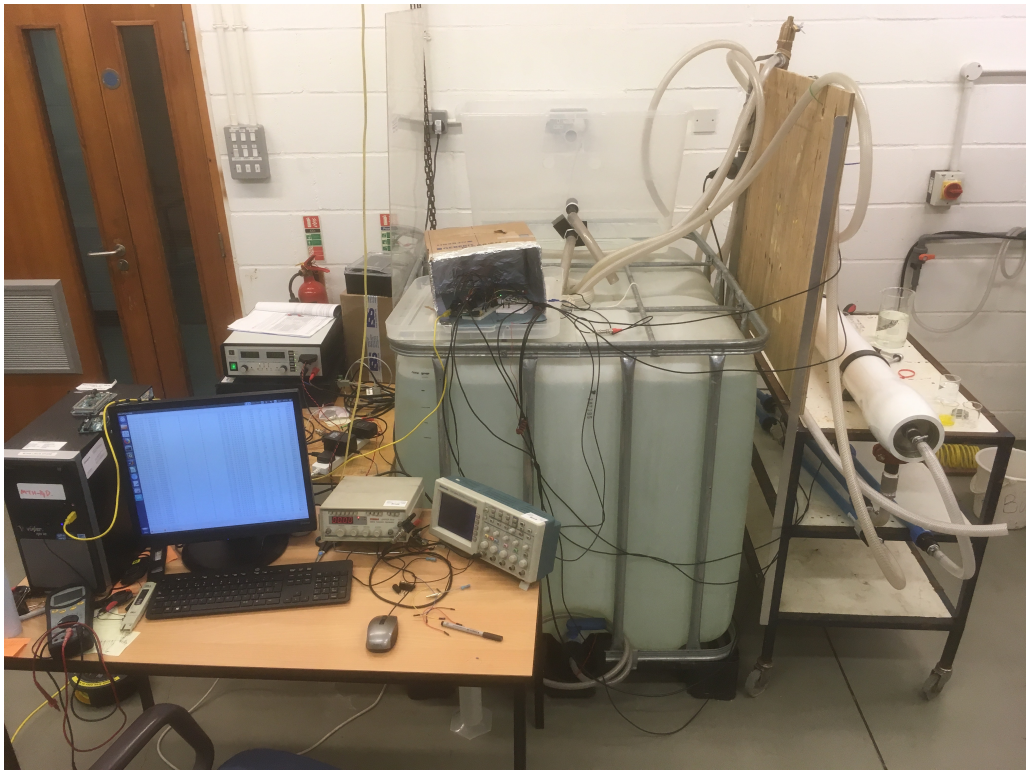

Figure 4.4.2: The lab set-up for benchmarking the reverse osmosis.

4.4.1 Pressure Gauge

A glycerol filled mechanical gauge reading a psi range of 0-150 (1.03 MPa) and a bar range of 0-12 (1.2 MPa) was installed on the feed line in close proximity to the pressure transducer. The glycerol acted as a hydraulic dampener, reducing the effect of vibration and ensuring a smooth sweep of the needle. The distance between the two was kept to a minimum in an attempt to reduce discrepancies in readings due to pressure drops caused by friction of flow and bends in the pipe. In practice, having two sensors of the same make and model, reading the same sample at the same time actually and agreeing with each other, is a rare occurrence. This is due to inconsistencies in manufacturing, margins of error being plus or minus and sensors having their own k curves.

4.4.2 Pressure Transducers

The same make and model, a Youtoo 5V0-1.2MPa three wire pressure transducer were installed on both the feed and reject line, PTF and PTR respectively, rated at 5 V and 1.2 MPa. The three wires are a red, five volt supply (Vin), a black ground (GND) and a yellow signal (S) wire.

4.4.3 Flow Meters

The three flow turbines in use are the FT2 Hall-effect turbine flow meter. The internal topology of the housing channels a portion of the flow into the path of a three-vane turbine whose rotational movement is picked up using Hall effect and transmitted as a series of pulses.

4.4.4 Pressure Relief Valve

As a safety precaution the pressure relief valve, PRV, was set at 12 bar (1.2 MPa). This was to protect the pump in the case of catastrophic back-pressure as the pump's rated maximum pressure is 1.2 MPa.

4.4.5 Gate Valve

A gate valve was in use as means of adjusting the back pressure to the RO reject. This was necessary in the first instance of testing, the benchmarking of the pump and calibration of the sensors, and for testing the effects of throttling the system without having to run saline feed through the RO unit. Evidently when using freshwater in the system there was no desalination taking place as there is little to no saline gradient. Therefore the osmotic pressure was negligible to non-existent.

4.5 Results & Discussion

Based on the manufacturer's data, see Section 4.3, the pumps optimal voltage is 72 V. The solar pump controller allows the pump to operate at a minimum input voltage of 36 V, with an optimal voltage range of 60 V – 76 V.

Discrepancies have been found between the pressure gauge and the pressure transducers. To avoid overloading the pump during the initial phase of testing, a maximum test pressure, as observed on the gauge, of 0.8 MPa was chosen. This value is safely below the pump's rated max pressure of 1.2 M Pa.

4.5.1 Flow, Pressure & Power Benchmarking

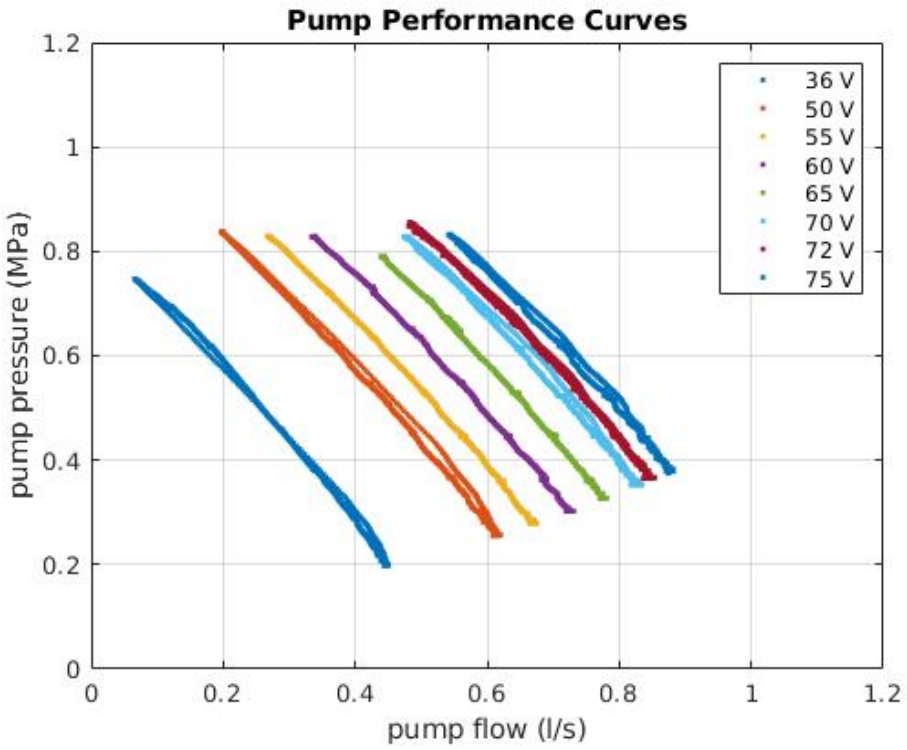

Figure 4.5.1: Flow versus pressure curves for all voltage setting data sets i.e. 35 V, 50 V, 55 V, 60 V, 65 V, 70 V, 72 V and 75 V.

Eight voltage set points were used to initially test pump performance, see Figure 4.5.1; 36 V, 50 V, 55 V, 60 V, 65 V, 72 V and 75 V, at pressure set points starting from the initial pressure at that voltage setting, i.e. no back pressure, up to 0.8

MPa of back pressure in 0.1 MPa increments. The back pressure was attained by manually closing the gate valve until the next pressure increment was observed on the pressure gauge. This lead to perturbations in the power reading that can be seen in Figure 4.5.1 as localised spikes.

Based on the pump data sheet, 36 V and 7 V were chosen as the minimum and maximum pump voltage, Vmin and Vmax respectively, as the lower and upper bounds of the performance testing. 72 V was to be used as a direct comparison to the data-sheet. Under load the pump would shut down intermittently at lower voltages. Through experimentation it was found that a voltage setting $\geq$50V worked well over a large range of pressures, 0.2 MPa - 0.8 Mpa. Hence, the 5 V increments starting from 50V onward. As the data shows the shape of the performance curve maintains uniformity across all voltage settings.

The pump performed as expected throughout. At the lowest voltage set-point, 36 V, the lowest flows and pressure were achieved but across one of the largest overall ranges. The next voltage setting, 50 V, had the same size of pressure and flow range as 36 V but at higher values. The remaining settings were at 5 V increments up to 75 V, except for the 72 V setting which is used to compare the information provided by the manufacturer's data sheet.

A quadratic line of best fit was applied to several points lifted from the data sheet and extrapolated over the rated flow rate range, see Figure 4.5.2. This 'estimated' line shows the pump achieving the stated 1.2 MPa maximum pressure and 1.05 l/s approx, which falls slightly short of the 1.17 l/s, 4.2 m^3/hr, the stated maximum flow rate. When compared with the empirical data gathered at 72 V the pump appears to underperform but the 75 V empirical data sits nicely within the estimated performance curve. The flow rate vs performance results are satisfactory with the slight discrepancies between the manufacturer's data and the empirical data at 75 V being negligible.

A higher voltage setpoint supplies more power to the pump. Consequently there is an increase in the steady-state flow rate, which in turn increases the initial

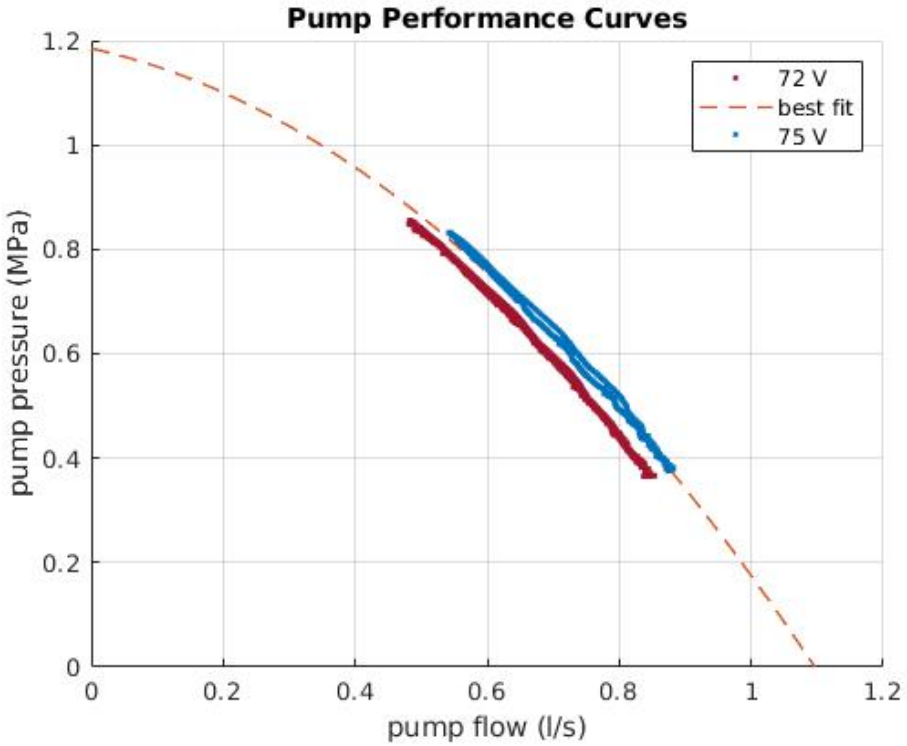

Figure 4.5.2: Pump performance comparison between the manufacturer's data sheet, the dashed line, and the two closest empirical data sets, 72 V and 75 V.

pressure experienced by the pump, as it forces the flow around the system at a greater rate. A greater pressure results in a greater load on the pump and a corresponding increase in current was observed coupled with a decrease in flow, figure 4.5.3 and figure 4.5.4 show this relationship; power versus pressure and power versus flow.

Figure 4.5.3 demonstrates the correlation between power and pressure being positively linear. It is clear from the graph that the 75 V data exceeds the 1300 W rated max power at slightly over 0.8 MPa. Forecasting is unnecessary to evaluate that both the 65 V and the 70 V data would exceed 1300 W prior to achieving the maximum rated pressure, 1.2 MPa. Only the lower voltages would achieve the maximum pressure but would tend toward a flow rate of 0. Both outcomes are undesirable.

The same can be observed in Figure 4.5.4. With voltage settings $\geq$ 7 V would exceed the power rating of the pump if the pressure were to be increased. These

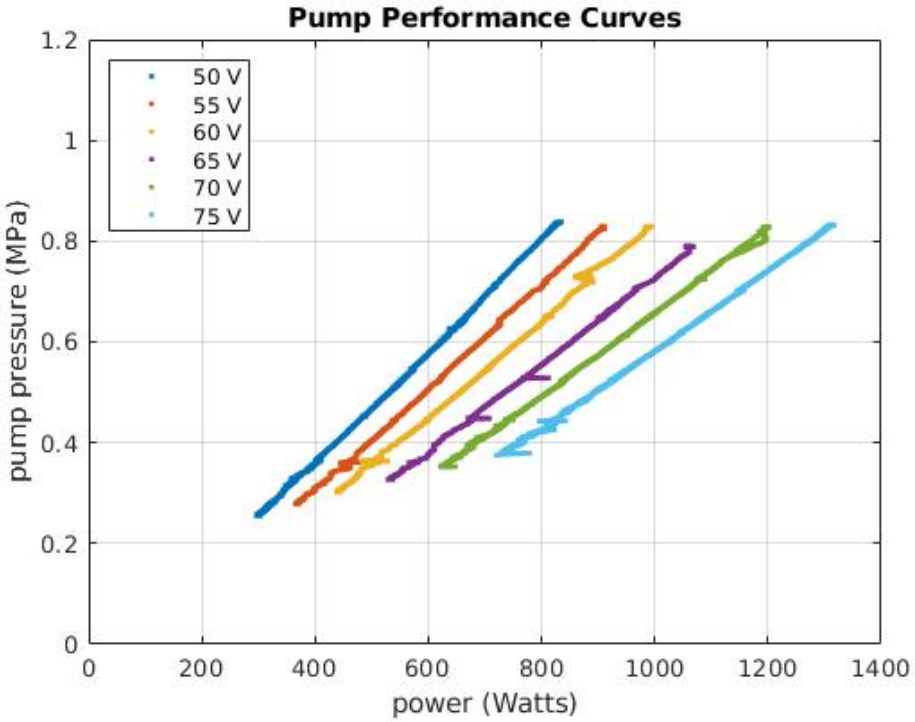

Figure 4.5.3: Power vs pressure curves for the 5 V increment data sets ie 50 V - 75 V.

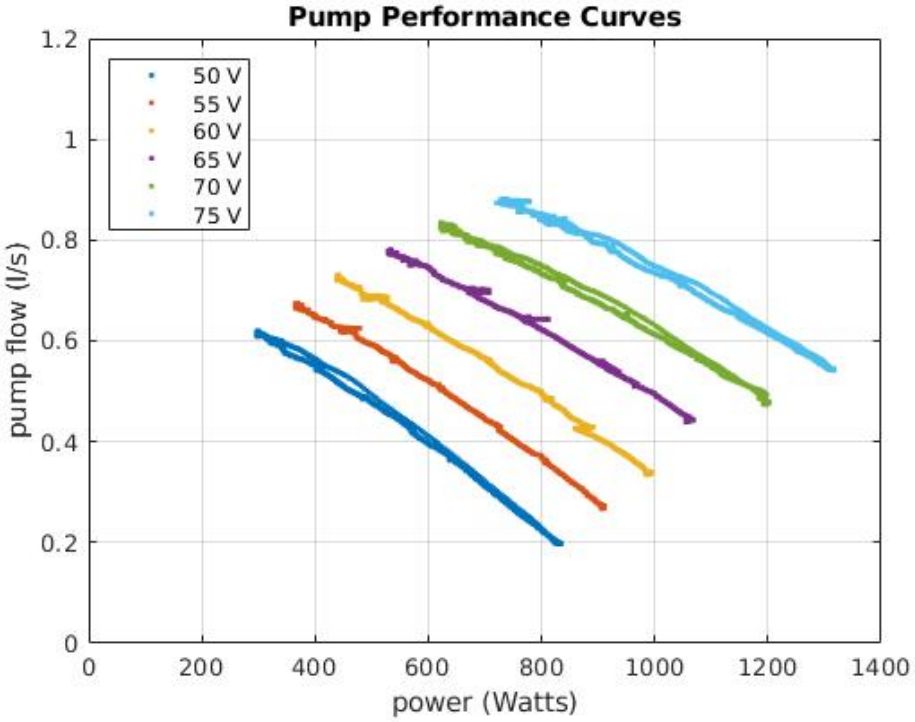

Figure 4.5.4: Power versus flow curves for the 5 V increment data sets i.e. 50 V - 75V.

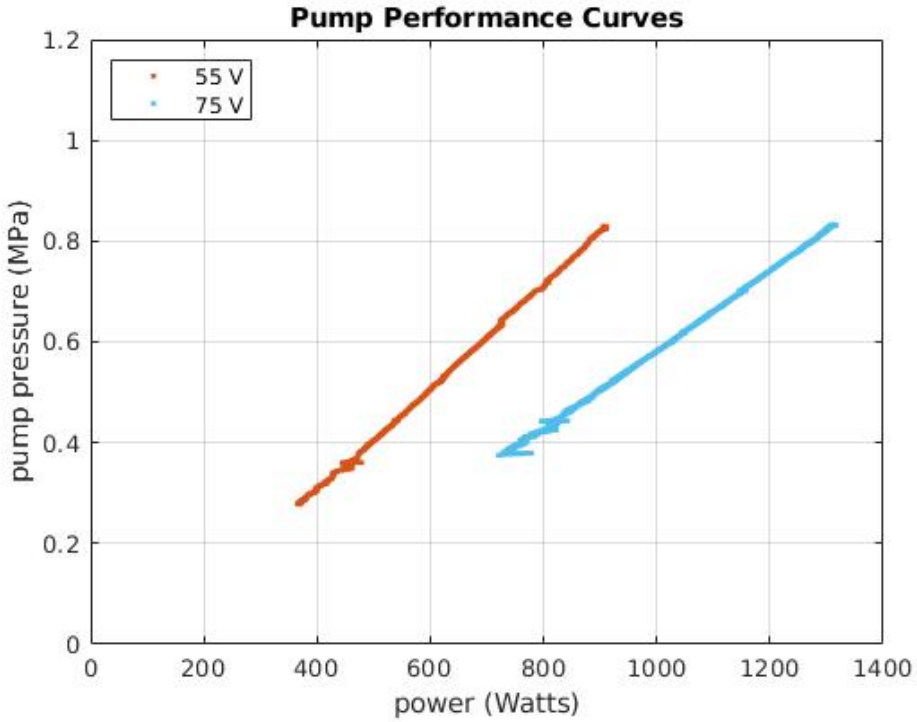

Figure 4.5.5: Optimal operating power versus pressure window; 300 W - 1300 W and 0.3 MPa - 0.8 MPa between 50 V and 70 V.

graphs show that back-pressure has the bigger impact on power consumption than higher voltage and, accordingly, pressure has the greater effect on the specific energy of desalination.

4.5.2 Optimal Operating Window

Figure 4.5.5 shows the optimal operating range between 50 V and 70 V. Due to points raised in the previous sections an optimal operating window was chosen with Vmin = 50V and Vmax= 70 V. The 50V -60 V range could be pushed, if needed, to achieve higher pressures of 1 MPa, while leaving head room for 70 V and above if later required.

4.5.3 Summary of Results

The pump benchmarking tests revealed several key performance characteristics essential for future experimentation. Five voltage setpoints were selected as optimal for subsequent tests. The pump demonstrated optimal performance within a power range of 300 W to 1300 W, handling flow rates between 0.2 l/s and 0.8 l/s and pressures from 0.25 MPa to 0.9 MPa. At higher voltage settings and low backpressures, the pump achieved greater flow rates, while higher pressures could be attained at the cost of increased power consumption and reduced flow rates, as anticipated.

Notably, increasing backpressure significantly impacted the pump's power consumption, thereby affecting the specific energy required for desalination. Operating the pump at pressures above 0.8 MPa with voltages of 70 V or higher exceeded the rated power, posing a risk of overheating. These findings highlight the critical balance between voltage settings, flow rates, and backpressures to maintain efficient and safe pump operation within the system.

5

Modelling System Dynamics: the reverse osmosis component

5.1 Introduction

Industrial reverse osmosis (RO) applications are typically designed to run at near constant production conditions that optimise energy consumption and cost. In contrast PVRO systems must operate across a range of conditions during the course of a day, with subsequent implications for production rates, product quality and energy efficiency. While battery banks have been explored as a means to smooth production in small-scale systems, the marginal gain obtained from diverting electricity for delay is quickly eroded by storage losses, thereby limiting the size of the bank and the scope for optimising production. Even under favourable circumstances batteries are highly inefficient and become more so as they age. This is a significant constraint in locations best suited to solar since high irradiance is concomitant with high temperatures. Heat enhances electrolyte losses and plate warping, causing discharge inefficiencies and localised overcharge, resulting in a steep attenuation in storage capacity with time. In some instances batteries may only have a 2-year useful life span. As such battery systems are considered a poor technological match with PV systems and for this reason consider herein the batteryless design of Thompson (2008). In this approach a Clark energy recovery mechanism is employed to successfully achieve efficiencies comparable to industrial scale RO systems.

Available power from the PV-array is not stored but fully utilised by the RO-system giving rise to variable feed and product flow rates, operational pressures and product quality. In this latter aspect the system performance must be optimised to comply with drinking water guidelines – it is necessary therefore to quantify system performance as a function of irradiance.

This Chapter provides an overview of the current state of the art with respect to equilibrium modelling of RO systems and note their similarity to Ohm's Law. Likening a membrane to an electrical resistor three candidate modelling approaches are formulated: black-box, structured "pure-resistance" and hybrid. The proposed "pure-resistance" model has the advantage of simplicity, but ignores any potential complex dependencies between variables that may be captured in the black-box approach. The "grey-box" hybrid approach utilises the parameterisations captured in the black-box model to compute equivalent resistances of the structured model, thereby affording some intuition behind the model performance.

For detailed discussions on system modeling techniques, including Bode plots, Laplace Transform analysis, and Fast Fourier Transform analysis, please see Appendix A.

5.2 Equilibrium Modelling of Reverse Osmosis Systems

RO systems are classically operated and modelled assuming steady-state conditions commensurate with typical implementations that assume near constant power supply.

The classic solution-diffusion model for reverse osmosis is:

$$Jw = A(\Delta p - \Delta \pi)$$

where Jw is flux across the membrane, A is the permeability of water which assumed constant, Δp is the applied pressure across the membrane and $\Delta\pi$ the osmotic pressure drop across the membrane [82]. One may consider the pressure differential $\Delta p - \Delta\pi$ driving the flux as analogous to a voltage potential. In this way the permeability constant A may be interpreted as an inverse resistance. Thus the model used to define equilibrium desalination has the same functional form as Ohm's Law: $V = IR$, perfectly describing the characteristics of a DC resistive load.

5.3 Dynamic Modelling & the Circuit Analogy

Due to the stochastic quality of irradiance any system that relies on solar as an input would benefit from a real-time prediction model, particularly PVRO systems. A model estimating RO feed pressures, flow and production rates, incorporating past and current solar irradiance and system pressures and flow rates, would be complex and highly dynamic. A potential solution is to leverage circuit analogy by establishing links between hydraulic systems, as in the previous section, that can capture the dynamical dimensions and deliver a robust but simpler translation of the system response for analysis and estimation.

5.4 Parametric vs Non-parametric Models

Parametric models are essential tools in engineering analysis, providing a mathematical framework to model complex physical systems. These models, often assume some finite set of parameters encapsulated in theta, θ. Once θ has been defined the future predictions of x, are independent of the observed data, D.

That is to say,

$$P(x|\theta, D) = P(x|\theta)$$

In ideal scenarios θ captures all the relations within D

In parametric models, the conditional probability $P(x|\theta)$ plays a fundamental role, representing the likelihood of observing a particular outcome x given specific parameter values θ and observed data D.

This conditional probability quantifies how the model's predictions are influenced by the known parameters and observed data, enabling informed predictions about future outcomes.

Case in point, consider a parametric model used to predict the performance of a PVRO system based on parameters such as voltage, current, flow, pressure, temperature and feed salinity properties. The conditional probability assesses how changes in these parameters affect the system's behaviour and predict its performance under different operating conditions.

However, it's important to acknowledge that the conditional probability assumes ideal conditions where the parameters accurately capture all relationships within the observed data. Deviations from these ideal conditions may introduce uncertainties in the model's predictions, highlighting the importance of carefully validating and refining parametric models to ensure their accuracy and reliability in real-world applications.

Non-parametric models assume that the distribution of D cannot be defined by a finite set of parameters. Non-parametric models are assumed capable of being defined by an infinite dimensional θ. As θ is a function, the amount of information it is able to capture within D is unbounded and therefore can increase to capture greater dimensions within D as D itself increases. Having θ unbounded allows for a model with a greater potential of depth to estimation for system response as the conditions pertaining to θ are infinite [80].

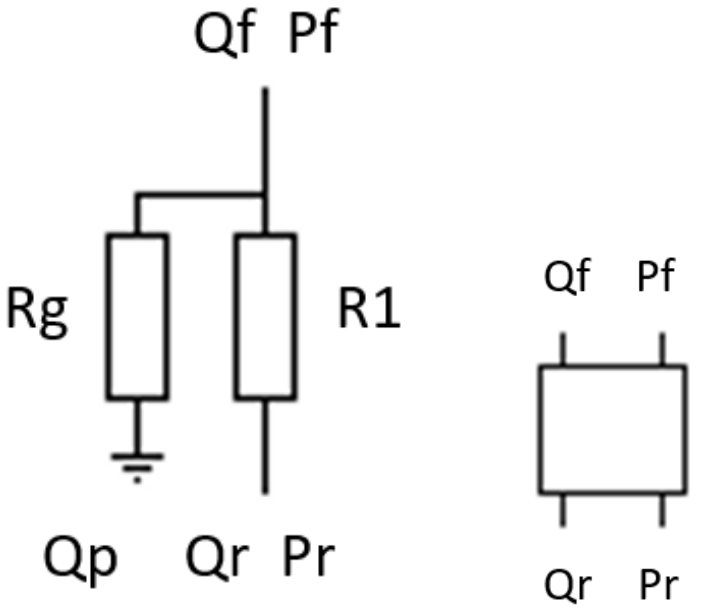

(a) (b)

Figure 5.5.1: (a) resistors in parallel model (b) black box model. Qf, Qp, Qr are feed flow, permeate flow and reject flow respectively. Pf and Pr are feed pressure and reject pressure. Rg and R1 are resistances to water flow through the membrane and across the membrane respectively.

5.5 Candidate Models

This subsection focuses on locally linear time-invariant models with a view to estimating the variation of these models with respect to appropriate factors. Each model will attempt to explicitly capture linear dependencies between input feed flows and pressures and output reject and product flows and pressures as a function of frequency and amplitude of the inputs. *A priori* it is expect our fitted models themselves to be a non-linear function of feed salinity and temperature. Ultimately the aim is to devise an amalgamated model, interpolating calibrated linear models across a range of salinity and temperature values arriving at a unified model accounting for linear and non-linear dependencies.

This chapter focuses on estimation of linear time-invariant (LTI) models of the following three varieties:

- Black-box: two inputs, two outputs, see Figure 5.5.1
- Structured Parametric: two resistors in parallel, also see Figure 5.5.1
- Hybrid: Structured Parametric

5.5.1 Black-Box Modelling

Black-box models make no attempt to represent a formal understanding of the system dynamics beyond those that might pertain to system size and the type of black box model chosen. In this approach only inputs and outputs and system size are specified and the model parameters are chosen to best fit the model output given the specified inputs. The state space representation of linear time-invariant continuous time black box models have the general form:

$$\dot{x}(t) = Ax(t) + Bu(t) + Ke(t) \tag{5.5.1}$$

$$y(t) = Cx(t) + Du(t) + e(t) \tag{5.5.2}$$

where $x(t) \in \mathbb{R}^n; n \in \mathbb{Z}+$ denotes the state space vector at time $t \in \mathbb{R}$, $A \in \mathbb{R}^{n\times n}$ is the linear state matrix representing the unforced dynamic of the state, $B \in \mathbb{R}^{n\times m}; m \leq n$ is the control matrix representing the influence of the control variate $u(t) \in \mathbb{R}^m; m \in \mathbb{Z}$ on the state space at time t and $K \in \mathbb{R}^{n\times p}; p \leq n$ is a disturbance matrix representing the influence of a random disturbance $e(t) \in \mathbb{R}^p$ on the state. Some or all of the state may not be directly amenable to observation and as such the state space representation distinguishes state $x(t)$ from observations $y(t) \in \mathbb{R}^q; q \in \mathbb{Z}$. LTIs assume observations are linear combinations of the state variables, the control variables and the error, respectively characterised by the matrices $C \in \mathbb{R}^{q\times n}$ and $D \in \mathbb{R}^{q\times m}$.

In control applications it is often easier to formulate the model in the frequency domain by taking the Laplace transform $U(s) = \mathcal{L}(u(t))$ of the inputs and the outputs $Y(s) = \mathcal{L}(y(t))$ and defining the "transfer function" transformation $G(s)$

such that

$$Y(s) = G(s)U(s).$$

5.5.2 Structured Parametric: resistors in parallel

In keeping with the circuit analogy an RO membrane offers distinct resistance to the two flows through the membrane. A water molecule first flows through the feed inlet into the pressure vessel containing a spiral wound semi-porous gelatinous membrane. Some molecules flow over the membrane, passing through and out of the vessel to be ejected as reject flow. Other molecules will pass through the membrane – either through micro-pores or diffusing through the membrane media. The feed flow therefore splits into reject and product. The resistance to flow through the membrane is substantially greater than the resistance to flow over the membrane surface – requiring a large pressure gradient. McWilliam (pers comm, 2017) suggested a circuit representation of an RO membrane comprising two resistors in parallel as depicted in Figure 5.5.1. Here $R_1(s)$ and $R_G(s)$ are considered functions of frequency whereby for any fixed frequency s assume Ohm's Law to hold — that is:

$$\Delta V_G(s) = R_G(s)I_G(s)$$

and

$$\Delta V_1(s) = R_1(s)I_1(s)$$

In this approach the resistance is in effect a one-dimensional transfer function from "current" (i.e. flow rate) to the change in "voltage" (i.e. delta pressure). This allows us to capture potential influence of disturbance on the resistance characteristics of the membrane. The phenomenon of "concentration polarisation" — the accumulation of ions of alternating charge at the membrane surface — is well documented in the literature, increasing resistance to flow of (polar) water molecules through the resulting electromagnetic field, ultimately

decreasing product flow. Disturbance in pressure or feed flows has the potential therefore to agitate and disrupt concentration polarisation gradients, with potential benefits to desalination productivity.

5.5.3 Structured Parametric: the hybrid model

The proposed "pure-resistance" model has the advantage of simplicity, but ignores any potential dependencies between feed pressure and the product/reject flow that are permitted in the black-box approach. The hybrid approach utilises the parametrisations captured in the black-box model to compute equivalent resistances of the structured model – in effect expressing the "Ohmic" resistances as an implicit function of feed pressure. In this way it is inferred that contributions to the resistance from the variation in feed pressure and feed/product flows thereby potentially affording some intuition behind the RO performance as a function of input frequency.

5.6 Methodology: initial input signals

IO data was attained by exciting the system at different Vpsu frequencies and amplitudes. The response behaviour was observed, which aided understanding to the factors that contributed to a change in the system.

The control inputs were PSU voltage amplitude, PSU voltage frequency and feed salinity. These would bare out through the system as pressure, flow rate and salt rejection.

The control input parameters have been established. Vpsu(theta) and Vpsu(Amp) effect the total flow and pressure being applied to the system, Qfeed and Pfeed respectively. Feed salinity (Sfeed) is indpendent of flow and pressure but permeate salinity (Spermeate) is a function of the relationship between Qfeed and Pfeed and the resistance to flow of the membrane. The

system outputs of RO reject flow, RO permeate flow and permeate TDS were monitored and the data recorded, Qreject, Qpermeate and Spermeate, respectively. From the resulting IO data SR, RR and SEC could be evaluated.

Note, while the system configuration incorporates the Clark, Qreject and Qpermeate return to the tank unrestricted and therefore the pressure i.e. Preject and Ppermeate are negligible and need not to be monitored.

Referring to the circuit equivalence model; the lab-based system has been defined as a electronic circuit. Each device having an equivalent electronic component. With pressure being analogous to voltage and flow being analogous to current. The flow coming from the pump having a high electronic potential and the flow returning to the tank having a low electronic potential (practicably exhausting to atmosphere at negligible pressure, which is assumed to be ground equivalent).

The system was monitored by several pressure transducers and three flow meters. The flow from the pump, the RO reject and the RO permeate were captured using Titan hall effect turbine flow meters. The low pressure side; i.e. reject pressure and pump pressure, of the system were monitored by two 0-1.2 Mpa (12 bar) pressure transducers. While the high pressure side, which consisted of anything entering or leaving the RO after the feed pressure had been amplified by the Clark, consisted of four sick sensors capable of reading pressures up to 10 MPa (100 bar). The PSU outputs, Vpsu, Ipsu and Ppsu were capable of being independently monitored via the rs232 port of the PSU.

Through testing it was determined that the Ppsu output was highly unstable. This had no impact as power could be evaluated via the reliable Vpsu and Ipsu signals.

As there were uncertainties regarding the dynamic response of the system to a varying input an initial set of frequencies were chosen to test its response.

A frequency response set of tests were designed to attain the data required for performance testing the system under a dynamic input and, thus modelling the

system's dynamic response. At least, initially guiding the methodology of the next steps to take for the modelling.

Ideally, the target frequency would emulate equivalent real-time fluctuations observed in solar irradiance. From literature and accessible solar irradiance data archives this would range from 1 - 10^5 Hz i.e. one second to one day. At this stage, taking into account observable fluctuations due to cloud coverage, a periodic range between 0.5 seconds - 1 minute (approximately) was deemed to be adequate, at least until analysis of test data could give a more precise value for frequency.

An excitation signal was applied to the system, in this case a simple sine wave. The system's outputs were observed and the responding data was captured.

The power supply unit, PSU, used to supply power to the solar pump controller, has a trackable 0 - 10V input signal that it maps to a corresponding 0 - 80 V voltage output. The PSU supplies the voltage to the solar pump controller. The solar pump controller's ability to perform power regulation operations were disabled for these tests (and all future tests going forward). The signal amplitude range was designed to match the minimum and maximum pump input voltage. The voltage range for the pump was ascertained during the pump benchmark tests explained in section 4.3.3, and are within the optimal operating conditions for the pump, 50 - 70 V.

An old TENMA Jupiter 2010 wave function generator (WFG) was used to set the target signal for the power supply unit (PSU). The WFG lacked built-in memory, preventing the presetting of function parameters. To address this, a method was developed to manually replicate the wave functions each time a parameter needed adjustment. This method did not always produce precise values until the WFG was upgraded in the spring of 2022. Consequently, the term "approximately" is used frequently in this section to indicate the inherent variability in the generated values.

The amplitude of the WFG sine wave signals were either 1.25 or 2.5 V, equivalent to a 10 or 20 V amplitude range delivered to the pump. These were combined with an offset of 6.25, 6.875 and 7.5 V, which translates to a pump voltage of 55, 60 and 65 V respectively.

The signal frequency was set to fast, medium and slow; 2, 0.2, 0.02 Hz respectively, equivalent to 0.5, 5 and 50 seconds, approximately.

The full amplitude, 2.5 V, with an offset of 6.875 V was used as the standard system input signal as this would test the pump over the entire 20 V range, 50 - 70 V.

Once the amplitude and frequency parameters were chosen, there were a total of 12 individual sine signals used to test the frequency response of the system, see table 5.1. These 12 sinewaves will be referred to as a suite of data or data suite going forward.

The old TENMA Jupiter 2010 WFG was replaced by a digital FEELTECH dual channel function arbitrary waveform generator and the 12 sines were recorded as presets 01 -12 on the new device. This lead to increased accuracy and repeatability of the wave function parameters as displayed 5.1.

This was to test the system over a range of frequency and amplitude signals. The additional presets were 50V-60 V, 55-65 V and 60-70 V equivalent. Again these three amplitude settings were paired with the 3 frequency settings to produce an additional 9 presets. Going forward in this paper the, in total, 12 presets will be referred to as a full suite of data. When operating the system with different input parameter settings and system configuration a full suite of data tests would be attempted.

Table 5.1: The standard data suite used to evaluate the system under different parameters, comprised of 12 separate data sets

Data Set	**Amplitude**	**Frequency**	**Voltage Range**
01	10 V	2 Hz	50 - 60 V
02	10 V	0.2 Hz	50 - 60 V
03	10 V	0.02 Hz	50 - 60 V
04	10 V	2 Hz	55 - 65 V
05	10 V	0.2 Hz	55 - 65 V
06	10 V	0.02 Hz	55 - 65 V
07	10 V	2 Hz	60 - 70 V
08	10 V	0.2 Hz	60 - 70 V
09	10 V	0.02 Hz	60 - 70 V
10	20 V	2 Hz	50 - 70 V
11	20 V	0.2 Hz	50 - 70 V
12	20 V	0.02 Hz	50 - 70 V

5.7 Results

Figure 5.7.1 illustrate the descriptive and predictive fit for models fitted to SI data at three different salinities; freshwater (350 ppm), brackish (1250 ppm), brackish (2000 ppm).

5.7.1 Resistance Function: non-parametric

Figure 5.7.2 depicts the inferred non-parametric resistance as a function of excitation frequency. Each data point corresponds to a regression of observed time series for flow rate against pressure. The plots also indicate standard errors regression coefficients.

Both R_1 and R_g appear to be overall decreasing as a function of increasing frequency. This relation appears to broadly corroborate the parametric estimation for R_g, as can be seen in Figure 5.7.4, indicating that it may be

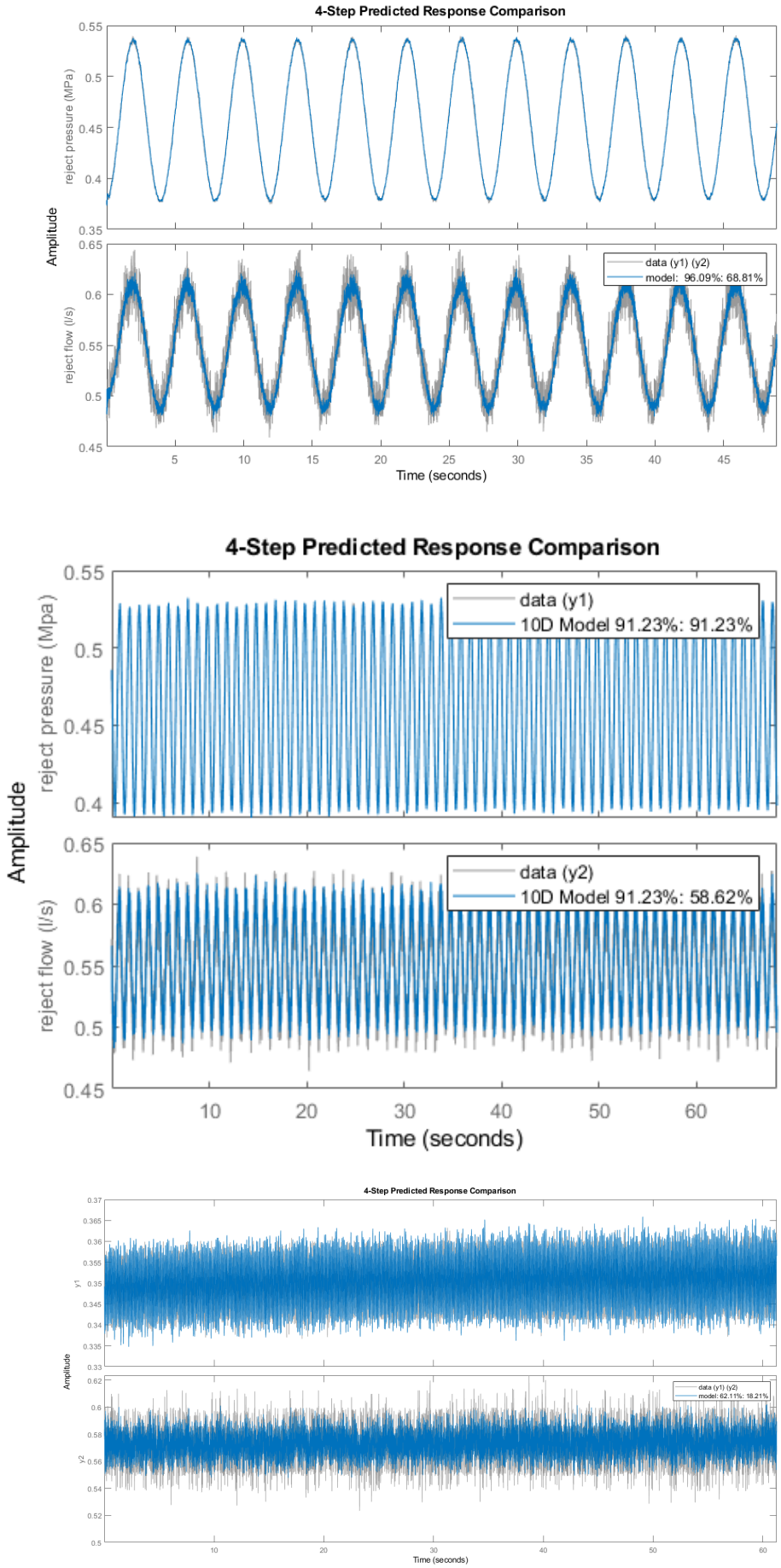

Figure 5.7.1: Black box model fits

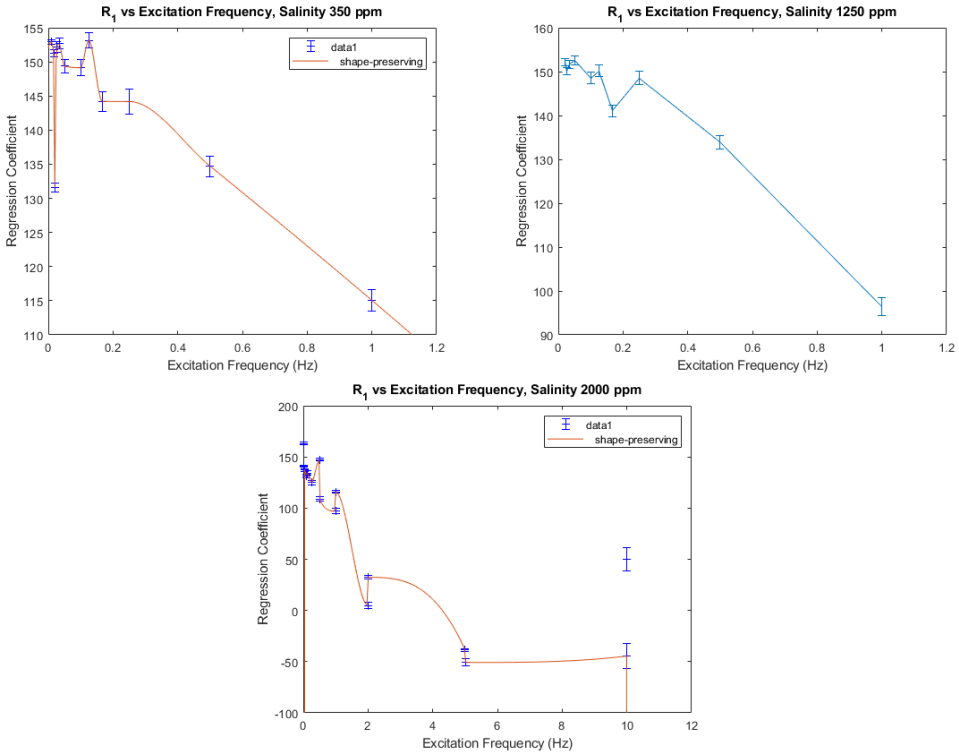

Figure 5.7.2: Non-parametric estimation for resistance R_1

possible to increase desalination efficiency through modulation of the input signal.

5.8 Discussion

The overarching concept of using the hydraulic analogy in reverse to assess a PVRO system by its electronic component counterparts is introduced. Ohm's law, $V = IR$, is equivalent to $P = QR$, where R represents the equivalent resistance to water flow, similar to how RR represents resistance to the flow of electrons (current). Moreover, if Ohm's law holds true, then other circuit analysis techniques like Kirchhoff's law are also applicable. Kirchhoff's law states that the total flow out of a node is the summation of flows into and out of that node. Expressing electronic circuits as hydraulic analogies is known as the hydraulic analogy. The term "circuit equivalence" has been coined to infer the reverse process: taking a hydraulic system and converting it into its electronic circuit

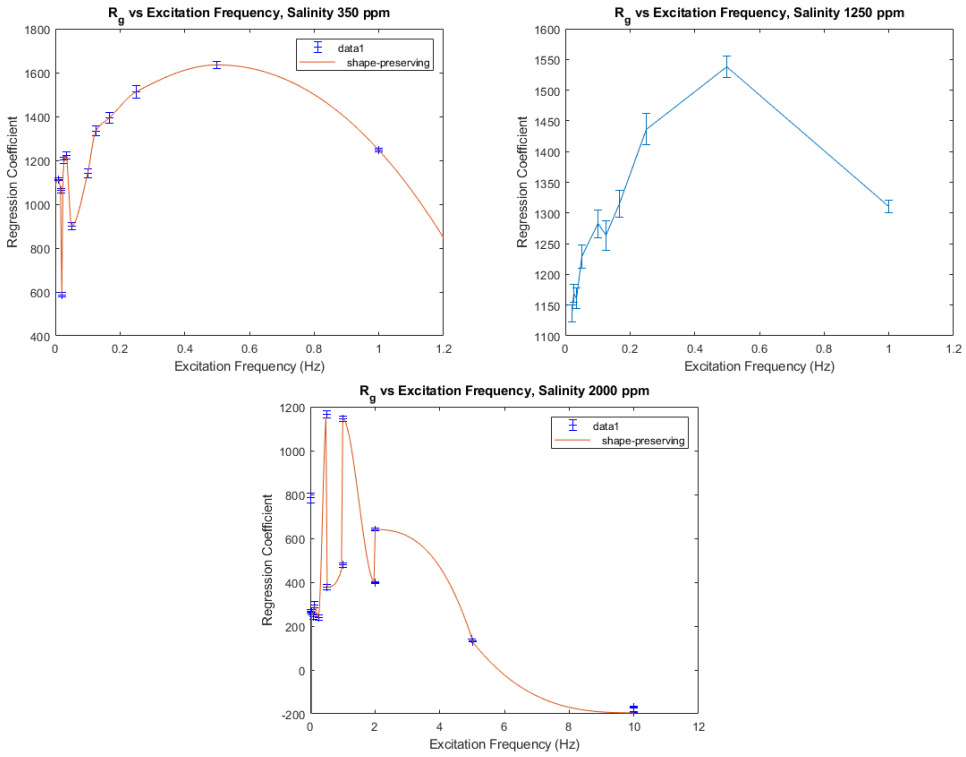

Figure 5.7.3: Non-parametric estimation for resistance R_g

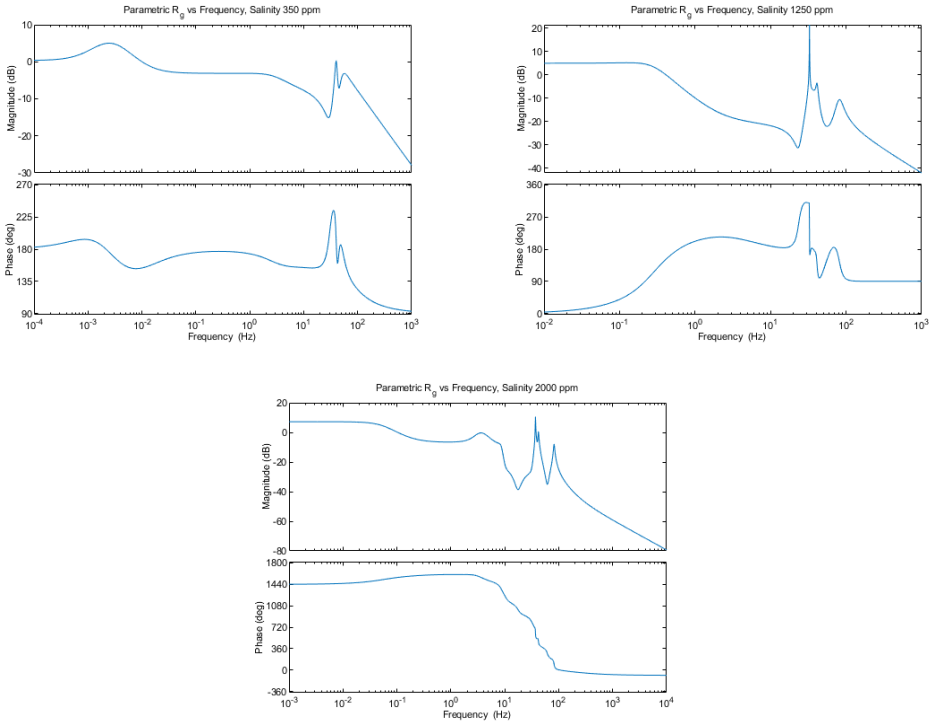

Figure 5.7.4: Parametric estimation for resistance R_g

component equivalent.

This concept was first applied to a simplified version of the system, focusing on the most basic form of IRES, which includes just the PVRO components. Input signals in the form of sinewaves were applied to the PVRO component, allowing for LT and FFT analysis of the input/output signals.

From system insights, three candidate models were proposed: a black box model comprising of two inputs and two outputs, a parametric model based on the circuit equivalence technique, and a hybrid model, or grey box model. Multi-model analysis was explored via system identification analysis by applying parametric and non-parametric fits, first-principle, and blackbox modelling techniques to establish the most confident model framework for the system.

A range of excitation input frequencies were used to determine the RO membrane resistance response to modulation. Both parametric and non-parametric models demonstrated that there is a frequency 'sweet spot' where a drop in membrane resistance was observed. This would equate to a higher product flow rate for less energy input, resulting in a reduction in the specific energy of consumption of desalination.

6

The Energy Recovery Prototype

REDACTED

This chapter has been omitted due to containing commercially sensitive information.

7

Modelling System Dynamics: the circuit equivalence model

7.1 Introduction

This chapter investigates the duality of electric circuits and hydraulic systems by defining a full system model based on first principles i.e. a white box model.

The electric-hydraulic analogy uses hydraulic systems to express the dynamics of electric circuits. A pressure differential due to gravity between bodies of water separated by distance in height or mechanical motion (i.e. pumped systems), is analogous to the voltage potential present in an electronic circuit. The flow of fluid is analogous current. Likewise, resistance, capacitance and inductance can be represented by a constricted section of pipe, a non-permeable elastic membrane across a pipe and a heavy water wheel with its paddles submerged in the fluid flow, respectively.

The analogy doesn't hold for all cases. Eddy currents, electro-magnetic fields and the Peltier effect are all instances that cannot be inferred by hydraulic systems and their counterpart components [71]. Furthermore, not all representations are backward compatible [75]. For example, how does one express pump cavitation or water-hammer with an electric circuit?

The more the analogy is scrutinised the better understanding the user needs of

both electric circuits and hydraulic systems. Leaky pipes can be expressed as power losses. A diode can be represented by a check valve with a leaky seal to represent losses. The back-and-forth movement of a piston can be expressed by a capacitor undergoing alternating current. The stiction of the piston and leakage over the piston head can be represented by the parasitic properties of the equivalent series inductance (ESL) and equivalent series resistance (ESR) exhibited in the performance reduction of the capacitor [74]. In wanting to capture the minutiae dynamics, the greater the imagination is needed to express them analogously. To the point the abstraction defeats the purpose of the exercise.

That being said, as long as the user remains vigilant of the analogy's limitations and does not overreach its intended goal, then the electric-hydraulic analogy can be a powerful tool to derive solutions for dynamic systems where the computing cost would be too great by alternative means.

The electric-hydraulic analogy is nothing new. The theory was established in the 1800s [73] and gained popularity as a teaching method for the first half of the 20th century[72]. Nikola Tesla designed the Valvular Conduit, a flow control device that has the characteristics of an electric diode and can be modelled using Ohm's law [69].

The analogy's paradigms have been investigated [67], its contradictions scrutinised and its failings criticised, mainly by physicists [71]. Yet the electric-hydraulic analogy has been used to model the cardiorespiratory system [66], pressure-driven microfluidic networks [68] , and evaluate the porous media characteristics of the Alberta oil sands [70] (the second largest proven oil reserves in the world) [65], to name but a few applications.

The electric-hydraulic analogy is being used in this thesis to express a hydraulic system as an electronic circuit, the representation will be refereed to furthermore as a circuit-equivalence model.

The full (lab-based test rig) system, including pump, RO and Clark was redefined as an electric circuit with equivalent electronic component counterparts. Using simple circuit theory, namely Ohm's Law and Kirchoff's Laws for solving electronic circuits, a mathematical circuit-equivalence (CE) model was derived. Thus far the overall method for (CE) modelling has been explained. The next section discusses the specific process of modelling the system in greater detail.

7.2 Electronic Phenomena & Their Analogous Counterparts

An inductor is analogous to a heavy water wheel with a high value of inertia. The waterwheel inhibits the flow until the speed of rotation matches the flow velocity. Likewise, if flow velocity drops to zero the water wheel would continue to rotate. Mimicking the dynamics of an inductor. If two waterwheels were joined axially yet their paddles were submerged in separated flows, then the waterwheels would impart energy upon each other in such a way that the difference in the velocity of flows would be dampened. Thus, the flows although physically separated still interact with each other through a transfer of energy. This behaviour is analogous to a pair of coupled inductors.

A capacitor stores voltage energy in the form of electrons across an electrolytic plate. In this way capacitors maintain circuit voltage by charging and discharging when the capacitor voltage is less or greater than the line voltage. This is analogous to to pressure storage vessel, also known as a pressure accumulator, as described in Chapter 4.2.3.

As previously noted in Chapter 4.2.4, Pascals are readily convertible to Joules per meter cubed. Thus, it follows when dividing pressure by volumetric flow rate in m^3/s the resulting SI units are J/s, which is also the definition of Watts. Therefore, in keeping with the circuit analogy the pressure divided by the flow is

equivalent to the power in Watts dissipated by a resistive load.

7.3 Deriving the Circuit Equivalence Model

The circuit equivalence method for modelling the dynamics of the IRES is based on a simple DC circuit. The following theory and equations were communicated by personal communication from Noel McWilliam, 2017. The CE model pairs devices and paraphernalia used in pumping water systems with their equivalent electronic counterpart. Water flow though a pumped system is analogous with DC current travelling through an electronic circuit. Water pressure within a pumped system is equivalent to the voltage potential being supplied to the circuit.

Likewise restrictions in the piping and components induce a resistance to flow, and accordingly, a pressure drop across components would be observed.

With these three analogous variables it is possible to construct Ohms Law V=IR.

Where the components are in parallel the total flow will pass through them. When in series the flow will split proportionally determined by the sum of the individual resistances of the components in each branch of the system. This is analogous to the conservation of charge principle as stated by Kirchoff's Current Law, KCL.

The conservation of energy principle, as defined by Kirchoff's Voltage Law, where the sum of voltages around a closed loop is zero, can be justified as the system is a closed loop. All flow entering the system (from the submerged pump) at pressure returns to the same tank at negligible pressure.

Kirchoff's Laws in conjunction with Ohm's Law can evaluate the values of current (I), voltage (V) and resistance (R) for the system and all its components.

7.3.1 Insights & Assumptions

Assuming Kirchhoff's Law holds then the full system can be modelled as follows.

In the case of a pumped reverse osmosis system the submersible pumps acts as an ideal DC source i.e. a perfect battery.

The reverse osmosis unit can be modelled as two resistors in parallel, with one of the resistors attached to GND, this would reflect the path the product flow takes as the permeate exits to atmospheric pressure with no back pressure applied i.e. equivalent to ground. The output of second resistor is fed to the Clark, analogous to the path the RO reject takes.

The Clark is the hardest to model as it is a symmetrical device yet each side acts as the inverse action of the other. One side drives the pressurisation of the fluid on the other side and upon the returning stroke of the piston the side that was pressurised now becomes the driving force pressurising the other side. As one side fills the other side empties.

The feed flow from the pump enters the Clark, and has its (pressure) energy amplified before it reaches the RO. Similarly, the RO reject returns to the Clark imparting its (pressure) energy before returning to the tank. To simplify and summarise The Clark stage, nestled between the pump stage and the RO stage, captures the flow, performs an energy transfer function upon the flow, and releases the flow.

The desire to explicitly capture the out of phase yet reciprocal energy transfer stages of the Clark mechanism necessitates representing the Clark as its own sub-circuit, embedded within the system, as a configuration of equivalent electrical storage devices. The solution, like the Clark itself, although hard to describe with words is elegant in its simplicity.

All flows are separated from mixing by the piston heads, i.e. they should not be physically represented as connected by nodes or junctions in the CE model.

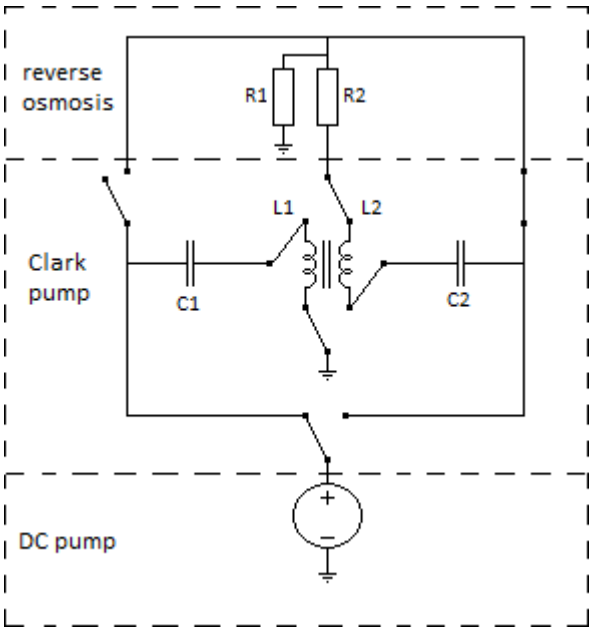

Figure 7.3.1: The lab based PVRO system with Clark redrawn as an electronic circuit

Energy transfer takes place by imparting force in the same direction on both piston heads joined by the piston rod.

To summarise, flow from the pump interacts with the piston head, which inhibits flow across the Clark yet transfers energy to the opposite chamber via the piston rod. Thus the piston head is analogous to a capacitor while the piston rod is analogous to an inductor. As the Clark is a symmetrical device it is in keeping that the chambers are a reflection of each other. Therefore this symmetry is captured in the CE model by having a pair of coupled inductors, analogous to the piston rod, paired with a capacitor on either side, analogous to the piston head.

Figure 7.3.1 depicts the full system as an electronic circuit. For simplicity the internal switching of the Clark has been modelled as synchronised open/closed switches.

7.3.2 Uncoupled Discharge Dynamics

The feed-voltage to the resistance sub-circuit is also the voltage across the right-hand capacitor $vRC(t)$ at time t. $iR2(t)$ is the current from the outer plate of the right-hand capacitor to the feed of the RO sub-circuit and $iR3(t)$ the current flowing through $R1$ into the top of the right=hand inductor. The voltage drop across $R1$ is $iR3(t)R1$. The current flowing through $R1$ is the current for the right inductor. Therefore, $vRI(t)$ is the voltage across the right-hand inductor at time t.

The charging and discharging circuits are electrically isolated, except for their coupling via the two central inductors.

$$v_C^R(t) + i_3^R(t)R_1 + v_I^R(t) = 0 \tag{7.3.1}$$

Current flowing through an inductor produces an EMF in the inductor that inhibits the flow of current. The back EMF allows current flow through the inductor when it is proportional to the current. Therefore, field strength is proportional to the acceleration of charge through the coil, or equivalently the speed of change of the current.

The uncoupled voltage across the right-hand inductor can be defined as

$$v_I^R(t) = L_R \frac{di_3}{dt} \tag{7.3.2}$$

where L_R is the inductance in Henries.

The two variables $V_R^C(t)$ and $i_R^3(t)$ have been defined. The voltage across a capacitor is directly proportional to the sum of the current applied to it, thus $i_R^3(t)$ is a function of $V_R^C(t)$.

Due to the energy storage properties of the capacitors and inductors, and the way

the circuit is configured, the current in and out of the capacitors are not equal, i.e. $i_0 \neq i_1$ and $i_2 \neq i_3$.

Expressing the above in differential form

$$C_R \frac{dv_C^R}{dt} = \frac{i_3^R + i_2^R}{2} \tag{7.3.3}$$

$C_R > 0$ is the capacitance in Farads of the right-hand capacitor. R_1 and R_G are configured in parallel therefore the current is split in proportion to the ratio of the resistances. The sum of the resistances are $i_3^R = \frac{R_1}{R_1+R_G} i_2^R$.

Substituting into 7.3.3

$$k i_3^R = C_R \frac{dv_C^R}{dt} \tag{7.3.4}$$

Where $k = 1 + fracR_G 2R_1$.

Re-expressing (2) with respect to v_R^C. Differentiating (4) with respect to t and noting that both R_1 and R_G are functions of V_C^R the following expression can be ascertained (via the product rule)

$$\begin{aligned} \frac{d(k i_3^R)}{dt} &= \frac{dk}{dt} i_3^R + k \frac{di_3^R}{dt} = \frac{dk}{dv_C^R} \dot{v}_C^R i_3^R + k \frac{di_3^R}{dt} \\ &= C_R \ddot{v}_C^R \end{aligned}$$

Rearranging and substituting yields

$$\begin{aligned} \frac{di_3^R}{dt} &= \frac{1}{k}\left[C_R \ddot{v}_C^R - \frac{dk}{dv_C^R} \dot{v}_C^R i_3^R \right] \\ &= \frac{1}{k}\left[C_R \ddot{v}_C^R - \frac{C_R}{k} \frac{dk}{dv_C^R} \left(\dot{v}_C^R\right)^2 \right] \end{aligned} \tag{7.3.5}$$

Thus, equation 7.3.1 may be rewritten as

$$v_C^R(t) + \frac{R_1 C_R}{k}\dot{v}_C^R + \frac{L_R}{k}\left[C_R\ddot{v}_C^R - \frac{C_R}{k}\frac{dk}{dv_C^R}\left(\dot{v}_C^R\right)^2\right] = \frac{L_R C_R}{k}\ddot{v}_C^R + \left(\frac{R_1 C_R}{k} - \frac{L_R C_R}{k^2}\frac{dk}{dv_C^R}\dot{v}_C^R\right)\dot{v}_C^R + v_C^R = 0 \quad (7.3.6)$$

Here R_1, k and subsequently $\frac{dk}{dv_R^C}$ are extraneously derived functions of $v_R^C(t)$.

The above is an example of a non-linear, non-homogeneous ordinary differential equation. For fixed resistances this equation reduces to a linear second order homogeneous ODE.

7.3.3 Coupling & Constraints

As discussed previously the Clark pump transfers energy contained within the reject flow amplifying the pressure of the feed flow. There must be sufficient force foe this to take place. By construction, the reject flow rates are less than that of the input since some feed flow passes through the membrane as product.

Furthermore, the pressure of the reject will always be less than that at the membrane inlet due to internal resistance within the membrane. To overcome these losses the Clark pump joins the left and right hand chambers via a single actuating shaft, thus the incoming low pressure feed augments the energy recovered from the reject stream. These two combined forces increase the pressure of the low pressure beyond that of the reject stream and ensure the pressure ramps up to a pressure that delivers the recovery ratio $\frac{As}{Ap}$.

7.3.4 Energy Losses are Negligible

To characterise the non-stationary dynamics it is assumed that energy losses are negligible. The additive force applied to the high-pressure feed is supplied by the low-pressure feed $i_0(t)$ and the reject $i_3(t)$. In line with the circuit analogy, the coupling between the left hand and right hand chambers via the piston rod is represented by a pair of couples inductors. Wherein, the EMF within one coil can induce an acceleration of current in the other.

Within the discharging sub-circuit the coupled inductors provide an additional force, in addition to the force provided in equation 7.3.2.

Therefore, equation 7.3.6 is re-expressed with this additional term.

$$\frac{L_R C_R}{k}\ddot{v}_C^R + \frac{C_R}{k}\left(R_1 - \frac{L_R}{k}\frac{dk}{dv_C^R}\dot{v}_C^R\right)\dot{v}_C^R + v_C^R - L_R^C\frac{di_0^L}{dt} = 0 \tag{7.3.7}$$

L_R^C is the coupling coefficient of the left-hand inductor.

7.3.5 Coupled Charge Dynamics

The circuit is driven by an ideal DC source i.e. a perfect battery.

Considering the left side components; current $i_0^L(t)$ flows from the battery to the capacitor, and a second current $i_1^L(t)$ from the inner plate of the capacitor to the top of the left-hand inductor.

Applying Kirchhoff's Law to the left-side components derives

$$v_{DC}(t) - v_C^L(t) - v_I^L(t) = 0 \tag{7.3.8}$$

The source voltage $vDC(t) > 0$ is an extraneously given possibly time-varying quantity.

For the coupled circuit

$$v_I^L(t) = L_L \frac{di_0^L}{dt} + L_L^C \frac{di_3^R}{dt} \tag{7.3.9}$$

Substituting from equation **??** into the above and rearranging into 7.3.8

$$\frac{di_0^L}{dt} = \frac{1}{L_L}\left[v_{DC}(t) - v_C^L(t) - \frac{L_L^C}{k}\left[C_R \ddot{v}_C^R - \frac{C_R}{k}\frac{dk}{dv_C^R}\left(\dot{v}_C^R\right)^2\right]\right] \tag{7.3.10}$$

Here the impact of the "control variable" v_{DC} on v_C^R is expressed.

To fully characterise solutions to the system dynamics $v_C^L(t)$ must be defined. Consequently, additional assumptions need to be made..

7.3.6 Fluids are Ideal

It is not clear if further assumptions are needed at this point. For example, does partial filling take place? i.e. upon start up is some portion of the system occupied by a compressible fluid such as air. Is the membrane rigid or plastic? Further analysis is necessary to fully characterise the system dynamics, but, as a starting point, the following assumption is made.

7.3.7 Partial Filling of the Inner Chamber

There exists some constant $K^j > 0$ such that

$$i_1(t) = \rho K^j i_0(t)$$

$\rho = \frac{1-As}{Ap}$ and $j = 1, ..., n$ denote the j^th charge-discharge cycle.

For $K^j \in (0, 1)$ a situation arises such that the the inner chamber fills less than

would be expected from the equilibrium recovery ratio $\frac{As}{Ap}$. Potentially, this would happen if either: the current recovery ratio was higher than expected; or the input flow is increasing in time. The latter could be due to membrane plasticity or compressible fluids within the system creating a time lag between the feed flow and permeate/reject flows.

It is assumed later that the membrane is plastic together with an additional term expressing membrane fluid retention time. Consequent to this assumption and in alignment with the circuit analogy;

$$C_L \frac{dv_C^L}{dt} = \frac{i_0^L + i_1^L}{2} = i_0^L \frac{\rho K^j + 1}{2}$$

thus from 7.3.9 and 7.3.5 equation 7.3.8 may be rewritten as

$$\begin{aligned} 0 = v_{DC}(t) - v_C^L(t) - \frac{2L_L C_L}{\rho K^j + 1}\ddot{v}_C^L \\ - \frac{L_L^C}{k}\left[C_R \ddot{v}_C^R - \frac{C_R}{k}\frac{dk}{dv_C^R}(\dot{v}_C^R)^2\right] \end{aligned} \tag{7.3.11}$$

Together with equation 7.3.7 defining a coupled system of two non-linear non-homogeneous differential equations in two unknowns v_C^L and v_C^R.

Substituting 7.3.10 into 7.3.7

$$\begin{aligned} \frac{L_R C_R}{k}\ddot{v}_C^R + \frac{C_R}{k}\left(R_1 - \frac{L_R}{k}\frac{dk}{dv_C^R}\dot{v}_C^R\right)\dot{v}_C^R + v_C^R \\ - L_R^C\left(\frac{1}{L_L}\left[v_D^C - v_C^L - \frac{L_L^C}{k}\left[C_R\ddot{v}_C^R - \frac{C_R}{k}\frac{dk}{dv_C^R}(\dot{v}_C^R)^2\right]\right]\right) = 0 \end{aligned} \tag{7.3.12}$$

to make equation 7.3.12

Setting initial conditions such that

$$t = t_0 \qquad v_c^R = v_C^L = 0 \qquad \dot{v}_C^R = \dot{v}_C^L = 0$$

$$\frac{L_R C_R}{k}\ddot{v}_C^R \quad - \quad L_R^C\left(\frac{1}{L_L}\left[v_D^C \quad - \quad \frac{L_L^C}{k}\left[C_R\ddot{v}_C^R\right]\right]\right) \quad = \quad 0$$

$$\frac{L_R C_R}{k}\ddot{v}_C^R \quad - \quad L_R^C\left(\frac{1}{L_L}\left[v_D^C \quad - \quad \frac{L_L^C C_R\ddot{v}_C^R}{k}\right]\right) \quad = \quad 0$$

$$\frac{L_R C_R}{k}\ddot{v}_C^R \quad - \quad \frac{L_R^C v_D^C}{L_L} \quad - \quad \frac{L_R^C L_L^C C_R}{L_L k}\ddot{v}_C^R \quad = \quad 0 \quad (7.3.13)$$

Solving for $\ddot{v}_C^R$

$$a\ddot{v}_C^R - b - c\ddot{v}_C^R = 0$$
$$a\ddot{v}_C^R - c\ddot{v}_C^R = b$$
$$\ddot{v}_C^R\left[a - c\right] = b$$
$$\ddot{v}_C^R = \frac{b}{a - c}$$

$$a = \frac{L_R C_R}{k} \qquad b = \frac{L_R^C v_D^C}{L_L} \qquad c = \frac{L_R^C L_L^C C_R}{L_L k} \frac{L_R^C v_D^C}{L_L}$$

and rearranging for 7.3.13

$$\ddot{v}_C^R = \frac{\left[\frac{L_R^C v_D^C}{L_L}\right]}{\frac{L_R C_R}{k} - \frac{L_R^C L_L^C C_R}{L_L k}}$$

$$\ddot{v}_C^R = \frac{\left[\frac{L_R^C v_D^C}{L_L}\right]}{\frac{C_R}{k}\left[L_R - \frac{L_R^C L_L^C}{L_L}\right]} \tag{7.3.14}$$

Equation 7.3.12 can be rearranged for V_C^R to establish state space $x1$

$$v_C^R = L_R^C\Big(\frac{1}{L_L}\Big[v_D^C - v_C^L - \frac{L_L^C}{k}\big[C_R\ddot{v}_C^R - \frac{C_R}{k}\frac{dk}{dv_C^R}(\dot{v}_C^R)^2\big]\Big]\Big) - \frac{L_R C_R}{k}\ddot{v}_C^R - \frac{C_R}{k}\Big[R - 1 - \frac{L_R}{k}\frac{dk}{dv_C^R}\Big]\dot{v}_C^R \tag{7.3.15}$$

7.4 Model Parameteriastion

This section introduces the experiments conducted that parametrise components of the model pertaining to the Clark pump. Specifically, this section will consider experiments devised to isolate sub-components of the Clark to facilitate the parametrisation of variables that would otherwise not be observable. In this regard the Clark is disassembled into the following particular configurations:

- 'Rectifier Bridge';

- 'Spring Configuration', forward and reverse piston head;
- 'Pistonless Configuration'.

The Rectifier Bridge configuration isolates the passive valve mechanism through which low pressure feed and high pressure RO feed flow. This configuration, as discussed in Section 7.4.1, bypasses flow to and from the inner and outer chambers. Allowing evaluation of resistances to flow into and out of the chamber.

The Spring Configuration discussed in Section 7.5 bypasses to the inner chamber, thereby isolating within the outer chamber permitting parameterisation of chamber resistances and capacitance.

Section 7.6 outlines a Pistonless Configuration. Whereby the piston head is removed allowing direct feed of flow through the Clark piston cylinder and through the top section exiting via the Clark reject port. In this way Clark reject resistances may be isolated.

The following subsections detail these three configurations.

7.4.1 Rectifier Bridge Resistances

The bottom section of the Clark is analogous to the configuration of a "reverse" rectifier bridge: rather than an AC source driving a DC load, the load is AC and the source is DC. Similar to a DC battery driving the AC motor of an electric vehicle.

To isolate the resistance the feed flow encounters upon entering the rectifier bridge section of the Clark, the j-tubes connecting the bottom section to the outer chambers were removed and the j-tube ports were plugged.

Figure 7.4.1 depicts this configuration wherein feed flow Q_f enters the bottom section of the Clark, with the flow split between the two channels of the rectifier bridge, and rejoining before exiting the Clark. No flow enters the outer chambers

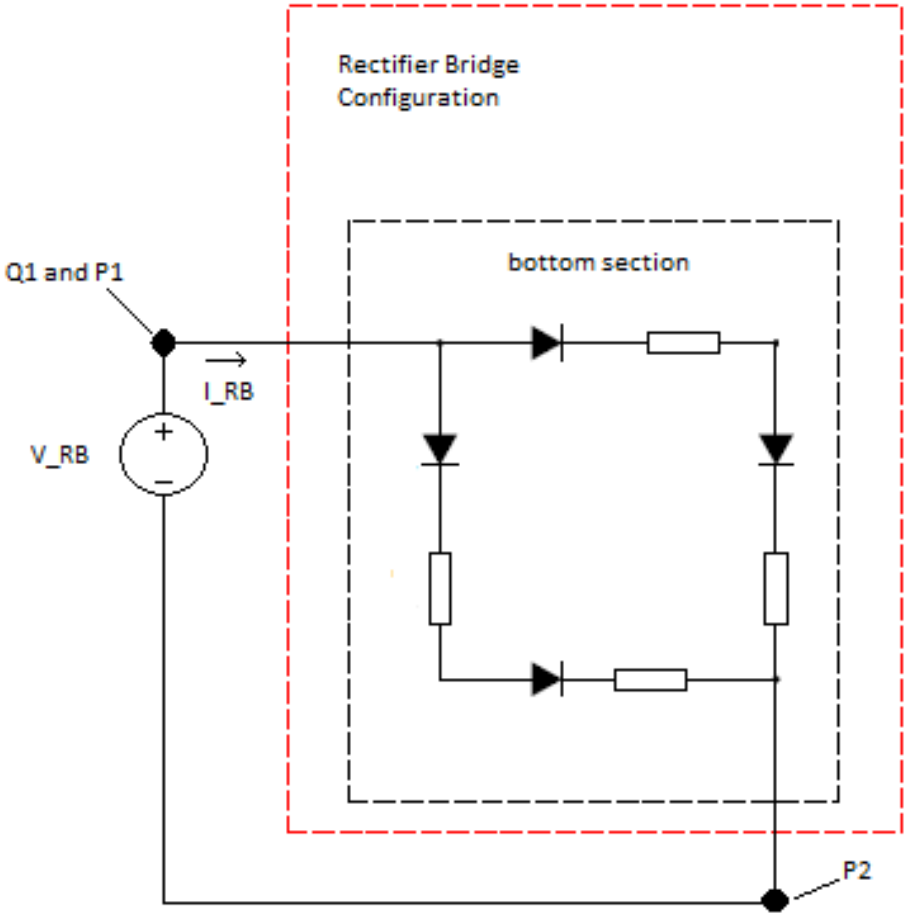

Figure 7.4.1: 'rectifier bridge'circuit model withsensor placement

of the Clark.

In keeping with the general circuit analogy the flow rates and pressures the following equivalent electric counterparts:

$$I_{RB} = Q_1 \qquad\qquad V_{RB} = P_1 - P_2$$

By symmetry of the bridge internal topology it can be assumed that the four component resistances have equivalent value. Consequently, the experiments aim to evaluate the following resistance:

$$R_{RB} = \frac{V_{RB}}{I_{RB}} \tag{7.4.1}$$

where it is admitted $R_{RB}(s)$ may be a function of frequency s.

7.4.2 General Methdology

Pump voltages and input frequencies were modulated as described in Section **??**

Resistances at equilibrium and dynamic voltage ranges were assessed by regressing $v_{RB}(t)$ against $i_{RB}(+\delta)$ where δ denotes a fixed lag to be determined and the use of lowercase indicates observed values in the time domain.

7.4.3 Results

Figures 7.4.3 (a-d) are illustrative of the regression fits deriving estimates for R_{RB}. As can be seen a linear fit is a good descriptor of the relation between pressure differential and flow rate, with R^2 values typically greater than 0.95. However, it should be noted that the observed intercept values appear non-trivial, in contradistinction to Ohm's Law.

Interestingly, the estimated resistances appear to be a strong function of frequency and a weaker function of voltage range, as can be seen in Figure 7.4.2. Errorbars show standard errors for the regression coefficient of each time series pair, indicating that these apparent relations are statistically significant.

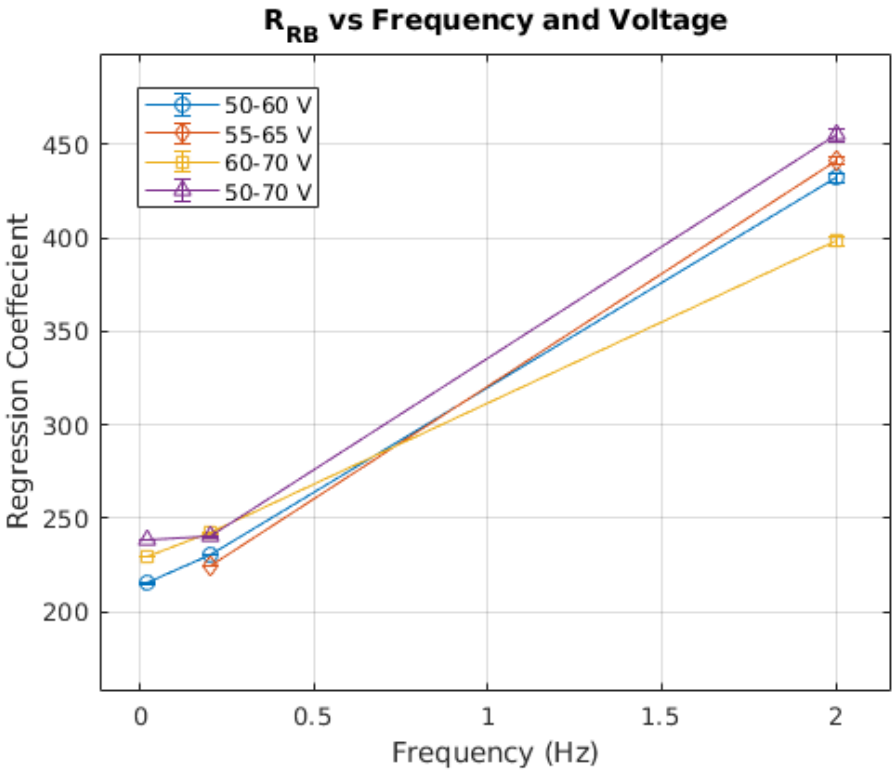

Figure 7.4.2: 'rectifier bridge' dynamic regression coefficients

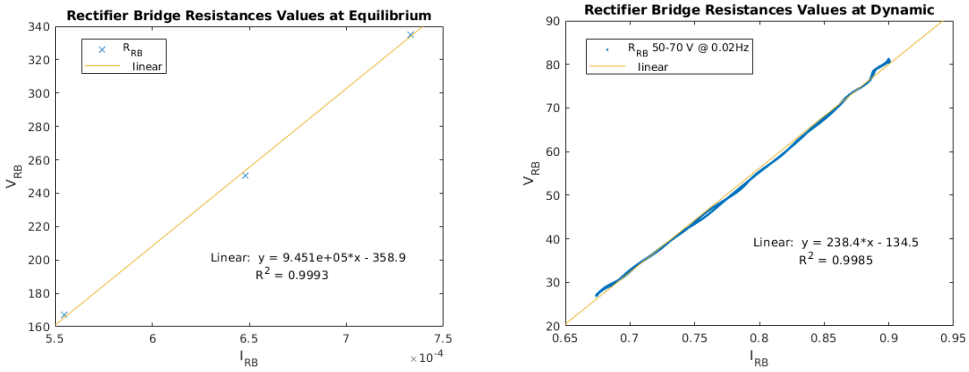

Figure 7.4.3: 'rectifier bridge' power dissipation in Watts

7.5 Spring Configuration

As noted previously the Clark is modelled as an RCL circuit whereby actuation of the piston head acts as a mean to store fluid flow, analogous to a capacitor storing charge. In this approach the piston rod transmits force from one chamber of the Clark to the other, and as such emulates the transmission of force between two coupled inductors without the direct transference of electrical current. As a means to isolate the parametrisation of Clark capacitance and component resistances subsequent to the Rectifier Bridge, the Clark was configured as shown in Figure 7.5.2.

In this set-up the right-hand chamber of the Clark was reconfigured to internally house a spring between the piston head and the j-tube port, see Figure 7.5.1. In this way the spring provides a reactive force to incoming flow to the left-hand chamber permitting dynamic testing and providing the following key advantages: analytical simplicity — this set-up obviates the need to observe and model pressure dynamics within the inner chamber; explicit measurement of leakage over the piston head, which would otherwise be incorporated into the Clark reject flow; implicit measurement of pressures at the piston head by inference from observed spring compression and known spring k-values.

With reference to Figure 7.5.2 let $Q_1(t)$ denote the feed flow from the submersible pump entering into the inlet port of the Clark. As described in Section 7.4.1 the feed flow splits across the rectifier bridge with flow $I_1(t)$ entering the outer chamber of the left-hand side of the Clark. The remaining portion $I_2(t)$ flows through the opposing side of the rectifier bridge exiting the Clark via the outlet port, and through a separate gate valve. The gate valve permits control of back pressure to ensure sufficient compression of the spring.

Flow $I_1(t)$ travels through the left-hand j-tube and outer chamber during actuation of the piston in the forward direction, leading to compression of the spring within the right-hand chamber. Some flow I_{oi} passes over the piston

Figure 7.5.1: 'Spring Configuration' Clark assembly

head and exits the Clark through the middle section as leakage $I_l(t)$.

Should the compressive force within the spring exceed the opposing force on the piston head fluid will flow out from the left-hand outer chamber into the lower right channel of the rectifier bridge and exit through the Clark outlet port.

In normal operation the inner chambers of the Clark would receive high pressure fluid flow from the RO reject leading to possible leakage I_{io} from the inner to the outer chamber.

The Spring Configuration parametrises the resistance R_1 to the flow I_1, the forward leakage resistance R_{oi} and the chamber capacitance C.

As noted in Section 7.3 the change in pressure across the Clark is assumed proportional to the total net-flow, that is to say

$$V_C = C \int_0^t \big(i_1(s) - i_l(s)\big).$$

A water molecule passing into the chamber and exiting over the piston head as leakage will experience a pressure differential equivalent to a difference in pressure at the piston head and atmospheric. In contrast a water molecule passing into the chamber which is deflected by the piston head and ejected via the outlet port will experience a pressure diferential equivalent to the difference between the piston head pressure and the pressure at transducer two P_2.

Again in relation to the circuit equivalence analogy via application of Kirchoff's Law the following relations are stated:

$$\Delta v^L(t) \quad = \quad i_1(t)R_1 \quad + \quad i_l(t)R_{oi} \quad + \quad C\int_0^t \big(i_1(s) \quad - \quad i_l(s)\big)ds, \quad (7.5.1)$$

and

$$\Delta v^S(t) \quad = \quad i_1(t)R_1 \quad + \quad i_2(t)R_2 \quad + \quad C\int_0^t \big(i_1(s) \quad - \quad i_2(s)\big)ds, \quad (7.5.2)$$

where $i_1(t)R_1$ and $i_l(t)R_{io}$ represent the pressure drop respectively due to resistances, expansion losses and turbulence within the j-tube and outer chamber; and leakage pressure loss.

To intuit $v^s(t)$ suppose that the Clark pump were entirely lossless. Furthermore, suppose $P_1 = P_2$, that is to say the transducers – situated at the inlet to the left hand side of the Clark and the outlet of the Clark subsequent to the (for the sake of argument) lossless rectifier bridge – both read the same pressure. Since the transducers are connected via the piston head then for the equality $P_1 = P_2$ to hold, no pressure can be exerted at the piston head. If such a scenario were possible then no force would be applied to the spring, no displacement would occur and there would be no volumetric change nor attendant net flow into or out of the Clark. In reality the piston head has finite area and as such assuming constant at transducer one pressure applied at the piston head would reduce the subsequent pressure at transducer two. Thus, one may think of the pressure differential between transducer one and two as a factor proportional to

the volumetric displacement and the corresponding flow into/out of the Clark in the same way voltage differential relates to charge/discharge within a capacitor.

The next section defines the methodology used to evaluate whether such a scenario were possible then no force would applied to the spring, no displacement would occur and no volumetric change and attendant net flow into or out of the Clark would occur. In reality the piston head had finite area and as such the above relations.

7.5.1 Methodology

The points of interest for this model are internal to the Clark and therefore cannot be observed or measured directly during normal operation. The back and forth of the piston is equivalent to the charging/discharging of a capacitor. A proxy was needed to emulate the dynamic resonance of this behaviour. A spring was mounted inside the outer chamber on one side of the Clark, in between the piston head and the j-tube port. The j-tube was removed. The j-tube port on the outer chamber was left open, and the j-tube port on the bottom middle section of the Clark was plugged. This meant flow entering the Clark via the rectifier bridge would interact with the piston head in the outer chamber on the other side of the Clark. The returning force of the spring would encapsulate the capacitance dynamic of the outer chamber of the model, as depicted by the schematic in Figure 7.5.2.

A rod with length greater than the swept length of the outer chamber was 3D printed and attached to the piston head, with the end of the rod protruding through the open (j-tube) port. Strong neodymium magnets were attached to the end of the exposed rod.

An outer casing was designed, 3D printed and attached to the outer chamber. The casing had an open orifice which allowed the free movement of the rod when the spring was displaced. The orifice housed an optics barrel. A 3D printed disc

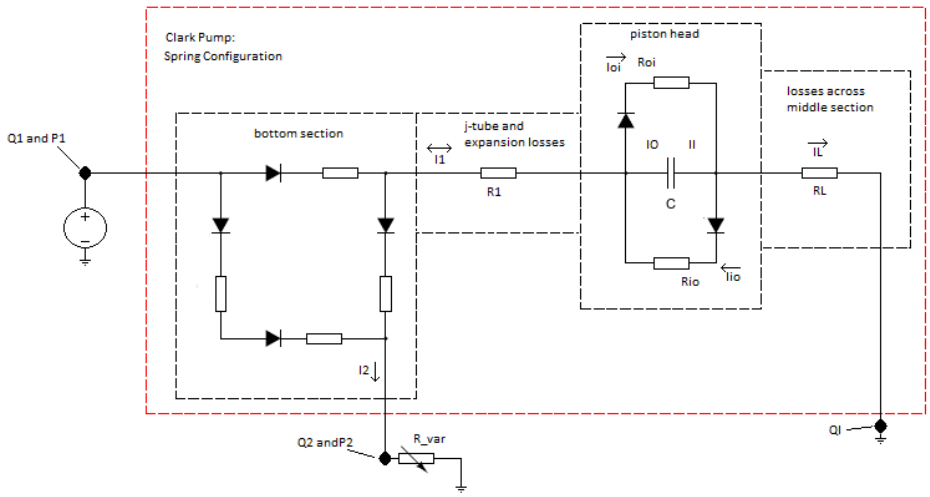

Figure 7.5.2: 'Spring Configuration' circuit model

3mm thick designed for the thread count had two Hall effect sensors embedded in it. These were used to assess displacement of the spring, one sensor being highly sensitive. A third sensor was embedded on the top of the casing above the relative position of the magnet at rest. This was to assess initial time of movement of the spring.

Initially the Clark lp reject was plugged. During the identification of the methodology process fluid was observed to leak from the open port of the outer chamber. Therefore fluid must leak past the piston head on the other side, work its way through the switching channel of the centre block to section of the Clark, drain into the other outer chamber, leak past the piston head on that side, and fill the outer chamber until it leaked out of the open port. Capturing the leakage was of importance but got in the way of the magnet/Hall effect set up.

Unplugging the Clark lp reject port gave the leakage flow an alternative exit and easier opportunity to capture it. A hose barb was attached to the Clark lp reject with a 1.6 m length of hose connected.

The leakage flow was extremely low, circa $\frac{1}{60}l/s$. Capturing and quantifying flow that low was an exercise in invention itself. Due to financial constraints there was

Figure 7.5.3: A hacked pair of scales interfaced with an Arduino to measure extremely low leakage flow.

no budget for the purchase of reliable super low flow meters. A pair of kitchen digital scales were hacked, the output fed through an op-amp and the signal amplified. The leakage was directed to a vessel placed on top of the scales. The mass of the flow was recorded and converted to litres in post processing.

1. the flow and pressure entering the 'rectifier bridge'; Q_1 and P_1 respectively
2. the flow and pressure exiting the 'rectifier bridge'; Q_2 and P_2 respectively
3. the displacement of the spring
4. the fow of leakage across the piston head

The circuit as defined in Figure 7.5 can be reduced to two states, charging and discharging, this is in line with the physical operation of the Clark during this process.

By evaluating the flows entering and exiting the outer chamber of the Clark

via the rectifier bridge and accounting for losses across the piston head the net voltages for the charge/discharge state can be defined by a CE model.

As all the components are in series the total voltage for the circuit is equal to the voltage drop across the sum of all the components. The total voltage is $V_l = V_1 + V_l + V_C$

Where $V_1 = IR_1$, $V_l = IR_l$ and $V_C = C\int_0^t \big(i_1(s) - i_l(s)\big)$

Note, R_l is a lumped parameter for the losses over the piston head in either direction which is represented by R_{oi} and R_{io} and any resistance to flow exiting the Clark as leakage. The equivalent series resistance (ESR) and equivalent series inductance (ESL) of the capacitor represent these lumped terms in the R_l term.

$$\Delta v^L(t) = i_1(t)R_j + i_l(t)R_l + C\int_0^t \big(i_1(s) - i_l(s)\big)ds \tag{7.5.3}$$

State 2: discharging subcircuit.

This circuit captures the discharging dynamic of the capacitor, equivalent to flow exiting the outer chamber of the Clark.

$$\Delta v^S(t) = i_1(t)R_j + i_2(t)R_2 + C\int_0^t \big(i_1(s) - i_2(s)\big)ds \tag{7.5.4}$$

$$I_1 = Q_1$$

$$V_1 = P_1$$

$$I_2 = Q_2$$

$$V_2 = P_2$$

$$I_l = Q_l$$

$$\Delta V_L = P_1 - P_{atm}$$

$$\Delta V_S = P_1 - P_2$$

$$I_1(s) = Q_1(cumulative)$$

$$I_2(s) = Q_2(cumulative)$$

$$I_l(s) = Q_l(cumulative)$$

7.6 Pistonless Configuration

It was desired to observe the piston head dynamics, i.e losses, from flow in the opposite direction. Without changing the current configuration another proxy was derived; flip the piston head. The piston heads are floating i.e they are not physically attached to the rod. The piston head has an asymmetric profile The side that faces the outer chamber is flanged to increase energy capture when pushing against the piston rod. Upon flipping the piston head the apparatus became non-functional and this experiment was aborted.

7.7 Discussion

To comprehensively model the entire system, an approach was employed that analogised the system to an electronic circuit, drawing upon the hydraulic analogy

for electronic circuits as a guiding principle. This involved applying Ohm's law and Kirchhoff's law to evaluate the resistances of components within the circuit, utilising known voltage and current across components and around nodes. In this analogy, pressure equates to voltage, and flow corresponds to current.

To achieve our modeling objectives, insights were leveraged of the system to assess both known and unknown parameters, which informed the development of the model assumptions. A thorough breakdown of the entire system was conducted, converting the system into electronic components to assess the dynamics of the pump, reverse osmosis component, and the Clark. This breakdown revealed symmetrical asynchronous subcircuits within the Clark. Subsequently, the system was conceptualised as a multi-component electrical circuit, and a model was derived based on voltage (V), current (I), resistance (R), capicatance (C) and inductance (L) equivalences.

This process involved disassembling and reconfiguring the system to evaluate resistance values for different components. Three separate configurations were devised to asses the bottom chamber, charging cycle and discharging cycle, reffered to as the spring, rectifier bridge, and pistonless configurations respectively.

A super fast 5 kHz sampling rate piece of code was developed for the arduino to capture eight analog input data input streams from the system. A MATLAB code was written and refined to convert and synchronise multiple data streams to the same time intervals and analyse them using regression techniques.

The analysis of the rectifier bridge configuration revealed a notable correlation between voltage increase and current, supporting the fundamental tenet of Ohm's law, where resistance decreases with lower voltage and current. Furthermore, the results indicate a statistically significant relationship, demonstrating that resistance is a strong function of frequency, particularly within the internal topology of the bottom section of the Clark system, where increased resistance to flow is observed when the input signal is modulated at

higher speeds, as discussed in the previous Section 7.4.1.

The spring configuration model was represented by the two operational states of the Clark sub-circuits: charging and discharging. Corresponding equations were developed to represent the voltage loss due to leakage across the piston head and the voltage gain from the spring's return. The capacitance was the dependent variable, expressed in integral form.

During post-analysis, it was discovered that a fundamental error had occurred while regressing the sets of values representing voltage (V) and capacitance (C) derived from system data. The two equations contained two unknowns, leading to incorrect results in half of the post-processing regression outputs. However, the correctly regressed values appeared to support the initial assumptions and validate the model.

Although the results were incomplete, the correct values reinforced the validity the approach, suggesting that the model accurately represented the system dynamics. Consequently, the erroneous results were omitted from the thesis. Efforts are ongoing to rectify this mistake, gather the required data, and publish the corrected results in a paper co-authored with Dr. Noel McWilliam.

As discussed previously, for the set of pistonless configuration experiments, the configuration was kept the same as the spring configuration, with the piston head flipped. Due to the asymmetry of the piston head, it was postulated that reversing the orientation of the piston head and conducting the same tests as the spring configuration could serve as a proxy for flow in the opposite direction.

Unfortunately, the test had to be abandoned because this resulted in irreparable damage to the piston head. This failure led to the discovery of an entirely different approach to the configuration. Instead of reversing the piston head, it was suggested that channelling the flow input through the RO return port of the top section of the Clark could achieve the desired results. This alternative method promises to be a more robust and effective way to explore the system's

behaviour without risking damage to the piston head.

Future work will focus on implementing this new configuration and conducting thorough tests to validate its efficacy. The findings from these experiments will be documented and published to provide a comprehensive understanding of the pistonless configuration and its potential advantages.

Post-analysis of the data showed a lag between pressure and flow, with pressure leading flow. Experiments were conducted to evaluate the lag between sensors to justify the operations between values in time series data derived from sensors being physically separated by distance.

Pressure waves propagate through water inside a piped system at approximately the speed of sound in water, aligning with the near-zero observed lag. Therefore, the distance between pressure sensors had a negligible effect on pressure data as the velocity of travel made the readings between instruments almost instantaneous.

To assess the lag time accurately, an additional piece of code was developed to regress the variables of interest. This code allowed for a more precise evaluation of the temporal relationships between pressure and flow measurements.

There was up to 1 second of lag between flow sensors at high frequencies, but at lower frequencies, the lag was indistinguishable from noise.

These tests indicate that Ohm's Law is an appropriate local approximation, given the alignment of the data post-correction for the lag. This supports the validity of using the hydraulic analogy in this context and confirms the reliability of the model.

8

Conclusion Summary

8.1 Reverse Osmosis Model Summary

The application of circuit equivalence technique on the PVRO system assessment has yielded significant insights, particularly regarding the identification of a frequency "sweet spot" that influences membrane resistance modulation.

This discovery could revolutionise the development of input control systems for commercial RO plants, offering a novel approach to manipulating flow dynamics across the membrane. By targeting this frequency sweet spot, operators could potentially increase product output while simultaneously reducing specific energy consumption (SEC), thereby enhancing overall system efficiency and sustainability. Such a breakthrough holds immense promise for the desalination industry, where even marginal improvements in efficiency can translate into substantial cost savings and environmental benefits.

Looking ahead, future research endeavours will focus on further exploring and harnessing the potential of this frequency-based modulation technique.

One key area of investigation will involve delving deeper into how this approach can effectively mitigate polarization concentration issues commonly encountered in RO systems. By disrupting the buildup of solute particles near the membrane surface, research aims to enhance system performance and prolong membrane

lifespan.

Additionally, ongoing efforts will seek to optimise the implementation of this technique across various operational scenarios and system configurations, ensuring its practical viability and scalability for real-world applications.

Through continued experimentation and refinement, the frequency-based modulation approach has the potential to reshape the landscape of membrane-based desalination technologies, paving the way for more efficient, sustainable, and cost-effective water treatment solutions.

8.2 The Energy Recovery Prototype Summary: REDACTED

This section has been omitted due to containing commercially sensitive information.

8.3 The Circuit Equivalence Model Summary

A novel dynamic modelling framework was established and partially verified through the application of the hydraulic analogy for electronic circuits to the PVRO system. This innovative approach utilized Ohm's law and Kirchhoff's law to evaluate the resistances within the system. By redefining the system as a multi-component electrical circuit, insights into the dynamics of the pump, reverse osmosis component, and the Clark subcircuits were gained.

The results from the rectifier bridge configuration confirmed the applicability of Ohm's law, showing a strong correlation between voltage increase and current. It was found that resistance is a significant function of frequency, with higher modulation speeds resulting in increased resistance to flow. The spring configuration model, despite some initial errors, supported the assumptions and

validated the model, indicating a potential for further refinement.

In the pistonless configuration, an innovative approach was discovered following an initial test failure. This new method, which involves channeling the flow input through the RO return port of the Clark's top section, offers promising avenues for future research and development.

If fully realised, this dynamic modelling framework could revolutionise the way dynamic systems are modelled. It holds massive potential for future development, not only of IRESs but also of any system that relies on a stochastic dynamic, whether powered by solar irradiance or influenced by a modulating input signal. This framework could lead to significant advancements in energy efficiency and system performance across a variety of applications.

Bibliography

[1] Food and Agriculture Organization of the United Nations. AQUASTAT - FAO's Global Information System on Water and Agriculture. Web link: https://www.fao.org/aquastat/en/overview/methodology/water-use, July 2016.

[2] World Water Assessment Programme. The United Nations World Water Development Report 4: Managing Water under Uncertainty and Risk. UNESCO, Paris, UN Report 2012.

[3] World Energy Council. World Energy Scenarios: Composing energy futures to 2050. London, 2013.

[4] Environmental Investigation Agency. Annual Energy Outlook 2017 with projections to 2050. U.S. Energy Information Administration, annual report 2017.

[5] Food and Agriculture Organization of the United Nations How to Feed the World in 2050. United Nations, Rome, expert forum 2009.

[6] A. Pruss-Ustun et al. Safer water, better health. World Health Organisation, 2008.

[7] Helen Mountford. Water: The Environmental Outlook to 2050. OECD, Paris, presentation 2011.

[8] United Nations World Water Assessment Programme. The United Nations World Water Development Report 2014: Water and Energy. UNESCO, Paris, UNESCO 2014.

[9] Vaclav Smil. Energy in Nature and Society General Energetics of Complex Systems. The MIT Press, 2007.

[10] Dudley Kirk Demographic Transition Theory. Population Studies 50; 1996: 361-387.

[11] Mehran Moalem. We Could Power The Entire World By Harnessing Solar Energy From 1% Of The Sahara. Web link https://www.forbes.com/sites/quora/2016/09/22/we-could-power-the-entireworld- by-harnessing-solar-energy-from-1-of-the-sahara, September 2006

[12] T.J. Saktisahdan, A. Jannifar, M.H. Hasan, H.S.C. Matseelar T.M.I. Mahlia. A review of available methods and development on energy storage; technology update. *Renewable and Sustainable Energy Reviews*, vol. 33, pp. 532-545, 2014.

[13] Meihong Wang Mathew Aneke. Energy storage technologies and real life applications – A state of the art review. *Applied Energy*, vol. 179, pp. 350-377, 2016.

[14] A. G. Olabi. Renewable energy and energy storage systems *Energy*, vol. 136, pp. 1-6, July 2017.

[15] SBC Energy Institute. Electricity Storage. SBC Energy Institute, Presentation 2013.

[16] SBC Energy Institute. Hydrogen Based Energy Conversion SBC Energy Institute, Gravenhage, Presentation 2014.

[17] International Renewable Energy Agency. Thermal Energy Storage. Technology Brief 2013.

[18] Nicole Pfleger, Thomas Bauer, Claudia Martin, Markus Eck, Antje Wörner. Thermal energy storage – overview and specific insight into nitrate salts for sensible and latent heat storage. *Belstein Journal of Nanotechnology*, vol. 6, pp. 1487-1497, 2015.

[19] A.B. Gallo, J.R. Simões-Moreira, H.K.M. Costa, M.M. Santos, E. Moutinho dos Santos,. Energy storage in the energy transition context: A technology review. *Renewable and Sustainable Energy Review*, vol. 62, pp. 800-822, 2016.

[20] Ahmed Alkaisi, Ruth Mossad, Ahmad Sharifian-Barforoush. A review of water desalination systems integrated with renewable energy. *Energy Procedia*, vol.110, pp. 268-274, 2017.

[21] Chiung-Wen Hsu, Chih-Min Hsiung, Chiu-Yue Lin Pao-Long Chang. Constructing an innovative Bio-Hydrogen Integrated Renewable Energy System. *International Journal of Hydrogen Energy*, no. 38, pp. 15660-15669, 2013.

[22] Anurag Chauhan, R.P. Saini. Size optimisation and demand response of a stand alone integrated renewable energy system. *Energy*, vol. 124, pp. 59-73, 2017.

[23] William Hickman, Aramazd Muzhikyan, Amro M. Farid. The synergistic role of renewable energy integration into the unit commitment of the water energy nexus. *Renewable Energy*, vol. 108, pp. 220-229, 2017.

[24] Anurag Chuahan, R.P. Saini. Discrete harmony search based size optimisation of Integrated Renewable Energy System for remote rural areas of Uttarakhand state in India. *Renewable Energy*, Elsevier, vol. 94, pp. 587-604, 2016.

[25] Oluwamayowa O. Amusat, Paul R. Shearing, Eric S. Fraga. Optimal integrated energy systems design incorporating variable renewable energy

sources. *Computers & Chemical Engineering* Elsevier, vol. 95, pp. 21-37, 2016.

[26] S. Rajanna, R.P. Saini. Modelling of integrated renewable energy systems for electrification of remote area in India. *Renewable Energy], Elsevier, vol. 90, pp. 175-187, 2016.*

[27] Anurag Chauhan, R.P. Saini. Techno-economic feasibility study on Integrated Renewable Energy System for an isolated community of India. *Renewable and Sustainable Energy Reviews* Elsevier, vol. 59, pp. 388-405, 2016.

[28] I. Dinceer, M. Agelin-Chaab F. Suleman. Development of an integrated renewable energy system for multigeneration. *Energy*, vol. 78, pp. 196-204, 2014.

[29] M. Walker, D. Poggio, M. Pourkashanian, W. Nimmo J.G. Castellanos. Modelling an off-grid integrated renewable energy system for rural electrification in India using photovoltaics and anaerobic digestion. *Renewable Energy*, vol. 74, pp. 390-398, 2015.

[30] Christian Breyera Otto Koskinena. Energy Storage in Global and Transcontinental Energy Scenarios: A Critical Review. *Energy Procedia*, vol. 99, pp. 53-63, 2016.

[31] Kanase-Patil, R.P. Saini, M.P. Shaini A.B. Integrated reneawble energy systems for off grid rural electrification of remote area. *Renewable Energy*, vol. 35, no.6, pp. 1342-1349, 2010.

[32] Noreddine Ghaffour, Jochen Bundschuh, Hacene Mahmoudi, Mattheus F.A. Goosen. Renewable energy-driven desalination technologies: A comprehensive review on challenges and potential applications of integrated systems. *Desalination*, vol. 356, pp. 94-114, 2015.

[33] M. Methnani. Influence of fuel costs on seawater desalination options. *Desalination*, vol. 1-3, no. 205, pp. 332-339, 2007.

[34] E. Hassan. Desalination Integration with Renewable Energy for Climate Change Abatement in the MENA Region. *Recent Progress in Desalination, Environmental and Marine Outfall Systems*, Springer, pp 159-173., 2015.

[35] Muhammad Shuja Azhar, Ghaus Rizvi, Ibrahim Dincer. Integration of renewable energy based multigeneration system with desalination. *Desalination*, vol. 404, pp. 72-78, 2017.

[36] Janette Hogerwaard, Ibrahim Dincer, Greg F. Naterer. Solar energy based integrated system for power generation, refrigeration and desalination. *Applied Thermal Engineering*, vol. 121, pp. 1059-1069, 2017.

[37] United Nations. Transforming Our World: The 2030 Agenda for Sustainable Development. Web Link: https://sustainabledevelopment.un.org/content/documents/21252030 Agenda for Sustainable Development web.pdf , February 2023

[38] Max Roser. Two centuries of rapid global population growth will come to an end. Web Link: https://ourworldindata.org/world-population-growth-past-future

[39] United Nations. Global Issues: Population. Web Link: https://www.un.org/en/global-issues/population

[40] David Attenboruogh. Video Conference: addressinf the UN council. Web Link: https://www.reuters.com/business/environment/david-attenborough-un-climate-change-threat-global-security-i-dont-envy-you-2021-02-23/

[41] United NAtions. Igniting the Spark Of a Clean Energy Revolution. Web Link: https://www.un.org/en/desa/igniting-spark-clean-energy-revolution

[42] Lorenzo Rosa et al. The water footprint of carbon capture and storage technologies *Renewable and Sustainable Energy Reviews*, Elsevier, pp 159-173, 2021.

[43] Sara Sneath. The cost to capture carbon? More water and electricity The Gaurdian, 2022.

[44] United NAtions. Global Issues: Food. Web Link: https://www.un.org/en/global-issues/food

[45] OCHA Water Stress by Country: 2040 Web Link: https://reliefweb.int/map/world/water-stress-country-2040

[46] OCHA Water Challenges for Geologic Carbon Capture and Sequestration *Environmental Management*, SPringerlink, vol 45, pp 651-661, 2010

[47] IEA Capacity of large-scale CO2 capture projects, current and planned vs the Net Zero Scenario, 2020-2030 Web Link: https://www.iea.org/data-and-statistics/charts/capacity-of-large-scale-co2-capture-projects-current-and-planned-vs-the-net-zero-scenario-2020-2030

[48] ING High energy prices are another test for the resilience of food producers Web Link: https://think.ing.com/articles/high-energy-prices-yet-another-test-for-the-resilience-of-food-producers-ot

[49] World Health Organisation UN Report: Global hunger numbers rose to as many as 828 million in 2021 web Link: https://www.who.int/news/item/06-07-2022-un-report–global-hunger-numbers-rose-to-as-many-as-828-million-in-2021

[50] IEA World Energy Outlook 2022 Web Link https://www.iea.org/reports/world-energy-outlook-2022

[51] Tom Clarke Nuclear fusion breakthrough offers hope for future generations - but the reality may be more complicated Web Link https://news.sky.com/story/amp/nuclear-fusion-breakthrough-offers-hope-for-future-generations-but-the-reality-may-be-more-complicated-12767678

[52] Iain Sample US scientists confirm 'major breakthrough' in nuclear fusion web Link https://www.theguardian.com/environment/2022/dec/13/us-scientists-confirm-major-breakthrough-in-nuclear-fusion

[53] S Jackson, E Brodal A comparison of the energy consumption for CO2 compression process alternatives *IOP Conference Series: Earth and Environmental Science*, IOP Publishing, 167, pp 1-13, 2018

[54] Karl W. Bandilla Carbon Capture and Storage *Future Energy (Third Edition)*, Elsevier, 31, pp 669-692, 2020

[55] Ross Peel et al. Nuclear Security and Safeguards Considerations for Novel Advanced Reactors *Centre for Science and Security Studies; Report*, King's College London, 2022

[56] Amanda S Adams, David W Keith Are global wind power resource estimates overstated? *Environmental research Letters*, IOP, 8, 2013

[57] Asis Sarkar, Dhiren Kumar Behera Wind Turbine Blade Efficiency and Power Calculation with Electrical Analogy *International Journal of Scientific and Research Publications* , Volume 2, Issue 2, February 2012

[58] Tan Woan Wen, C. Palanichamy, Gobbi Ramasamy Small Wind Turbines as Partial Solution for EnergySustainability of Malaysia *International Journal of Energy Economics and Policy,*, 9(2), pp 257-266, 2019

[59] Clark Permar LIQUID TREATMENT APPARATUS FOR PROVIDING A FLOW OF PRESSURIZED LIQUID *United States Patent: Permar* Patent Number 5462414, Date of Patent Oct. 31, 1995

[60] Leslie Wilson Reverse osmosis liquid purification apparatus *United States Patent: Wilson Leslie P S* Patent Number US-4367140-A, Date of Patent Nov. 5, 1979

[61] Murray Thomson Reverse-Osmosis Desalination of Seawater Powered by Photovoltaics Without Batteries *A Doctoral Thesis* Loughborough, 30/06/2003

[62] Spectra Watermakers Inc. Web Page: Our Technology web Link https://www.spectrawatermakers.com/us/us/products/our-technology accessed: 01/03/2023

[63] EcoHydro Solutions Co., Ltd. Web Page: The Clark Pump web Link https://www.ecohydrosolutions.com/Technologies/Clark.html accessed: 01/03/2023

[64] Seatech Marine Grade Products Web Page: Spectra Watermakers web Link https://www.seatechmarineproducts.com/spectra-watermakers/ accessed: 01/03/2023

[65] Alberta's Oil Sands 2006 Alberta Department of Energy web Link https:www.energy.gov.ab.ca/OilSands/pdfs/osgenbrf.pdf accessed: 05/04/2023

[66] Fernandez de Canete et al Physical modelling and computer simulation of the cardiorespiratory system based on the use of a combined electrical analogy *MATHEMATICAL AND COMPUTER MODELLING OF DYNAMICAL SYSTEMS 2021* , VOL. 27, NO. 1, 453–488

[67] Hyein Shin et al Comparative Analysis of the Two Paradigms in the Hydraulic Analogy *New Phys.: Sae Mulli* May 31 2022; 72: 419-428

[68] Kwang W. Oh et al Design of pressure-driven microfluidic networks using electric circuit analogy *Lab on a Chip* issue 3; 2012

[69] Quynh M. Nguyen et al Tesla's fluidic diode and the electronic-hydraulic analogy *American Journal of Physics* 89, 393, (2021)

[70] Goudarzi et al Direct pore-level examination of hydraulic-electric analogy in unconsolidated porous media *In Journal of Petroleum Science and Engineering* June 2018 165:811-820

[71] Thane Heins Georgia State University https://www.slideshare.net/PDiCEOThaneHeins3240/georgia-state-

university-hyperphysics-how-newtonian-mechanics-is-incorrectly-being-applied-to-explain-the-laws-of-electricity-and-magnetism accessed 05/04/2023

[72] Tom Greenslade Kenyon College *The Hydraulic Analogy for Electric Current* 2003

[73] Oliver J. Lodge MacMil- lan and Company *Modern Views on Electricity I* New York, 1889, pp. 54–62

[74] Sourav Gupta Understanding ESR and ESL in Capacitors https://circuitdigest.com/tutorial/understanding-esr-and-esl-in-capacitors accesssed 05/04/2023

[75] Trevor Gamblin Understanding Electricity with Hydraulics https://www.allaboutcircuits.com/technical-articles/understanding-electricity-with-hydrodynamics/ accesssed 05/04/2023

[76] United Nations The Sustainable Development Goals Report 2021 https://unstats.un.org/sdgs/report/2021/ accesssed 05/04/2023

[77] Nature What the fusion breakthrough in the US means for Europe https://www.nature.com/articles/d43978-022-00171-5 accesssed 21/12/2022

[78] Al-Mutaz, Al-Ghunaimi THE IDA WORLD CONGRESS ON DESALINATION AND WATER REUSE *Performance of Reverse Osmosis Units at High Temperatures* 2001

[79] Shigidi et al MDPI *Temperature Impact on Reverse Osmosis Permeate Flux in the Remediation of Hexavalent Chromium* 24/12/2021

[80] Damianou and Lawrence MDPI http://mlss.tuebingen.mpg.de/2015/slides/ghahramani/gp-neural-nets15.pdf 24/12/2021

[81] Kiran Kumar Panigrahi Difference between Laplace Transform and Fourier Transform https://www.tutorialspoint.com/difference-between-laplace-transform-and-fourier-transform 24/12/2021

[82] DHisham Maddah King Abdulaziz University *Application of The Solution-Diffusion Model to Optimize Water Flux in Reverse Osmosis Desalination Plan* 24/12/2021

[83] Haya Nassrullah, Shaheen Fatima Anis, Raed Hashaikeha, Nidal Hilala Energy for desalination: A state-of-the-art review *Desalination, Volume 491, 2020, 114569,* 2020

[84] J. S. Johnson, Jr., L. Dresner and K. A. Kraus Chapter 8 in Principles of Desalination *K. S. Spiegler (Ed.), Academic Press, New York* 1966

[85] National Grid How much of the UK's energy is renewable? *https://www.nationalgrid.com/stories/energy-explained/how-much-uks-energy-renewable* accessed 2024

[86] International Energy Agency Hydropower is the forgotten giant of low-carbon electricity *Hydropower Special Market Report Executive summary* accessed 2024

[87] National Grid Renewable Energy Percentage UK *https://www.cladcodecking.co.uk/blog/post/renewable-energy-percentage-uk* accessed 2024

[88] Statista Research Department Number of sites generating electricity from hydropower in the United Kingdom (UK) from 2003 to 2022 https://www.statista.com/statistics/518390/uk-hydro-energy-sites/ accessed 2024

[89] Drax ltd Producing power: Hydro power energy generation in the UK https://energy.drax.com/insights/hydro-power-in-the-UK/ accessed 2024

[90] Department for Energy Security and Net Zero, Environment Agency and Department for Business, Energy and Industrial Strategy

Harnessing hydroelectric power https://www.gov.uk/guidance/harnessing-hydroelectric-power accessed 2024

[91] Vanessa Martin Chapter 5: Electricity *Digest of UK energy statistics DUKES* accessed 2024

[92] Inemesit Ukpanah UK's Wind Power: A Gust of Growth in the Renewable Energy Sector https://www.greenmatch.co.uk/green-energy/wind accessed 2024

[93] Michael Sexton SILENT FLOOD: AUSTRALIA'S SALINITY CRISIS *ABC Books, Sydney* 2003

[94] Lumen Learning Entropy and the Second Law of Thermodynamics: Disorder and the Unavailability of Energy https://courses.lumenlearning.com/suny-physics/chapter/15-6-entropy-and-the-second-law-of-thermodynamics-disorder-and-the-unavailability-of-energy/ 2023

[95] Bhausaheb L. Pangarkar, Mukund G. Sane, and Mahendra Guddad1 Reverse Osmosis and Membrane Distillation for Desalination of Groundwater: A Review 2011 *International Scholarly Research Network, ISRN Materials Science, Volume 2011, Article ID 523124, 9 pages* 2011

[96] Lauren Greenlee et al Reverse osmosis desalination: Water sources, technology, and today's challenges *Water Research Volume 43, Issue 9* May 2009

A

Appendix A: system modelling techniques

A.1 Bode Plots

Before delving into the details of system identification and frequency response analysis, it's important to understand the tools used for visualising these concepts. One of the most effective tools for this purpose is the Bode plot. A Bode plot is a graphical representation that shows how the gain and phase of a system respond to different frequencies. It consists of two separate graphs: the first plots the gain (in decibels) against the frequency, and the second plots the phase angle against the same frequency. Both graphs share the x-axis, which represents the frequency in a logarithmic scale (base 10). In more detail, the first graph of the Bode plot shows the gain of the system, typically measured in decibels (dB), on the y-axis, while the x-axis represents the frequency response of the system. The second graph, which complements the first, plots the phase angle on the y-axis against the same frequency on the x-axis. The use of a logarithmic scale for the frequency axis allows for a wide range of frequencies to be represented in a compact form, making it easier to observe how the system behaves across different frequency ranges. Bode plots are a very useful way to represent the gain and phase of a system as a function of frequency, providing clear insights into the stability and performance characteristics of the system.

A.2 Laplace Transform vs the Fast Fourier Transform

Engineering analysis involves the mathematical modeling of physical systems. Often, these models are too complex to solve directly using traditional methods. To address this, a common technique is to apply a transform function to the model, converting it into a simpler form. This transformation allows for easier manipulation and often reduces the complexity of the equations. Once the model is simplified and solved in this transformed space, an inverse transform is applied to convert the solution back to its original form.

Two commonly used transform functions are the integral transforms of Laplace and Fourier. Both the Laplace and Fourier transform take physical systems represented by differential equations, convert them into algebraic equations or an easier set of differentials of lower degree.

The Laplace Transform is a mathematical tool which is used to convert the differential equations representing a linear time invariant system in time domain into algebraic equations in the frequency domain.

The Laplace transform of a time domain function $x(t)$ is defined as:

$$L[x(t)] = X(s) = \int_0^\infty x(t)e^{-st}dt$$

where, s is a complex variable

$$s = \sigma + j\omega$$

The Laplace transform operator L transforms the time domain function $x(t)$ into the frequency domain function $X(s)$.

The Fourier Transform fits a superposition of sine waves to a continuous time domain signal, converting the signal into its component frequencies and presenting the signal in the frequency domain. The Fourier transform of a

continuous-time signal $x(t)$ is defined as

$$F[x(t)] = X\omega = \int_{-\infty}^{\infty} x(t)e^{-j\omega}dt$$

The Fourier Transform analyses a function in frequency domain and is limited to real numbers. However, the Laplace transform analyses function in the complex plain and can be used to analyse unstable systems [81].

System identification is a data driven approach to modelling the dynamics of a system. A frequency response method allows the user to determine the model structure of system by evaluating its response to an input frequency. From the results a Bode plot can be used to visualise the frequency response of a system across the entire spectrum.

The benefits of a linear time-invariant (LTI) system with regards to modelling are significant. LTI systems have two properties; they are linear and time-invariant.

Linear systems ensure that if a scalar is applied to the input, u, the output y is scaled by the same amount. LTI's also adhere to the principle of superposition. When two inputs, $u1 + u2$, are passed through the system the outputs will be $y1 + y2$. The scaling property holds in conjunction with the superposition and the superposition with linear scaling.

Time-invariance means that any input, u, will produce an output y with some lag in time applied.

LTI systems benefit from only having a limited number of mathematical operations that can be applied.

1. integration of the input signal $\int u(t)\,du$
2. differentiation of the input signal $\frac{du(t)}{dt}$
3. superpostion of the input signal $u_1(t) + u_2(t)$

4. subtraction by adding a negative $u_1(t) + (-u_2(t))$
5. multiplication by a constant $u(t) \times a$
6. division by muliplying by the reciprocal $u(t) \times \frac{1}{a}$

When a sinewave is used as an input for $x\theta$ the same shaped wave will be present in $y\theta$ i.e. the frequency will be left unchanged. The amplitude and phase may have been changed and these can be easily evaluated using the mathematical operators above and the Laplace transform function.

The Laplace transform is a function in the form $S = \sigma + j\omega$. At steady state the transient term σ decays to 0, therefore $S = j\omega$.

The transfer function, $\frac{y(s)}{u(s)}$ is $H(S)$, which is the ratio between the complex representations of the $y(S)$ outputs and the $u(S)$ inputs.

The gain is determined by evaluating the square root of the real part squared plus the imaginary part squared.

$$Gain = \sqrt{real^2 + imaginary^2}$$

Likewise, the change in phase can be evaluated by taking the argument of the imaginary part and the real part.

$$\theta(phase) = arctan2(imaginary, real)$$

A Bode plot maps the gain and phase change of the frequency response over all frequencies. It is a two graph plot that maps frequency on a logarithmic scale against gain in decibels on the top plot and frequency against phase shift on the bottom plot.

To convert to dB take log base 10 of the ratio of amplitudes of the input and output signal and multiply by 20.

$$dB = 20log10\frac{A1}{A2}$$

Theta can be evaluated for all values of omega in rads per second and plotted on the frequency phase graph of the Bode plot.

B

Appendix B: code progression

B.1 Arduino

B.1.1 5 kHz data logger

NB This code was developed to read upto 8 analog pins from an Arduino with a sampling rate of 1 kHz to 5 kHz.

```
/**
 * This program logs data from the Arduino ADC to a binary file.
 *
 * Samples are logged at regular intervals. Each Sample consists of the ADC
 * values for the analog pins defined in the PIN_LIST array.  The pins numbers
 * may be in any order.
 *
 * Edit the configuration constants below to set the sample pins, sample rate,
 * and other configuration values.
 *
 * If your SD card has a long write latency, it may be necessary to use
 * slower sample rates.  Using a Mega Arduino helps overcome latency
 * problems since 13 512 byte buffers will be used.
 *
```

```
 * Each 512 byte data block in the file has a four byte header followed by up
 * to 508 bytes of data. (508 values in 8-bit mode or 254 values in 10-bit mode)
 * Each block contains an integral number of samples with unused space at the
 * end of the block.
 *
 * Data is written to the file using a SD multiple block write command.
 */
#ifdef __AVR__
#include <SPI.h>
#include "SdFat.h"
#include "FreeStack.h"
#include "AnalogBinLogger.h"
//------------------------------------------------------------------------------
// Analog pin number list for a sample.  Pins may be in any order and pin
// numbers may be repeated.
const uint8_t PIN_LIST[] = {0, 1, 2, 3, 4, 5, 6, 7};
//------------------------------------------------------------------------------
// Sample rate in samples per second.
const float SAMPLE_RATE = 5000;  // Must be 0.25 or greater.

// The interval between samples in seconds, SAMPLE_INTERVAL, may be set to a
// constant instead of being calculated from SAMPLE_RATE.  SAMPLE_RATE is not
// used in the code below.  For example, setting SAMPLE_INTERVAL = 2.0e-4
// will result in a 200 microsecond sample interval.
const float SAMPLE_INTERVAL = 1.0/SAMPLE_RATE;

// Setting ROUND_SAMPLE_INTERVAL non-zero will cause the sample interval to
// be rounded to a a multiple of the ADC clock period and will reduce sample
// time jitter.
#define ROUND_SAMPLE_INTERVAL 1
//------------------------------------------------------------------------------
```

```
// ADC clock rate.
// The ADC clock rate is normally calculated from the pin count and sample
// interval.  The calculation attempts to use the lowest possible ADC clock
// rate.
//
// You can select an ADC clock rate by defining the symbol ADC_PRESCALER to
// one of these values.  You must choose an appropriate ADC clock rate for
// your sample interval.
// #define ADC_PRESCALER 7 // F_CPU/128 125 kHz on an Uno
// #define ADC_PRESCALER 6 // F_CPU/64  250 kHz on an Uno
// #define ADC_PRESCALER 5 // F_CPU/32  500 kHz on an Uno
// #define ADC_PRESCALER 4 // F_CPU/16 1000 kHz on an Uno
// #define ADC_PRESCALER 3 // F_CPU/8  2000 kHz on an Uno (8-bit mode only)
//------------------------------------------------------------------------------
// Reference voltage.  See the processor data-sheet for reference details.
// uint8_t const ADC_REF = 0; // External Reference AREF pin.
uint8_t const ADC_REF = (1 << REFS0);  // Vcc Reference.
// uint8_t const ADC_REF = (1 << REFS1);  // Internal 1.1 (only 644 1284P Mega)
// uint8_t const ADC_REF = (1 << REFS1) | (1 << REFS0);  // Internal 1.1 or 2.56
//------------------------------------------------------------------------------
// File definitions.
//
// Maximum file size in blocks.
// The program creates a contiguous file with FILE_BLOCK_COUNT 512 byte blocks.
// This file is flash erased using special SD commands.  The file will be
// truncated if logging is stopped early.
const uint32_t FILE_BLOCK_COUNT = 256000;

// log file base name.  Must be six characters or less.
#define FILE_BASE_NAME "analog"
```

```
// Set RECORD_EIGHT_BITS non-zero to record only the high 8-bits of the ADC.
#define RECORD_EIGHT_BITS 0
//------------------------------------------------------------------------------
// Pin definitions.
//
// Digital pin to indicate an error, set to -1 if not used.
// The led blinks for fatal errors. The led goes on solid for SD write
// overrun errors and logging continues.
const int8_t ERROR_LED_PIN = 3;

// SD chip select pin.
const uint8_t SD_CS_PIN = SS;
//------------------------------------------------------------------------------
// Buffer definitions.
//
// The logger will use SdFat's buffer plus BUFFER_BLOCK_COUNT additional
// buffers.  QUEUE_DIM must be a power of two larger than
//(BUFFER_BLOCK_COUNT + 1).
//
#if RAMEND < 0X8FF
#error Too little SRAM
//
#elif RAMEND < 0X10FF
// Use total of two 512 byte buffers.
const uint8_t BUFFER_BLOCK_COUNT = 1;
// Dimension for queues of 512 byte SD blocks.
const uint8_t QUEUE_DIM = 4;  // Must be a power of two!
//
#elif RAMEND < 0X20FF
// Use total of five 512 byte buffers.
const uint8_t BUFFER_BLOCK_COUNT = 4;
```

```
// Dimension for queues of 512 byte SD blocks.
const uint8_t QUEUE_DIM = 8;  // Must be a power of two!
//
#elif RAMEND < 0X40FF
// Use total of 13 512 byte buffers.
const uint8_t BUFFER_BLOCK_COUNT = 12;
// Dimension for queues of 512 byte SD blocks.
const uint8_t QUEUE_DIM = 16;  // Must be a power of two!
//
#else  // RAMEND
// Use total of 29 512 byte buffers.
const uint8_t BUFFER_BLOCK_COUNT = 28;
// Dimension for queues of 512 byte SD blocks.
const uint8_t QUEUE_DIM = 32;  // Must be a power of two!
#endif  // RAMEND
//==============================================================================
// End of configuration constants.
//==============================================================================
// Temporary log file.  Will be deleted if a reset or power failure occurs.
#define TMP_FILE_NAME "tmp_log.bin"

// Size of file base name.  Must not be larger than six.
const uint8_t BASE_NAME_SIZE = sizeof(FILE_BASE_NAME) - 1;

// Number of analog pins to log.
const uint8_t PIN_COUNT = sizeof(PIN_LIST)/sizeof(PIN_LIST[0]);

// Minimum ADC clock cycles per sample interval
const uint16_t MIN_ADC_CYCLES = 15;

// Extra cpu cycles to setup ADC with more than one pin per sample.
```

```
const uint16_t ISR_SETUP_ADC = PIN_COUNT > 1 ? 100 : 0;

// Maximum cycles for timer0 system interrupt, millis, micros.
const uint16_t ISR_TIMER0 = 160;
//==============================================================================
SdFat sd;

SdBaseFile binFile;

char binName[13] = FILE_BASE_NAME "00.bin";

#if RECORD_EIGHT_BITS
const size_t SAMPLES_PER_BLOCK = DATA_DIM8/PIN_COUNT;
typedef block8_t block_t;
#else  // RECORD_EIGHT_BITS
const size_t SAMPLES_PER_BLOCK = DATA_DIM16/PIN_COUNT;
typedef block16_t block_t;
#endif // RECORD_EIGHT_BITS

block_t* emptyQueue[QUEUE_DIM];
uint8_t emptyHead;
uint8_t emptyTail;

block_t* fullQueue[QUEUE_DIM];
volatile uint8_t fullHead;  // volatile insures non-interrupt code sees changes.
uint8_t fullTail;

// queueNext assumes QUEUE_DIM is a power of two
inline uint8_t queueNext(uint8_t ht) {
  return (ht + 1) & (QUEUE_DIM -1);
}
```

```
//==============================================================================
// Interrupt Service Routines

// Pointer to current buffer.
block_t* isrBuf;

// Need new buffer if true.
bool isrBufNeeded = true;

// overrun count
uint16_t isrOver = 0;

// ADC configuration for each pin.
uint8_t adcmux[PIN_COUNT];
uint8_t adcsra[PIN_COUNT];
uint8_t adcsrb[PIN_COUNT];
uint8_t adcindex = 1;

// Insure no timer events are missed.
volatile bool timerError = false;
volatile bool timerFlag = false;
//------------------------------------------------------------------------------
// ADC done interrupt.
ISR(ADC_vect) {
  // Read ADC data.
#if RECORD_EIGHT_BITS
  uint8_t d = ADCH;
#else  // RECORD_EIGHT_BITS
  // This will access ADCL first.
  uint16_t d = ADC;
#endif  // RECORD_EIGHT_BITS
```

```
if (isrBufNeeded && emptyHead == emptyTail) {
  // no buffers - count overrun
  if (isrOver < 0XFFFF) {
    isrOver++;
  }

  // Avoid missed timer error.
  timerFlag = false;
  return;
}
// Start ADC
if (PIN_COUNT > 1) {
  ADMUX = adcmux[adcindex];
  ADCSRB = adcsrb[adcindex];
  ADCSRA = adcsra[adcindex];
  if (adcindex == 0) {
    timerFlag = false;
  }
  adcindex =  adcindex < (PIN_COUNT - 1) ? adcindex + 1 : 0;
} else {
  timerFlag = false;
}
// Check for buffer needed.
if (isrBufNeeded) {
  // Remove buffer from empty queue.
  isrBuf = emptyQueue[emptyTail];
  emptyTail = queueNext(emptyTail);
  isrBuf->count = 0;
  isrBuf->overrun = isrOver;
  isrBufNeeded = false;
```

```
  }
  // Store ADC data.
  isrBuf->data[isrBuf->count++] = d;

  // Check for buffer full.
  if (isrBuf->count >= PIN_COUNT*SAMPLES_PER_BLOCK) {
    // Put buffer isrIn full queue.
    uint8_t tmp = fullHead;  // Avoid extra fetch of volatile fullHead.
    fullQueue[tmp] = (block_t*)isrBuf;
    fullHead = queueNext(tmp);

    // Set buffer needed and clear overruns.
    isrBufNeeded = true;
    isrOver = 0;
  }
}
//------------------------------------------------------------------------------
// timer1 interrupt to clear OCF1B
ISR(TIMER1_COMPB_vect) {
  // Make sure ADC ISR responded to timer event.
  if (timerFlag) {
    timerError = true;
  }
  timerFlag = true;
}
//==============================================================================
// Error messages stored in flash.
#define error(msg) {sd.errorPrint(F(msg));fatalBlink();}
//------------------------------------------------------------------------------
//
void fatalBlink() {
```

```
  while (true) {
    if (ERROR_LED_PIN >= 0) {
      digitalWrite(ERROR_LED_PIN, HIGH);
      delay(200);
      digitalWrite(ERROR_LED_PIN, LOW);
      delay(200);
    }
  }
}
//============================================================================
#if ADPS0 != 0 || ADPS1 != 1 || ADPS2 != 2
#error unexpected ADC prescaler bits
#endif
//------------------------------------------------------------------------------
// initialize ADC and timer1
void adcInit(metadata_t* meta) {
  uint8_t adps;  // prescaler bits for ADCSRA
  uint32_t ticks = F_CPU*SAMPLE_INTERVAL + 0.5;  // Sample interval cpu cycles.

  if (ADC_REF & ~((1 << REFS0) | (1 << REFS1))) {
    error("Invalid ADC reference");
  }
#ifdef ADC_PRESCALER
  if (ADC_PRESCALER > 7 || ADC_PRESCALER < 2) {
    error("Invalid ADC prescaler");
  }
  adps = ADC_PRESCALER;
#else  // ADC_PRESCALER
  // Allow extra cpu cycles to change ADC settings if more than one pin.
  int32_t adcCycles = (ticks - ISR_TIMER0)/PIN_COUNT - ISR_SETUP_ADC;
```

```
  for (adps = 7; adps > 0; adps--) {
    if (adcCycles >= (MIN_ADC_CYCLES << adps)) {
      break;
    }
  }
#endif  // ADC_PRESCALER
  meta->adcFrequency = F_CPU >> adps;
  if (meta->adcFrequency > (RECORD_EIGHT_BITS ? 2000000 : 1000000)) {
    error("Sample Rate Too High");
  }
#if ROUND_SAMPLE_INTERVAL
  // Round so interval is multiple of ADC clock.
  ticks += 1 << (adps - 1);
  ticks >>= adps;
  ticks <<= adps;
#endif  // ROUND_SAMPLE_INTERVAL

  if (PIN_COUNT > sizeof(meta->pinNumber)/sizeof(meta->pinNumber[0])) {
    error("Too many pins");
  }
  meta->pinCount = PIN_COUNT;
  meta->recordEightBits = RECORD_EIGHT_BITS;

  for (int i = 0; i < PIN_COUNT; i++) {
    uint8_t pin = PIN_LIST[i];
    if (pin >= NUM_ANALOG_INPUTS) {
      error("Invalid Analog pin number");
    }
    meta->pinNumber[i] = pin;

    // Set ADC reference and low three bits of analog pin number.
```

```
    adcmux[i] = (pin & 7) | ADC_REF;
    if (RECORD_EIGHT_BITS) {
      adcmux[i] |= 1 << ADLAR;
    }

    // If this is the first pin, trigger on timer/counter 1 compare match B.
    adcsrb[i] = i == 0 ? (1 << ADTS2) | (1 << ADTS0) : 0;
#ifdef MUX5
    if (pin > 7) {
      adcsrb[i] |= (1 << MUX5);
    }
#endif  // MUX5
    adcsra[i] = (1 << ADEN) | (1 << ADIE) | adps;
    adcsra[i] |= i == 0 ? 1 << ADATE : 1 << ADSC;
  }

  // Setup timer1
  TCCR1A = 0;
  uint8_t tshift;
  if (ticks < 0X10000) {
    // no prescale, CTC mode
    TCCR1B = (1 << WGM13) | (1 << WGM12) | (1 << CS10);
    tshift = 0;
  } else if (ticks < 0X10000*8) {
    // prescale 8, CTC mode
    TCCR1B = (1 << WGM13) | (1 << WGM12) | (1 << CS11);
    tshift = 3;
  } else if (ticks < 0X10000*64) {
    // prescale 64, CTC mode
    TCCR1B = (1 << WGM13) | (1 << WGM12) | (1 << CS11) | (1 << CS10);
    tshift = 6;
```

```
} else if (ticks < 0X10000*256) {
  // prescale 256, CTC mode
  TCCR1B = (1 << WGM13) | (1 << WGM12) | (1 << CS12);
  tshift = 8;
} else if (ticks < 0X10000*1024) {
  // prescale 1024, CTC mode
  TCCR1B = (1 << WGM13) | (1 << WGM12) | (1 << CS12) | (1 << CS10);
  tshift = 10;
} else {
  error("Sample Rate Too Slow");
}
// divide by prescaler
ticks >>= tshift;
// set TOP for timer reset
ICR1 = ticks - 1;
// compare for ADC start
OCR1B = 0;

// multiply by prescaler
ticks <<= tshift;

// Sample interval in CPU clock ticks.
meta->sampleInterval = ticks;
meta->cpuFrequency = F_CPU;
float sampleRate = (float)meta->cpuFrequency/meta->sampleInterval;
Serial.print(F("Sample pins:"));
for (uint8_t i = 0; i < meta->pinCount; i++) {
  Serial.print(' ');
  Serial.print(meta->pinNumber[i], DEC);
}
Serial.println();
```

```
  Serial.print(F("ADC bits: "));
  Serial.println(meta->recordEightBits ? 8 : 10);
  Serial.print(F("ADC clock kHz: "));
  Serial.println(meta->adcFrequency/1000);
  Serial.print(F("Sample Rate: "));
  Serial.println(sampleRate);
  Serial.print(F("Sample interval usec: "));
  Serial.println(1000000.0/sampleRate, 4);
}
//------------------------------------------------------------------------------
// enable ADC and timer1 interrupts
void adcStart() {
  // initialize ISR

  isrBufNeeded = true;
  isrOver = 0;
  adcindex = 1;

  // Clear any pending interrupt.
  ADCSRA |= 1 << ADIF;

  // Setup for first pin.
  ADMUX = adcmux[0];
  ADCSRB = adcsrb[0];
  ADCSRA = adcsra[0];

  // Enable timer1 interrupts.
  timerError = false;
  timerFlag = false;
  TCNT1 = 0;
  TIFR1 = 1 << OCF1B;
```

```
  TIMSK1 = 1 << OCIE1B;
}
//------------------------------------------------------------------------------
void adcStop() {
  Serial.println(micros()); //MOB EDIT
  TIMSK1 = 0;
  ADCSRA = 0;
}
//------------------------------------------------------------------------------
// Convert binary file to csv file.
void binaryToCsv() {
  uint8_t lastPct = 0;
  block_t buf;
  metadata_t* pm;
  uint32_t t0 = millis();
  char csvName[13];
  StdioStream csvStream;

  if (!binFile.isOpen()) {
    Serial.println(F("No current binary file"));
    return;
  }
  binFile.rewind();
  if (binFile.read(&buf , 512) != 512) {
    error("Read metadata failed");
  }
  // Create a new csv file.
  strcpy(csvName, binName);
  strcpy(&csvName[BASE_NAME_SIZE + 3], "csv");

  if (!csvStream.fopen(csvName, "w")) {
```

```
  error("open csvStream failed");
}
Serial.println();
Serial.print(F("Writing: "));
Serial.print(csvName);
Serial.println(F(" - type any character to stop"));
pm = (metadata_t*)&buf;
csvStream.print(F("Interval,"));
float intervalMicros = 1.0e6*pm->sampleInterval/(float)pm->cpuFrequency;
csvStream.print(intervalMicros, 4);
csvStream.println(F(",usec"));
for (uint8_t i = 0; i < pm->pinCount; i++) {
  if (i) {
    csvStream.putc(',');
  }
  csvStream.print(F("pin"));
  csvStream.print(pm->pinNumber[i]);
}
csvStream.println();
uint32_t tPct = millis();
while (!Serial.available() && binFile.read(&buf, 512) == 512) {
  if (buf.count == 0) {
    break;
  }
  if (buf.overrun) {
    csvStream.print(F("OVERRUN,"));
    csvStream.println(buf.overrun);
  }
  for (uint16_t j = 0; j < buf.count; j += PIN_COUNT) {
    for (uint16_t i = 0; i < PIN_COUNT; i++) {
      if (i) {
```

```
          csvStream.putc(',');
        }
        csvStream.print(buf.data[i + j]);
      }
      csvStream.println();
    }
    if ((millis() - tPct) > 1000) {
      uint8_t pct = binFile.curPosition()/(binFile.fileSize()/100);
      if (pct != lastPct) {
        tPct = millis();
        lastPct = pct;
        Serial.print(pct, DEC);
        Serial.println('%');
      }
    }
    if (Serial.available()) {
      break;
    }
  }
  csvStream.fclose();
  Serial.print(F("Done: "));
  Serial.print(0.001*(millis() - t0));
  Serial.println(F(" Seconds"));
}
//------------------------------------------------------------------------------
// read data file and check for overruns
void checkOverrun() {
  bool headerPrinted = false;
  block_t buf;
  uint32_t bgnBlock, endBlock;
  uint32_t bn = 0;
```

```
if (!binFile.isOpen()) {
  Serial.println(F("No current binary file"));
  return;
}
if (!binFile.contiguousRange(&bgnBlock, &endBlock)) {
  error("contiguousRange failed");
}
binFile.rewind();
Serial.println();
Serial.println(F("Checking overrun errors - type any character to stop"));
if (binFile.read(&buf , 512) != 512) {
  error("Read metadata failed");
}
bn++;
while (binFile.read(&buf, 512) == 512) {
  if (buf.count == 0) {
    break;
  }
  if (buf.overrun) {
    if (!headerPrinted) {
      Serial.println();
      Serial.println(F("Overruns:"));
      Serial.println(F("fileBlockNumber,sdBlockNumber,overrunCount"));
      headerPrinted = true;
    }
    Serial.print(bn);
    Serial.print(',');
    Serial.print(bgnBlock + bn);
    Serial.print(',');
    Serial.println(buf.overrun);
```

```
    }
    bn++;
  }
  if (!headerPrinted) {
    Serial.println(F("No errors found"));
  } else {
    Serial.println(F("Done"));
  }
}
//------------------------------------------------------------------------------
// dump data file to Serial
void dumpData() {
  block_t buf;
  if (!binFile.isOpen()) {
    Serial.println(F("No current binary file"));
    return;
  }
  binFile.rewind();
  if (binFile.read(&buf , 512) != 512) {
    error("Read metadata failed");
  }
  Serial.println();
  Serial.println(F("Type any character to stop"));
  delay(1000);
  while (!Serial.available() && binFile.read(&buf , 512) == 512) {
    if (buf.count == 0) {
      break;
    }
    if (buf.overrun) {
      Serial.print(F("OVERRUN,"));
      Serial.println(buf.overrun);
```

```
    }
    for (uint16_t i = 0; i < buf.count; i++) {
      Serial.print(buf.data[i], DEC);
      if ((i+1)%PIN_COUNT) {
        Serial.print(',');
      } else {
        Serial.println();
      }
    }
  }
  Serial.println(F("Done"));
}
//------------------------------------------------------------------------------
// log data
// max number of blocks to erase per erase call
uint32_t const ERASE_SIZE = 262144L;
void logData() {
  uint32_t bgnBlock, endBlock;

  // Allocate extra buffer space.
  block_t block[BUFFER_BLOCK_COUNT];

  Serial.println();

  // Initialize ADC and timer1.
  adcInit((metadata_t*) &block[0]);

  // Find unused file name.
  if (BASE_NAME_SIZE > 6) {
    error("FILE_BASE_NAME too long");
  }
```

```
while (sd.exists(binName)) {
  if (binName[BASE_NAME_SIZE + 1] != '9') {
    binName[BASE_NAME_SIZE + 1]++;
  } else {
    binName[BASE_NAME_SIZE + 1] = '0';
    if (binName[BASE_NAME_SIZE] == '9') {
      error("Can't create file name");
    }
    binName[BASE_NAME_SIZE]++;
  }
}
// Delete old tmp file.
if (sd.exists(TMP_FILE_NAME)) {
  Serial.println(F("Deleting tmp file"));
  if (!sd.remove(TMP_FILE_NAME)) {
    error("Can't remove tmp file");
  }
}
// Create new file.
Serial.println(F("Creating new file"));
binFile.close();
if (!binFile.createContiguous(TMP_FILE_NAME, 512 * FILE_BLOCK_COUNT)) {
  error("createContiguous failed");
}
// Get the address of the file on the SD.
if (!binFile.contiguousRange(&bgnBlock, &endBlock)) {
  error("contiguousRange failed");
}
// Use SdFat's internal buffer.
uint8_t* cache = (uint8_t*)sd.vol()->cacheClear();
if (cache == 0) {
```

```
  error("cacheClear failed");
}

// Flash erase all data in the file.
Serial.println(F("Erasing all data"));
uint32_t bgnErase = bgnBlock;
uint32_t endErase;
while (bgnErase < endBlock) {
  endErase = bgnErase + ERASE_SIZE;
  if (endErase > endBlock) {
    endErase = endBlock;
  }
  if (!sd.card()->erase(bgnErase, endErase)) {
    error("erase failed");
  }
  bgnErase = endErase + 1;
}
// Start a multiple block write.
if (!sd.card()->writeStart(bgnBlock, FILE_BLOCK_COUNT)) {
  error("writeBegin failed");
}
// Write metadata.
if (!sd.card()->writeData((uint8_t*)&block[0])) {
  error("Write metadata failed");
}
// Initialize queues.
emptyHead = emptyTail = 0;
fullHead = fullTail = 0;

// Use SdFat buffer for one block.
emptyQueue[emptyHead] = (block_t*)cache;
```

```
emptyHead = queueNext(emptyHead);

// Put rest of buffers in the empty queue.
for (uint8_t i = 0; i < BUFFER_BLOCK_COUNT; i++) {
  emptyQueue[emptyHead] = &block[i];
  emptyHead = queueNext(emptyHead);
}
// Give SD time to prepare for big write.
delay(1000);
Serial.println(F("Logging - type any character to stop"));
// Wait for Serial Idle.
Serial.flush();
delay(10);
uint32_t bn = 1;
uint32_t t0 = millis();
uint32_t t1 = t0;
uint32_t overruns = 0;
uint32_t count = 0;
uint32_t maxLatency = 0;

// Start logging interrupts.
Serial.println(micros()); //MOB EDIT
adcStart();

while (1) {
  if (fullHead != fullTail) {
    // Get address of block to write.
    block_t* pBlock = fullQueue[fullTail];

    // Write block to SD.
    uint32_t usec = micros();
```

```
    if (!sd.card()->writeData((uint8_t*)pBlock)) {
      error("write data failed");
    }
    usec = micros() - usec;
    t1 = millis();
    if (usec > maxLatency) {
      maxLatency = usec;
    }
    count += pBlock->count;

    // Add overruns and possibly light LED.
    if (pBlock->overrun) {
      overruns += pBlock->overrun;
      if (ERROR_LED_PIN >= 0) {
        digitalWrite(ERROR_LED_PIN, HIGH);
      }
    }
    // Move block to empty queue.
    emptyQueue[emptyHead] = pBlock;
    emptyHead = queueNext(emptyHead);
    fullTail = queueNext(fullTail);
    bn++;
    if (bn == FILE_BLOCK_COUNT) {
      // File full so stop ISR calls.
      adcStop();
      break;
    }
  }
  if (timerError) {
    error("Missed timer event - rate too high");
  }
```

```
  if (Serial.available()) {
    // Stop ISR calls.
    adcStop();
    if (isrBuf != 0 && isrBuf->count >= PIN_COUNT) {
      // Truncate to last complete sample.
      isrBuf->count = PIN_COUNT*(isrBuf->count/PIN_COUNT);
      // Put buffer in full queue.
      fullQueue[fullHead] = isrBuf;
      fullHead = queueNext(fullHead);
      isrBuf = 0;
    }
    if (fullHead == fullTail) {
      break;
    }
  }
}
if (!sd.card()->writeStop()) {
  error("writeStop failed");
}
// Truncate file if recording stopped early.
if (bn != FILE_BLOCK_COUNT) {
  Serial.println(F("Truncating file"));
  if (!binFile.truncate(512L * bn)) {
    error("Can't truncate file");
  }
}
if (!binFile.rename(binName)) {
  error("Can't rename file");
}
Serial.print(F("File renamed: "));
Serial.println(binName);
```

```
  Serial.print(F("Max block write usec: "));
  Serial.println(maxLatency);
  Serial.print(F("Record time sec: "));
  Serial.println(0.001*(t1 - t0), 3);
  Serial.print(F("Sample count: "));
  Serial.println(count/PIN_COUNT);
  Serial.print(F("Samples/sec: "));
  Serial.println((1000.0/PIN_COUNT)*count/(t1-t0));
  Serial.print(F("Overruns: "));
  Serial.println(overruns);
  Serial.println(F("Done"));
}
//------------------------------------------------------------------------------
void setup(void) {
  if (ERROR_LED_PIN >= 0) {
    pinMode(ERROR_LED_PIN, OUTPUT);
  }
  Serial.begin(115200);

  // Read the first sample pin to init the ADC.
  analogRead(PIN_LIST[0]);

  Serial.print(F("FreeStack: "));
  Serial.println(FreeStack());

  // Initialize at the highest speed supported by the board that is
  // not over 50 MHz. Try a lower speed if SPI errors occur.
  if (!sd.begin(SD_CS_PIN, SD_SCK_MHZ(50))) {
    sd.initErrorPrint();
    fatalBlink();
  }
```

```
}
//------------------------------------------------------------------------------
void loop(void) {
  // Read any Serial data.
  do {
    delay(10);
  } while (Serial.available() && Serial.read() >= 0);
  Serial.println();
  Serial.println(F("type:"));
  Serial.println(F("c - convert file to csv"));
  Serial.println(F("d - dump data to Serial"));
  Serial.println(F("e - overrun error details"));
  Serial.println(F("r - record ADC data"));

  while(!Serial.available()) {
    SysCall::yield();
  }
  char c = tolower(Serial.read());
  if (ERROR_LED_PIN >= 0) {
    digitalWrite(ERROR_LED_PIN, LOW);
  }
  // Read any Serial data.
  do {
    delay(10);
  } while (Serial.available() && Serial.read() >= 0);

  if (c == 'c') {
    binaryToCsv();
  } else if (c == 'd') {
    dumpData();
  } else if (c == 'e') {
```

```
    checkOverrun();
  } else if (c == 'r') {
    logData();
  } else {
    Serial.println(F("Invalid entry"));
  }
}
#else  // __AVR__
#error This program is only for AVR.
#endif  // __AVR__
```

B.1.2 8 pin checker

NB This is a simple code to check the sensor values of the 8 analog pins of the Arduino. This code was used as a visual reference to quality check the data logging process.

```
const int analogPin0 = A0;
const int analogPin1 = A1;
const int analogPin2 = A2;
const int analogPin3 = A3;
const int analogPin4 = A4;
const int analogPin5 = A5;
const int analogPin6 = A6;
const int analogPin7 = A7;
//const int analogPin8 = A8;
//const int analogPin11 = A11;
```

```
void setup() {
  Serial.begin(115200);
}

void loop() {
//  Serial.print(analogRead(analogPin0));
//  Serial.print(",");
//  Serial.print(analogRead(analogPin1));
//  Serial.print(",");
  Serial.print(analogRead(analogPin2));
  Serial.print(",");
  Serial.print(analogRead(analogPin3));
  Serial.print(",");
  Serial.print(analogRead(analogPin4));
  Serial.print(",");
  Serial.print(analogRead(analogPin5));
  Serial.print(",");
  Serial.print(analogRead(analogPin6));
  Serial.print(",");
  Serial.println(analogRead(analogPin7));
//  Serial.print(",");
//  Serial.println(analogRead(analogPin8));
//  Serial.println(analogRead(analogPin11));
  delay(50);
}
```

B.2 MatLab

This script was developed over several years and calls many supporting functions, which were developed to support the tests during different system configurations.

As such, the script has flagged sections which can be turned on and off, as well as sections that are commented out and functions that aren't called.

The script was kept in a folder called dataCheckScript. The main is fullDataCheck fullSystem, which calls the a primary function that does the majority of the heavy lifting while also calling auxiliary subfunctions titled loadData, flowTurbines, scales, pressureTransducers, sickTransducers, psuOutputs, HEsensors and getIRFFTs.

B.2.1 dataCheckScript

B.2.1.1 fullDataCheck fullSystem

```
clearvars
% close all

%pathName = '/local/aut17twu/Documents/MATLAB/current/dataSetsToBeChecked/';
%pathName = 'F:\MTH18F Home\Documents\MATLAB\current\dataCheckScript\dataSetsToBeC
pathName = 'C:\Users\Engineering\Desktop\Data\dataCheckScript\current\dataSetsToBe

folderListings = dir(pathName);
folderContents = folderListings(~ismember({folderListings.name}, {'.', '..'}));
clear('folderListings')

T = table('Size',[length(folderContents),2],'VariableTypes',["double","string"],'V
S=struct2cell(folderContents);
S=S';

for i = 1:length(folderContents)
    T(i,1) = num2cell(i);
```

```
    T(i,2) = S(i);
end

disp(T);

prompt='choose folderName (use the indexNumber eg. 3): ';

indexNumber=input(prompt);

folderName = T{indexNumber,2}

folderPath = append(pathName,folderName) + "\";

fileListings = dir(folderPath);

fileList = fileListings(~ismember({fileListings.name}, {'.', '..'}));

for i = 1:length(fileList)
    fileName = fileList(i).name;
    dataStore(i) = runMainTestScript_theBigKahuna_fullSystem(pathName,fileName,fol
end

%saveFolder=('/local/aut17twu/Documents/MATLAB/current/convertedDataSets/');
%saveFolder='F:\MTH18F Home\Documents\MATLAB\current\dataCheckScript\convertedData
saveFolder='C:\Users\Engineering\Desktop\dataCheckScript\current\convertedDataSets

savePath=append(saveFolder,folderName);

save(savePath,'dataStore');

disp('pat yourself on the back')
```

B.2.1.2 runMainTestScript theBigKahuna fullSystem

```
function y = runMainTestScript_theBigKahuna(pathName,fileName,folderName)

%%% load datafile and convert datasets from anolog readings into relevant SI units

fullPath = fullfile(pathName,folderName,fileName);

rawData = loadData_fullSystem(fullPath); %load data from .csv file into a stucture

samplingRateInMicros = 1000; %set sampling rate (check with arduino code, should a

samplingFreq=1/(samplingRateInMicros*10^-6);

trigger=200; %set trigger-threshold for flow-meters (halleffect pulse turbine)

timeInMicros = (samplingRateInMicros:samplingRateInMicros:samplingRateInMicros*raw

timeInSeconds = timeInMicros./10^6; %convert that timeseries into seconds

data_lps = flowTurbines(rawData.pulses_flow1,rawData.pulses_flow2,[],trigger,sampl

%data_scales = scales(rawData.scales); %run scales function to convert raw scales

data_pressure = pressureTransducers(rawData.pt1,rawData.pt2); %run pressure functi
data_sick_pressure = sickTransducers(rawData.sick1,rawData.sick2)
data_PSU = psuOutputs(rawData.Ipsu, rawData.Vpsu)
```

```
%data_HEsensors = HEsensors(rawData.HE_disp1Standard, rawData.HE_disp2Sensitive);

y.folderName = folderName;
y.filename = fileName;
y.rawData = rawData;
y.convertedData.LPS = data_lps;
%y.convertedData.Scales = data_scales; %trying to convert into litre staright away
y.convertedData.Pressure = data_pressure;
y.convertedData.SickPressure = data_sick_pressure;
y.convertedData.PSU = data_PSU;
y.convertedData.tSeconds = timeInSeconds;

%%%% preliminary visual check on converted datasets
figure
subplot(2,2,1)
plot(data_lps.lps1Adj,'.')
hold on
plot(data_lps.lps2Adj,'.')
title('flow rates')

subplot(2,2,2)
plot(data_pressure.kPaP1,'.')
hold on
plot(data_pressure.kPaP2,'.')
title('pressure')

subplot(2,2,3)
plot(data_sick_pressure.sick1,'.')
hold on
plot(data_sick_pressure.sick2,'.')
```

```
title('sick pressure')

subplot(2,2,4)
plot(data_PSU.V,'.')
hold on
plot(data_PSU.I,'.')
title('PSU')

%subplot(2,2,4)
%plot(data_scales.I_C_c,'.')
%title('leakage')

%sgtitle({['{\bf\fontsize{14}' folderName '}'],fileName});
sgtitle(string(folderName)+"_" + string(fileName))

%%%%%%%%%%% select inputFrequency of dataset from visual check %%%%%%%%%
inputFrequency=[1 2 3; "slow" "medium" "fast"; 0.019 0.193 1.923];
inputFrequency=inputFrequency';
T=table(inputFrequency);
disp(T);
prompt='which frequency is it ? Select a number i.e. 1, 2 or 3: ';
indexNumber=input(prompt);
periodLen=1/str2double(inputFrequency(indexNumber,3));

%establish smallest set of flow data and interpolate remaining sets to
%smallest set
if numel(data_lps.tSeries1) < numel(data_lps.tSeries2)
    I_2_F_t = interp1(data_lps.tSeries2,data_lps.lps2Adj,data_lps.tSeries1,'linear
    I_F_t = data_lps.lps1Adj;
    t_series = data_lps.tSeries1;
    p_index = data_lps.pIndex1;
```

```
else
    I_F_t = interp1(data_lps.tSeries1,data_lps.lps1Adj,data_lps.tSeries2,'linear')
    I_2_F_t = data_lps.lps2Adj;
    t_series = data_lps.tSeries2;
    p_index = data_lps.pIndex2;
end

%%%% p_index all datasets%%%%%%%%
%I_C_s_ml=zeros(numel(p_index),1);
dV_L_t=zeros(numel(p_index),1);
dV2_L_t=zeros(numel(p_index),1);
sick_1_t=zeros(numel(p_index),1);
sick_2_t=zeros(numel(p_index),1);
PSU_V_t=zeros(numel(p_index),1);
PSU_I_t=zeros(numel(p_index),1);
%kPaPiston1=zeros(numel(p_index),1);
%kPaPiston2=zeros(numel(p_index),1);
%xDisp1=zeros(numel(p_index),1);
%xDisp2=zeros(numel(p_index),1);

for x = (1:numel(p_index))
    % how does this work? ...we're just taking a straight index...check
    %I_C_s_ml(x,1) = data_scales.I_C_c(p_index(x));
    dV_L_t(x,1) = data_pressure.kPaP1(p_index(x));
    dV2_L_t(x,1) = data_pressure.kPaP2(p_index(x));
    sick_1_t(x,1)= data_sick_pressure.sick1(p_index(x));
    sick_2_t(x,1)= data_sick_pressure.sick2(p_index(x));
    PSU_V_t(x,1) = data_PSU.V(p_index(x));
    PSU_I_t(x,1) = data_PSU.I(p_index(x));
end
```

```
%I_C_s_l = I_C_s_ml./10^3;


y.pIndexedData.I_F_t = I_F_t;
y.pIndexedData.I_2_F_t = I_2_F_t;
%y.pIndexedData.I_C_s_l = I_C_s_l;
y.pIndexedData.dV_L_t = dV_L_t;
y.pIndexedData.dV2_L_t = dV2_L_t;
y.pIndexedData.sick1 = sick_1_t;
y.pIndexedData.sick2 = sick_2_t;
y.pIndexedData.psu_v =PSU_V_t;
y.pIndexedData.psu_i =PSU_I_t;
y.pIndexedData.tSeries = t_series;
y.pIndexedData.pIndex = p_index;

%%% OBMC-IRFFT datasets that can be i.e. flow, pressure and HEsensors
%IRFFTdataSets= ["IFt","I2Ft","dVLt","dV2Lt","kPaPiston1","kPaPiston2","xDisp1","x
IRFFTdataSets= ["IFt","I2Ft","dVLt","dV2Lt","sick1","sick2","psu_v","psu_i"]; % NM



noisyData.IFt=I_F_t;
noisyData.I2Ft=I_2_F_t;
noisyData.dVLt=dV_L_t;
noisyData.dV2Lt=dV2_L_t;
noisyData.sick1 = sick_1_t;
noisyData.sick2 = sick_2_t;
noisyData.psu_v = PSU_V_t;
noisyData.psu_i = PSU_I_t;

%noisyData.kPaPiston1=kPaPiston1;
%noisyData.kPaPiston2=kPaPiston2;
%noisyData.xDisp1=xDisp1;
```

```
%noisyData.xDisp2=xDisp2;
% dataNames = fieldnames(noisyData);

for i=1:numel(IRFFTdataSets)

    if i==1
        figure
        plot(noisyData.(IRFFTdataSets(i)),'.')
        legend('noisy data')
        grid on
        grid minor

        disp('what is a good startPoint and stopPoint to capture one whole period?
        disp('NB note that scales data is the prime time-series to use, if you hav
        prompt=('startPoint value? ');
        startPoint=input(prompt);%startPoint(1)=input(prompt);
        prompt=('stopPoint value? ');
        stopPoint=input(prompt);%stopPoint(1)=input(prompt);
        y.IRFFTdData.startPoint=startPoint;
        y.IRFFTdData.stopPoint=stopPoint;
    end

    IRFFTs.(IRFFTdataSets(i))=getIRFFTs(noisyData.(IRFFTdataSets(i)),startPoint,st

    if isfield(IRFFTs,'happy') && IRFFTs.happy == 'n'
        return
    end
    y.IRFFTdData.(IRFFTdataSets(i))=IRFFTs.(IRFFTdataSets(i));
end

%%%%%%% 10th order ploynomial scales data %%%%%%%%%%
```

```
%%%% NM: Not used for full system...chck
%ICsl = I_C_s_l(startPoint:stopPoint);
%tSeries = t_series(startPoint:stopPoint);

%[p,~,mu]= polyfit(tSeries,ICsl,10);

%ICsl_polyfit = polyval(p,tSeries,[],mu);

%figure
%plot(tSeries,ICsl,'.')
%hold on
%plot(tSeries,ICsl_polyfit,'--')

%dtSeries = diff(tSeries);
doRegressions = false
if doRegressions

IFt = IRFFTs.IFt.OBMCfiltered(2:end);
%ICt = diff(ICsl_polyfit)./diff(tSeries);
%IFs = cumsum(IRFFTs.IFt.OBMCfiltered(2:end).*dtSeries);
%kPaPiston1 = IRFFTs.kPaPiston1.OBMCfiltered(2:end);
%ICs = ICsl_polyfit(2:end);
%dVLt = IRFFTs.dVLt.OBMCfiltered(2:end);

%y.tSeries = tSeries;
%y.polyfitttedData.ICs = ICsl;
%y.polyfitttedData.tSeries = tSeries;
%y.polyfitttedData.dICsl = diff(ICsl_polyfit);
%y.polyfitttedData.ICt = ICt;
```

```
%%%%%%%%%%% findCompponentShift %%%%%%%%%%%%%%%%%%%%%%
ComponentShiftVars.IFt = IFt;
ComponentShiftVars.ICt = ICt;
ComponentShiftVars.IFs = IFs;
ComponentShiftVars.kPaPiston1 = kPaPiston1;
ComponentShiftVars.ICs = ICs;
ComponentShiftVars.dVLt = dVLt;

componentDistance.PT1=3.86; %in m and from the sensor to the centre of the clark
componentDistance.FT1=1.45;
componentDistance.PT2=0.2;
componentDistance.FT2=2.55;
componentDistance.L=1.7; %the length of the hose that we measure leakage from

IDofPipe=19; %internal diameter of pipe in mm
AofPipe=pi*(0.019/2)^2;

m3ps1Average=mean(data_lps.lps1Adj)/1000;
m3ps2Average=mean(data_lps.lps2Adj)/1000;
metersPersSecond1=m3ps1Average/AofPipe;
metersPersSecond2=m3ps2Average/AofPipe;

expectedLag_PT1toPT2=(componentDistance.PT1+componentDistance.PT2)/metersPersSecon
expectedLag_PT1toFT1=(componentDistance.PT1-componentDistance.FT1)/metersPersSecon
expectedLag_FT1toPT2=(componentDistance.FT1+componentDistance.PT2)/metersPersSecon
expectedLag_PT1toL=(componentDistance.PT1+componentDistance.L)/metersPersSecond1;
expectedLag_FT1toL=(componentDistance.FT1+componentDistance.L)/metersPersSecond1;
expectedLag_PT1toPiston=(componentDistance.PT1+0)/metersPersSecond1;

expectedLags = [expectedLag_PT1toFT1,expectedLag_PT1toL,expectedLag_FT1toL,expecte
```

```
regressionX_names = ["IFt","ICt","ICs","kPaPiston1"];   %sumvec aka vec2
regressionY_names = ["dVLt","dVLt","IFs","dVLt"];       %target

uBoundShift=250;
lBoundShift=0;
doPlot=0; % doPlot=1;

flag = "chooseFirst"; % "chooseMax" == choose the lag with the highest RSq val
gradient =[];

for i = 1:numel(regressionX_names)

    regressionPair = regressionX_names(i) + "_" +regressionY_names(i)

    componentShift.(regressionPair)=findComponentShift220405(0*ComponentShiftV

    y.componentShift.(regressionPair)=componentShift.(regressionPair);

    componentLagInSeconds = componentShift.(regressionPair).estimatedLag;

    y.componentShift.(regressionPair).componentLagInSeconds = componentLagInSe

    gradient = [gradient,componentShift.(regressionPair).model.Coefficients.Es

    y.componentShift.(regressionPair).gradient = gradient;

end
%       componentShift.ICs_IFs.vec2_withLag    componentShift.ICs_IFs.target_
```

```
I3Fs = componentShift.ICs_IFs.vec2_withLag - componentShift.ICs_IFs.target_wit
IFti = IFt(1:numel(componentShift.kPaPiston1_dVLt.target_withLag));
I2Ft = IRFFTs.I2Ft.OBMCfiltered(1:numel(componentShift.kPaPiston1_dVLt.target_
dVLti = dVLt(1:numel(componentShift.ICs_IFs.vec2_withLag));
dVst = componentShift.kPaPiston1_dVLt.target_withLag - componentShift.kPaPistc
I3Fsi = I3Fs(numel(I3Fs)-numel(dVst)+1:end);

regressionX_names = ["I3Fs","IFti","I2Ft","I3Fsi"];
regressionY_names = ["dVLti","dVst","dVst","dVst"];

% regressionX_names = ["I3Fs","IFti","I2Ft"];
% regressionY_names = ["dVLti","dVst","dVst"];

ComponentShiftVars.I3Fs = I3Fs;
ComponentShiftVars.dVst = dVst;
ComponentShiftVars.dVLti = dVLti;
ComponentShiftVars.IFti = IFti;
ComponentShiftVars.I2Ft = I2Ft;
ComponentShiftVars.I3Fsi = I3Fsi;

for i = 1:numel(regressionX_names)

    regressionPair = regressionX_names(i) + "_" +regressionY_names(i)

    componentShift.(regressionPair)=findComponentShift220405(0*ComponentShiftV

    y.componentShift.(regressionPair)=componentShift.(regressionPair);

    componentLagInSeconds = componentShift.(regressionPair).estimatedLag;

    y.componentShift.(regressionPair).componentLagInSeconds = componentLagInSe
```

```
        gradient = [gradient,componentShift.(regressionPair).model.Coefficients.Es

        y.componentShift.(regressionPair).gradient = gradient;

    end

end

end
```

B.2.1.3 loadData fullSystem

```
function y = loadData(fullPath,~)

dataSet=readtable(fullPath); %dataSetsToBeChecked/
y.pulses_flow1 = dataSet{3:end,1};
y.pulses_flow2 = dataSet{3:end,2};
%y.pulses_flow3  = dataSet{3:end,3};
% original full system test pin config
% y.pt1 = dataSet{3:end,3};
% y.pt2 = dataSet{3:end,4};
% y.sick1 = dataSet{3:end,5};
% y.sick2 = dataSet{3:end,6};
% NM 24/02/24 new pin config: pins 5&6 were reading higher values (approx
% 290) at atm, expecting 204. Appears baseline voltage of sick increases
% when connected to these pins, possibly because pins have higher
% resistance? check correct wiring with sick, for now pins 3&4 seem
% unaffected, and pt1 & 2 readings are same on 5&6 as for 3&4.
```

```
y.pt1 = dataSet{3:end,5};
y.pt2 = dataSet{3:end,6};
y.sick1 = dataSet{3:end,3};
y.sick2 = dataSet{3:end,4};


y.Ipsu = dataSet{3:end,7};
y.Vpsu = dataSet{3:end,8};
y.size = size(dataSet{3:end,1},1);
end
```

B.2.1.4 flowTurbines

```
function y = flowTurbines(Flow1,Flow2,Flow3,trigger,samplingRateInMicros,~)

% This script finds the Hz from the pulses of p1, p2, flow 3 = Hz1,
% Hz2, Hz3

%%%%% polyfit.cofficients are from the original first round of bin filling
%%%%% (results can be found in 'reject k value error validation 2021')
polyfit.coefficients = [9.82275481583866E-15 -1.39909449889168E-11
8.14578073133654E-09 -2.49311280178075E-06 0.000428696
-0.0409355207 2.0204717038 165.3000248355;
    -8.83064393254399E-15 1.1830239035472E-11 -6.3160819570188E-09
1.71658648364681E-06 -0.0002520061 0.0194107555 -0.5943764233
213.5340200117;
    -2.27354604299708E-14 2.91043872946576E-11
-1.49271915464541E-08 3.91378669521436E-06 -0.0005531991
0.0402747765 -1.161996483 189.1995191243];
```

```
%%%%% polyfit.adjusted.cofficients are from the second first round of bin filling
%%%%% (results can be found in 'reject k value error validation 2021' - mob adjust
%%%%% this was in response to changing the way the data was read via the
%%%%% arduino meant we weren't dropping spikes anymore and had to re-adjust
%%%%% the k-value's for the FT flow sensors
polyfit_adjusted.coefficients = [1.0206584E-14 -1.45033743E-11
8.41978130E-09 -2.5678524679E-06 4.39637E-04  -0.0417595257137
2.0478128E+00 1.6437202410E+02
-9.6599198E-15 1.32736650E-11 -7.319745462E-09  2.07091E-06
-0.0003183317  2.562685557E-02 -0.84907771156 2.1441338497E+02
 -1.39643575976E-14 1.83944642E-11  -9.727141122044E-09
2.63437E-06 -0.000384684142 2.870065914E-02 -0.790880671932282
1.9083461944E+02];

%%%% old one [9.78963E-15 -1.39439E-11 8.11846E-09 -2.48478E-06
0.00042769 -0.0408 2.0138235 164.76595
%%%%    -8.73745E-15 1.177054E-11 -6.24943E-09 1.69847E-06
-0.000249347 0.01920591 -0.0588104 211.280608
%%%%    -2.324478E-14 2.9756385E-11 -1.56261589E-08 4.001463E-06
-0.0005655918 0.0411770087 -1.1880274326 193.43795119];

polyfit.meterId = [130477, 136845, 136846];
polyfit.columnName = {'pulseF','pulseP','pulseR'};

%Finding Hz1
trigCount1=0;
for x = 1:numel(Flow1)-1
    x1 = x+1;
    if Flow1(x)<trigger && Flow1(x1)>trigger
        trigCount1=trigCount1+1;
    end
```

```
end

n=trigCount1;
trigCount1=0;
Hz1=zeros(n,1);
samplingRate=samplingRateInMicros*10^-6; %in seconds
previousx1=0;
pulseIndex1=zeros(n,1);

for x = 1:numel(Flow1)-1
    x1 = x+1;
    if Flow1(x)<trigger && Flow1(x1)>trigger
        trigCount1=trigCount1+1;
        Hz1(trigCount1,1)=1/((x1-previousx1)*samplingRate);
        previousx1=x1;
        pulseIndex1(trigCount1,1)=x1;
    end
end

% ignore first element of Hz as we do not know exactly when it was triggered
Hz1=Hz1(2:end);
pulseIndex1=pulseIndex1(2:end);
idIndex = 1;
theseCoeffs = polyfit.coefficients(idIndex, :);
theseAdjustedCoeffs = polyfit_adjusted.coefficients(idIndex, :);

% get the unadjusted scaling factor (ie evaluate the polynomial at the observed pu
kValue_unadjusted = 0*Hz1;
kValue_adjusted = 0*Hz1;

for i = 0:length(theseCoeffs)-1
```

```
    kValue_unadjusted = kValue_unadjusted + theseCoeffs(length(theseCoeffs) -i)* H
    kValue_adjusted = kValue_adjusted + theseAdjustedCoeffs(length(theseAdjustedCo
end

y.lps1Adj = Hz1./kValue_adjusted;
y.lps1Unadj = Hz1./kValue_unadjusted;
y.Hz1=Hz1;
y.pIndex1=pulseIndex1;
y.tSeries1=pulseIndex1.*2*10^-4;

%Finding Hz2
trigCount2=0;
for x = 1:numel(Flow2)-1
    x1 = x+1;
    if Flow2(x)<trigger && Flow2(x1)>trigger
        trigCount2=trigCount2+1;
    end
end

n=trigCount2;
trigCount2=0;
Hz2=zeros(n,1);
%samplingRate=samplingRateInMicros*10^-6; %in seconds
previousx1=0;
pulseIndex2=zeros(n,1);
for x = 1:numel(Flow2)-1
    x1 = x+1;
    if Flow2(x)<trigger && Flow2(x1)>trigger
        trigCount2=trigCount2+1;
        Hz2(trigCount2,1)=1/((x1-previousx1)*samplingRate);
        previousx1=x1;
```

```
        pulseIndex2(trigCount2,1)=x1;
    end
end

% ignore first element of Hz as we do not know exactly when it was triggered
Hz2=Hz2(2:end);
pulseIndex2=pulseIndex2(2:end);
idIndex = 3;
theseCoeffs = polyfit.coefficients(idIndex, :);
theseAdjustedCoeffs = polyfit_adjusted.coefficients(idIndex, :);

% get the unadjusted scaling factor (ie evaluate the polynomial at the observed pu
kValue_unadjusted = 0*Hz2;
kValue_adjusted = 0*Hz2;

for i = 0:length(theseCoeffs)-1
    kValue_unadjusted = kValue_unadjusted + theseCoeffs(length(theseCoeffs) -i)* H
    kValue_adjusted = kValue_adjusted + theseAdjustedCoeffs(length(theseAdjustedCo
end

y.lps2Adj = Hz2./kValue_adjusted;
y.lps2Unadj = Hz2./kValue_unadjusted;
y.Hz2=Hz2;
y.pIndex2=pulseIndex2;
y.tSeries2=pulseIndex2.*2*10^-4;

%Finding Hz3
if isempty(Flow3)
    return
end
```

```
trigCount3=0;
for x = 1:numel(Flow3)-1
    x1 = x+1;
    if Flow3(x)<trigger && Flow3(x1)>trigger
        trigCount3=trigCount3+1;
    end
end

n=trigCount3;
trigCount3=0;
Hz3=zeros(n,1);
%samplingRate=samplingRateInMicros*10^-6; %in seconds
previousx1=0;
pulseIndex3=zeros(n,1);
for x = 1:numel(Flow3)-1
    x1 = x+1;
    if Flow3(x)<trigger && Flow3(x1)>trigger
        trigCount3=trigCount3+1;
        Hz3(trigCount3,1)=1/((x1-previousx1)*samplingRate);
        previousx1=x1;
        pulseIndex3(trigCount3,1)=x1;
    end
end

% ignore first element of Hz as we do not know exactly when it was triggered
Hz3=Hz3(2:end);
pulseIndex3=pulseIndex3(2:end);
idIndex = 2;
theseCoeffs = polyfit.coefficients(idIndex, :);
theseAdjustedCoeffs = polyfit_adjusted.coefficients(idIndex, :);
```

```
% get the unadjusted scaling factor (ie evaluate the polynomial at the observed pu
kValue_unadjusted = 0*Hz3;
kValue_adjusted = 0*Hz3;

for i = 0:length(theseCoeffs)-1
    kValue_unadjusted = kValue_unadjusted + theseCoeffs(length(theseCoeffs) -i)* H
    kValue_adjusted = kValue_adjusted + theseAdjustedCoeffs(length(theseAdjustedCo
end

y.lps3Adj = Hz3./kValue_adjusted;
y.lps3Unadj = Hz3./kValue_unadjusted;
y.Hz3=Hz3;
y.pIndex3=pulseIndex3;
y.tSeries3=pulseIndex3.*2*10^-4;
clear x
end
```

B.2.1.5 scales

```
function y = scalesToMl(scalesData)

% load calibration data to extrapolate the scales analog value (raw data) to a vol
load('scalesCalibrationUltimate');
ml_ult = scalesCalibrationUltimate(:,1);
anaScales_ult = scalesCalibrationUltimate(:,2);

% perform extrapolation and declare it a global variable
y.I_C_c = interp1(anaScales_ult, ml_ult, scalesData, 'linear', 'extrap');
```

```
end
```

B.2.1.6 pressureTransducers

```
function y = analogPTtokPa(pt1,pt2);

    load('pressure1calib');
    kPa1 = pressure1calib(:,1); %NB!!! validate digital to analog curve
    analogPressure = pressure1calib(:,2);
    y.kPaP1 = interp1(analogPressure, kPa1, pt1, 'linear', 'extrap');
    y.kPaP2 = interp1(analogPressure, kPa1, pt2, 'linear', 'extrap');
    y.kPaP1newFit = (pt1-[131.499966481646])/[0.716723087902708];
    y.kPaP2newFit = [1.41483105463544].*pt2+[-185.455510085796];
end
```

B.2.1.7 sickTransducers

```
function y = sickTransducers(pt1,pt2);
    % analog to kPa
    coeffs = readtable('sickSensorLinearFitCoeffficeints.xlsx')
    % NM 23/02/24 using 10bit theoretical conversion from bit to bar: this
    % assumes both sicks read 0-100 bar on range 1-5V on 10 bit arduino
    y.sick1 = (pt1-coeffs{3,2})/coeffs{3,3}
    y.sick2 = (pt2-coeffs{3,2})/coeffs{3,3}
end
```

B.2.1.8 psuOutputs

```
function y = psuOutputs(I,V);
    % does nothin really
    y.I = I;
    y.V = V;
end
```

B.2.1.9 HEsensors

```
function y = HEsensors(HE_disp1Standard, HE_disp2Sensitive)

HEcalibData=readtable('21112 2');
calib5turns=readtable('211122HEdist5turns.xlsx');

HE1standard=zeros(length(calib5turns.turns),1);
HE2sensitive=zeros(length(calib5turns.turns),1);
for i =1:numel(calib5turns.turns)
    HE1standard(i)= mean(HEcalibData.Var2(calib5turns.x1(i):calib5turns.x2(i)));
    HE1standard = HE1standard';
    HE2sensitive(i)= mean(HEcalibData.Var3(calib5turns.x1(i):calib5turns.x2(i)));
    HE2sensitive = HE2sensitive';
end

springDisplacement1 = interp1(HE2sensitive,calib5turns.mm,HE_disp1Standard,'linear
springDisplacement2 = interp1(HE1standard,calib5turns.mm,HE_disp2Sensitive,'linear
kSpringConst = 5353.07; %N/m
```

```
Force1 = kSpringConst*(springDisplacement1./1000);
Force2 = kSpringConst*(springDisplacement2./1000);
pistonIDmm = 69.8; %in mm
pistonID = pistonIDmm/1000; %in m
piston_area = pi*(pistonID/2)^2; %in m^2

y.displacement1= springDisplacement1;
y.displacement2= springDisplacement2;
y.kPa_piston1 = (Force1/piston_area)/1000;
y.kPa_piston2 = (Force2/piston_area)/1000;
end
```

B.2.1.10 getIRFFTs

```
function y = getIRFFTs(noisyData,startPoint,stopPoint,samplingFreq,~)

x = noisyData(startPoint:stopPoint);
yForPlotting=x;
returnTimeIntervals =[1,numel(x)];
t = (1:numel(x)).'/samplingFreq;

theseIntervals = returnTimeIntervals(1,:);
theseTimes = t(theseIntervals(1):theseIntervals(2));
theseObs = x(theseIntervals(1):theseIntervals(2));

fftTheseObs = fft(theseObs);
imagObs = imag(fftTheseObs);

range = max(theseObs) - min(theseObs);
```

```
mu_obs = mean(theseObs);
gradientSignChanges = zeros(100,1);

for k =  1:100
    u = zeros(numel(x),1);
    for n = 1:size(theseTimes,1)
        u(n) = 0;
        for kk = 1:k
            u(n) = u(n) + fftTheseObs(kk)*exp(1i*2*pi*(kk-1)*(n-1)/size(imagObs,1)
        end
    end

    range_u = (max(real(u))-min(real(u)));
    if range_u > 0
        u = range*u/range_u;
    end

    u = (mu_obs -mean(real(u))) + u;
    realU = real(u);

    DrealU = diff(realU);
    signU = sign(DrealU);
    signDiff = signU(1:end-1) ~= signU(2:end);
    totalU = sum(signDiff);
    gradientSignChanges(k) = totalU;

end

figure
plot(gradientSignChanges);
title('gradient sign changes')
```

```
grid on
grid minor
xticks(0:2:100);
prompt='local minima?';
localMinima=input(prompt);
close

for k = localMinima
    u = zeros(numel(x),1);
    for n = 1:size(theseTimes,1)
        u(n) = 0;
        for kk = 1:k
            u(n) = u(n) + fftTheseObs(kk)*exp(1i*2*pi*(kk-1)*(n-1)/size(imagObs,1)
        end
    end

    range_u = (max(real(u))-min(real(u)));
    if range_u > 0
        u = range*u/range_u;
    end

    u = (mu_obs -mean(real(u))) + u;

    realU = real(u);

    DrealU = diff(realU);
    signU = sign(DrealU);
    signDiff = signU(1:end-1) ~= signU(2:end);
    totalU = sum(signDiff);
    gradientSignChanges(k) = totalU;
```

```
end


realU_1=realU;


x=realU_1-x;


returnTimeIntervals =[1,numel(x)]; %6162
t = (1:numel(x)).'/samplingFreq;


theseIntervals = returnTimeIntervals(1,:);
theseTimes = t(theseIntervals(1):theseIntervals(2));
theseObs = x(theseIntervals(1):theseIntervals(2));


fftTheseObs = fft(theseObs);


imagObs = imag(fftTheseObs);


%Nsamples = size(theseObs,1);


range = max(theseObs) - min(theseObs);
mu_obs = mean(theseObs);
gradientSignChanges = zeros(100,1);



for k =  k
    u = zeros(numel(x),1);
    for n = 1:size(theseTimes,1)
        u(n) = 0;
        for kk = 1:k
            u(n) = u(n) + fftTheseObs(kk)*exp(1i*2*pi*(kk-1)*(n-1)/size(imagObs,1)
        end
```

```
    end

    range_u = (max(real(u))-min(real(u)));

    if range_u > 0
        u = range*u/range_u;
    end

    u = (mu_obs -mean(real(u))) + u;
    realU = real(u);

    DrealU = diff(realU);
    signU = sign(DrealU);
    signDiff = signU(1:end-1) ~= signU(2:end);
    totalU = sum(signDiff);
    gradientSignChanges(k) = totalU;

end
realU_2=realU;
meanU_new=(realU_1+(realU_1-realU_2))/2;

y.OBMCfiltered=meanU_new;
y.localMinima=localMinima;

figure
title('final result')
plot(yForPlotting,'.')
hold on;
plot(meanU_new,'--')
hold off;
```

```
prompt = 'Are you happy? hit any key to continue or n to exit script ';
happy = input(prompt,'s');


if happy == 'n'
    y.happy = (happy);
    return
end
close
end
```